

**UNIVERSIDAD NACIONAL DE INGENIERÍA
FACULTAD DE CIENCIAS**

**Sección de Posgrado y Segunda Especialización
Profesional**



Tesis para Optar el Grado Académico de
Doctor en Ciencias con mención en Química

**“Celdas Sensibilizadas de Óxido de Zinc:
Nuevos Enfoques”**

Presentada por:

María Esther Quintana Cáceda

LIMA - PERÚ

2008

Index

ABSTRACT.....	iii
PREFACE.....	iv
ACKNOWLEDGMENT.....	v
LIST OF SYMBOLS.....	vi
LIST OF ACRONYMS AND ABBREVIATIONS.....	viii
Chapter 1 Introduction.....	1
1.1. Solar Cells.....	1
1.2. Dye sensitized solar cell (DSC).....	2
1.3. DSC based on ZnO.....	2
Bibliography.....	4
Chapter 2 Photochemistry of semiconductor.....	5
2.1. Semiconductors.....	5
2.1.1. Density of electrons and holes.....	6
2.1.2. Localized States for impurities and vacancies.....	7
2.1.3. ZnO crystalline structure.....	8
2.2. Electrolyte.....	10
2.3. Dyes.....	11
2.4. Semiconductor-electrolyte interface.....	12
Bibliography.....	14
Chapter 3 Principles of dye sensitized solar cells.....	15
3.1. Operational principles.....	15
3.2. Energetics.....	16
3.3. Light absorption.....	17
3.3.1. Light absorption via MLCT excitation.....	18
3.4. Charge Transport.....	19
3.4.1. Recombination.....	19
3.5. Kinetics.....	21
3.5.1. Charge Transfer Dynamics.....	21
Bibliography.....	23
Chapter 4 Experimental techniques and device preparation.....	24
4.1. Materials and synthesis.....	24
4.1.1. TCO coated glass.....	24
4.1.2. Nanoparticle electrodes.....	25
4.1.2.1. ZnO particle synthesis.....	25
4.1.2.2. TiO ₂ particle synthesis.....	26
4.2. Device assembly.....	27
4.2.1. Photoelectrodes.....	27
4.2.2. Counterelectrodes.....	28
4.2.3. Electrolytes.....	28
4.2.4. Cell assembly.....	28
4.3. Photoelectrochemical characterization.....	28
4.3.1. Incident photon-to-current conversion efficiency (IPCE).....	30
4.3.2. Voltage Charge.....	32
4.4. Analytical characterization.....	33
4.4.1. Absorption spectroscopy.....	33
4.4.2. SEM.....	34
4.4.3. TEM.....	35
4.4.4. X ray diffraction.....	36
4.4.5. ATR.....	38

4.5. Intensity-modulated photocurrent and photovoltage spectroscopy (IMPS, IMVS)	38
Bibliography	40
Chapter 5 Influence of morphology and doped in ZnO photoelectrodes	42
5.1. ZnO nanorods and nanoparticles in DSC	42
5.1.1. ZnO nanorods synthesis	42
5.1.2. ZnO nanorods and nanoparticles characterization	43
5.1.3. Photoelectrochemical characterization	44
5.1.4. Electron Transport Studies	47
5.2. ZnO phototlectrodes doped with Li ⁺ , Mg ²⁺	48
5.2.1. Preparation of ZnO doped Mg ²⁺ photoelectrodes	48
5.2.1.1. Film characterization	48
5.2.1.2. Photoelectrochemical characterization	50
5.2.2. Preparation of ZnO doped Li ⁺ photoelectrodes	51
5.2.2.1. Film characterization	52
5.2.2.2. Photoelectrochemical measurements	52
5.2.2.3. Electron Transport studies	53
Bibliography	54
Chapter 6 Comparison between ZnO and TiO ₂ dye sensitized solar cell	56
6.1. Film characterization	56
6.2. Photoelectrochemical measurements	58
6.3. Electron transport studies	59
Bibliography	64
Chapter 7 New dye D5: Charge transfer process in dye sensitized ZnO solar cells	65
7.1. Dye sensitizers : D5 – N719	65
7.1.1. Photoelectrochemical measurements	65
7.1.2. Electron transport studies	66
7.1.3. ATR measurements	69
7.2. Different concentration of Li ⁺ in the electrolyte	70
7.2.1. Photoelectrochemical measurements	70
7.2.2. Electron transport studies	71
Bibliography	73
Chapter 8 Discussion	74
8.1. Effect of morphology and doping	74
8.1.1. ZnO nanorods and nanoparticles	74
8.1.2. Doped ZnO	75
8.2. Comparison with TiO ₂ solar cell	76
8.3. Effect of new dye D5	78
Bibliography	80
Chapter 9 Conclusions	82

UNIVERSIDAD NACIONAL DE INGENIERIA
FACULTAD DE CIENCIAS
SECCION DE POSGRADO Y SEGUNDA ESPECIALIZACION PROFESIONAL

Nombre de la alumna: Mg. María Esther Quintana Cáceda

Título de la tesis : Celdas sensibilizadas de Óxido de Zinc: Nuevos enfoques

RESUMEN

Las celdas solares sensibilizadas con colorante (DSC) han atraído mucha atención durante los últimos años debido a sus competitivas eficiencias y sus bajos costos. La tecnología está basada en una capa hecha de una película semiconductor (ZnO o TiO₂) la cual incrementa significativamente el haz óptico debido al recogimiento de luz por las moléculas del sensibilizador ancladas en su superficie, en contacto con la solución electrolítica.

En esta tesis fueron sintetizadas partículas nanocristalinas de ZnO con diferente forma, nanorods y nanopartículas, así como ZnO dopado con Mg²⁺ y Li⁺ para celdas solares sensibilizadas con colorante. Obteniendo mejores eficiencias con los fotoelectrodos nanoparticulados de ZnO.

La comparación con celdas solares sensibilizadas de TiO₂ muestra interesantes resultados. El transporte de electrones en las celdas solares fue estudiado usando espectroscopía de fotocorriente de intensidad modulada y reveló resultados muy similares para ZnO y TiO₂. La aparente energía de activación para el transporte de electrones en el ZnO nanoestructurado fue 0,1 eV, calculada de los tiempos de transporte en función de la temperatura bajo condiciones de corto circuito. El tiempo de vida de los electrones en los semiconductores nanoestructurados fue evaluado del decaimiento de voltaje a circuito abierto y espectroscopía de fotovoltaje de intensidad modulada. Fueron obtenidos mayores tiempos de vida para el ZnO. A pesar de la reducida recombinación, el rendimiento de las celdas solares sensibilizadas de ZnO fue menor que las de TiO₂, lo cual fue atribuido a una baja eficiencia en la inyección de electrones de las moléculas del colorante excitado y/o a una baja eficiencia en la regeneración del colorante. Los resultados podrían ser explicados usando un modelo de Múltiples Trampas, pero como los electrones están usualmente solo ligeramente atrapados en el ZnO, se presenta una alternativa.

Asimismo un eficiente colorante orgánico, la polieno-difenilamina D5, fue evaluado como sensibilizador y comparado con el N719. Eficiencias de cerca de 3% fueron obtenidas a 100 mW/ cm² con películas delgadas de ZnO (3 μ m). La sensibilización con este pigmento no mostró problemas de agregación, muy común para las celdas de ZnO, ya que para 14 horas de sensibilización pudo ser usado sin problemas.

Una disminución en la concentración de Li^+ en el electrolito muestra un cambio negativo en la banda de conducción (BC) siendo el efecto opuesto comparado a lo normalmente observado. La baja concentración de Li^+ produce una ligera disminución del fotovoltaje aumentando notablemente la fotocorriente resultando en un incremento de la eficiencia solar. La tendencia opuesta de la BC también fue observada en los electrodos de ZnO sin el colorante, revelando que el proceso ocurre entre el ZnO y el electrolito, independiente de la naturaleza del colorante. Finalmente este estudio muestra que la estabilidad del ZnO no solo debe ser considerada en la solución del colorante, sino principalmente en combinación con la composición del electrolito.

Lima, 17 de junio del 2008



MSc. María Quintana Cáceda
Autor



Dr. Wilfredo Hernandez
Asesor Local
Facultad de Ciencias UNI



Dr. Anders Hagfeldt
Asesor Externo
Universidad de Uppsala, Suecia

**NATIONAL UNIVERSITY OF ENGINEERING
FACULTY OF SCIENCE
POSTGRADUATE SECTION AND SECOND SPECIALIZATION**

Name: MSc. María Esther Quintana Cáceda
Thesis: DYE SENSITIZED ZnO SOLAR CELL: NEW APPROACHS

ABSTRACT

Dye-sensitized solar cells (DSS) have attracted much attention during the last few years, due to their competitive efficiencies and low costs. The technology is based on a layer made of semiconductor (ZnO or TiO₂) film which significantly increases the optical path for light harvesting by the surface-anchored sensitizer molecules, in contact with the electrolytic solution.

In this thesis where synthesized nanocrystalline particles of ZnO with different shape, nanorods and nanoparticles, as well as Mg²⁺ and Li⁺ doped ZnO for dye sensitized solar cells. Better efficiencies were obtained in ZnO nanoparticle photoelectrode.

Comparison with TiO₂ dye sensitized solar cells shows interesting results. Electron transport in the solar cells was studied using intensity-modulated photocurrent spectroscopy and revealed very similar results for ZnO and TiO₂. Apparent activation energies for electron transport in nanostructured ZnO of 0.1 eV were calculated from the temperature dependence of transport times under short-circuit conditions. The lifetime of electrons in the nanostructured semiconductors was evaluated from open-circuit voltage decay and intensity-modulated photovoltage spectroscopy. Significantly longer lifetimes were obtained with ZnO. Despite the reduced recombination, ZnO-based solar cells performed worse than TiO₂ cells, which was attributed to a lower electron injection efficiency from excited dye molecules and/or a lower dye regeneration efficiency. The internal voltage in the nanostructured ZnO film under short-circuit conditions was about 0.23 V lower than the open circuit potential at the same light intensity. Results may be explained using a multiple trapping model, but as electrons are usually only shallowly trapped in ZnO, an alternative view is presented. If there is significant doping of the ZnO, resulting band bending in the nanocrystals will form energy barriers for electron transport and recombination that can explain the observed properties.

Likewise an efficient polyene-diphenylaniline organic dye, D5, was evaluated as sensitizer and compared with N719. Efficiencies of about 3 % were obtained at 100 mW/cm² with thin films of ZnO (3 μm). Sensitization with this dye did not showed aggregate related problems; otherwise common for ZnO based solar cells, since 14 hours of sensitization times could be used without problems. A decreasing lithium concentration in the electrolyte showed a negative conduction band (CB) shift being the opposite effect compared to what is normally observed. Low concentration of lithium yielded slightly lower photovoltages, but notably higher photocurrent, resulting in the most favorable solar cell efficiencies. Increased injection efficiency and longer lifetimes explained the increase in efficiency for Dye-sensitized solar cells based on low lithium concentrations.

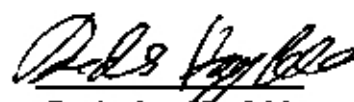
The opposite CB trend was also observed for bare ZnO electrodes revealing that the process occurring is between the ZnO and the electrolyte, independent on the dye nature. As a consequence of the working electrode instability the dye was desorbed in different amounts depending on the electrolyte nature. This study shows that the stability of the ZnO must not only be considered in the dye bath, but more importantly in combination with the electrolyte composition.



MSc. María Quintana Cáceda
Author



Dr. Wilfredo Hernandez
Local Adviser
UNI



Dr. Anders Hagfeldt
External Adviser
Uppsala University

PREFACE

The research presented in this thesis was developed at the Department of Chemistry, National University of Engineering in Peru, at the Division of Physical Chemistry of Royal Institute of Technology (KTH) and Uppsala University in Sweden during the years 2004-2007 under the main supervision of Dr. Anders Hagfeldt and Dr. Walter Estrada from Peru. The experimental work was performed in KTH and Uppsala University.

This doctoral thesis is presented in the International Agreement between National University of Engineering and the Royal Institute of Technology, Sweden.

The main objective of this thesis is optimization of ZnO dye sensitized solar cell, evaluating the photoelectrochemical and physical properties of them, considering the influence of the chemical synthesis of the nanoparticles of ZnO.

The thesis is based on the following papers.

1. Comparison of Dye-Sensitized ZnO and TiO₂ Solar Cells: Studies of Charge Transport and Carrier Lifetime

M. Quintana, T. Edvinsson, A. Hagfeldt, and G. Boschloo
J. Phys. Chem. C, **2007**, *111*, 1035-1041

2. A comparative study of a polyene-diphenylaniline dye and Ru(dcbpy)₂(NCS)₂ in electrolyte-based and solid-state dye-sensitized solar cells

G. Boschloo; T. Marinado; K. Nonomura; T. Edvinsson; A. Agrios; D. Hagberg; L. Sun; M. Quintana; C. Karthikeyan; M. Thelakkat; and A. Hagfeldt
Thin Solid Films, **2008**, *516*, 7214-7217

3. Organic chromophore-sensitized ZnO solar cells: photoinduced and electrolyte dependent dye desorption

M. Quintana, T. Marinado, K. Nonomura, G. Boschloo and A. Hagfeldt
Submitted

ACKNOWLEDGMENT

I never imagined the uncountable experiences, knowledge and friends that involved the realization of this work, even the opportunity to participate of this interchange program.

Then, I begin by saying thanks to Dr. Walter Estrada, who let me grow as professional in his Thin Films group and sent me to Sweden for my PhD studies. He and Dr. Juan Rodríguez have been my mentors in my scientific career.

Nothing could be possible without the help and guidance of Dr. Anders Hagfeldt, outstanding professional from Uppsala University, one of the pioneers in dye sensitized solar cells, and indisputable leader of one of the best research groups in the field. My eternal gratitude and admiration to him, as a professional and as a person, for his understanding and help, in all this period of travels and stages in Sweden. As well, I want to thank Dr. Gerrit Boschloo, for sharing his experience and knowledge, selflessly. To my friend, Dr. Tomas Edvinsson, for his help, understanding and jokes, that promoted a friendly atmosphere. To William Kylberg, for his friendship and help, on my first stage of learning "how to make solar cells". To my friends from Uppsala University, Goran Svensk, Goran Karlson, and Orlando Tapia, for their friendship. To all my friends of CMD: Leif, Eva, Alexander, Jarl, Marcelo y Ute, for the good moments and their company. To Lena Skowron from KTH, for the uncountable times that she helped me with paperwork. To my friend Kazu, for the interesting discussions about ZnO and his advices about it.

I need this paragraph to say "thanks a lot" to one of my best friends, during all this time she showed me her care and esteem, she gave me her friendship and let me get close to her family, my esteem and admiration to Tannia.

To my peruvian friends who live in Sweden, Johnny, Marta and Leonardo, thanks for their help and for the good moments we shared... and to my friend Pontus, for his help in the last year of my studies.

To the International Science Program (ISP), for the initial support that they gave me in the first years of my stages in Sweden.

Finally, nothing would have been possible without the help and understanding here, in Lima, especially from my little daughters. They stayed with my parents, my sisters, my husband and Carmencita... thanks a lot for their help, patience and love.

LIST OF SYMBOLS

Latin symbols

<i>a</i>	area
<i>A</i>	absorbance
<i>c</i>	speed of light
<i>CuKα</i>	K radiation of Cu [1.54 Å]
<i>d</i>	film thickness
<i>D</i>	(a) diffusion coefficient (b) Electronic ground of the dye molecule
<i>D⁺, D[*]</i>	oxidized and excited states of the dye molecule
<i>D_{red}</i>	density of occupied states
<i>D_{ox}</i>	density of empty states
<i>e⁻</i>	electron
<i>E_{red/ox}</i>	redox potential of redox couple
<i>E_F</i>	Fermi level
<i>E_g</i>	band gap energy
<i>F</i>	Faraday's constant
<i>g</i>	grain crystal size, at half its maximum intensity (rad)
<i>G_{sc}</i>	solar constant [1353](W/m ²)
<i>hν</i>	light illumination
<i>h</i>	Planck's constant
\hbar	$h/2\pi$
<i>h⁺</i>	hole
<i>I</i>	current
<i>I_{sc}</i>	short-circuit current
<i>I_m</i>	maximum current in a solar cell
<i>i</i>	current (A)
<i>i_{ph}</i>	photocurrent density (A/cm ²)
<i>j(t)</i>	transient current
<i>J_{sc}</i>	integral photocurrent density
<i>k</i>	Boltzmann's constant
<i>l</i>	length
<i>m</i>	electron mass
<i>N_c</i>	density of charge carriers
<i>N</i>	number of electrons exchanged during a redox reaction
<i>Ox/Re</i>	redox couple
<i>P</i>	power
<i>P_{in}</i>	incoming power from the sun
<i>P_m</i>	maximum power in a solar cell

q	elementary charge
Q	charge (C)
R	reflectance
r	radius
t	time
V	voltage
V _{oc}	open-circuit voltage
V _{fb}	flat band potential
V _m	maximum voltage in a solar cell
V _{sc}	short circuit voltage

Greek Symbols

α	absorption coefficient
β	angle
ϵ	extinction coefficient (Lmol ⁻¹ cm ⁻¹)
η	solar cell efficiency
λ	wavelength
μ	mobility
ν	frequency
τ	lifetime

LIST OF ACRONYMS AND ABBREVIATIONS

AM	air mass
CE	counter electrode
CB	conduction band
CV	cyclic voltammetry
FF	fill factor
HOMO	highest occupied molecular orbital
IMPS	intensity modulated photocurrent spectroscopy
IMVS	intensity modulated photovoltage spectroscopy
IPCE	incident photon-to-current conversion efficiency
IR	infrared
LUMO	lowest unoccupied molecular orbital
OC	open circuit
RE	reference electrode
SEM	scanning electron microscopy
SC	short circuit
TEM	transmission electron microscopy
UV	ultraviolet
VB	valence band
VIS	visible
WE	working electrode
XRD	X-ray diffraction

Chapter 1 Introduction

In the last years, energy demand on the world is increasing. The mainly source of energy is fossil fuels, which are becoming exhausted and causing environment pollution. Nuclear energy obtained from nuclear fission is dangerous and limited due to deficiency of heavy elements. Nuclear fusion has shortcomings in controlling the reaction and the formation energy. Some alternative energy sources such as water or wind are limited to areas with windy environments or flowing rivers. There is a need to find alternative forms of energy. Utilizing energy from the sun allows all parts of the world to use this energy. Solar energy presents as one of the best candidates.

The amount of solar energy from the sun to the earth is huge, i.e. 3×10^{24} J per year, about 10^4 times more than what humankind consumes currently. Solar energy emitted by the sun and reaching the earth's surface is a form of electromagnetic radiation that is available over a wide spectral range (300-2100 nm). In order to be used, the radiation needs to be converted into an energy form suitable for our needs.

Despite the significant development over the past decades, the high cost of manufacturing has remained a limiting factor on implementation of solar electricity in large scale. The commercial solar cells in the market are expensive and cost reduction of the electricity produced from solar cells is the principal objective for development material engineering in the nanometer scale. That could potentially lead to realization of low cost solar cells in the future.

1.1. Solar Cells

Solar cells convert directly solar energy into electricity. They required absorption of the sunlight and charge separation of electron-hole pairs that are created. The ability to absorb light is defined mainly by the band shape and the width of the bandgap, *Eg*. The separation and transport of the photo-generated free carriers are supported by the built-in electric field formed by the junction.

Crystalline silicon has become the dominant solar cell technology mostly due to its volume application in microelectronics. The solar cells that are commercially available today are made from solar grade silicon rejected by the microelectronics industry. This cell has the highest efficiency, 25% [1] and the silicon must be very pure and perfectly crystalline for photo-generated carriers to reach the contacts. The main problem with this kind of solar cells is its high cost of manufacturing. Other emerging semiconductor materials are the III-V and II-IV compounds, such as copper indium diselenide (CIS solar cells) and cadmium telluride (CdTe solar cells.) [2].

CIS solar cells comprise a heterojunction structure, built up by p-type semiconductors (CIS) with a thin n-type cadmium sulfide (CdS) layer. The reported laboratory efficiency is 21.5% [3]. The mainly advantage of CIS solar cells is the stable operation, without light induced degradation. However, the stability is not so good in hot and humid environments [4]. CdTe solar cells also have a heterojunction

structure, consisting of p-type CdTe and n-type CdS thin films, and its record laboratory efficiency is 16%. The main drawback of CdTe solar cells is the potential toxicity of cadmium [5].

During the past two decades, substantial progress in the photovoltaic field has significantly reduced the cost, improved the stability, and above all, continuously increased efficiency of all kinds of solar cells [6].

1.2. Dye sensitized solar cell (DSC)

Dye sensitization dates back to the nineteenth century, at the same time with photography invention. One of the pioneer works in dye sensitization of semiconductors was Vogel's study about silver halide emulsions sensitized with dyes in 1873[7]. Few years after, Dr. Moser in Vienna University reported the dye sensitized photoelectric effect. In the 1960s, the first experiment was carried out using single crystal semiconductor electrodes immersed into dye solution. This device exhibited conversion efficiencies of less than 0.5% and poor long-term stability for applications in water splitting systems [8]. In 1976, Tshubomura at al. reported 1.5 % energy conversion using dyed high porosity multi-crystalline ZnO cell [9].

The use of dye-sensitization in photovoltaics remained however rather unsuccessful until a breakthrough at the early 1990's in the Laboratory of Photonics and Interfaces in the EPFL Switzerland. By the successful combination of nanostructured electrodes and efficient charge injection dyes professor Grätzel and his co-workers developed a solar cell with energy conversion efficiency exceeding 7% in 1991 [10] and 10% in 1993[11]. This solar cell is called *the dye sensitized nanostructured solar cell* or *the Grätzel cell* after its inventor.

Titanium dioxide became the semiconductor of choice. This material has many advantages for sensitized photochemistry and photoelectrochemistry: cheap, widely available, non-toxic and biocompatible material, and as such is even used in health care products, as well as domestic applications such as paint pigmentation.

Due to the high efficiencies and good long-term stability reported for the dye-sensitized solar cells, the interest in this technology grew rapidly during the 1990's until now. While the patent holders and the licensees developed the original patented concepts towards practical products, numerous research groups explored the replacement of the original materials with new ones. Materials such as ZnO, SnO₂, Nb₂O₅, and In₂O₃. etc. have been widely investigated. Specifically, zinc oxide has received much attention due to its similar band-gap to that of titanium dioxide.

1.3. DSC based on ZnO

As I mentioned above, extensive studies have focused on investigating the proper substitute for the TiO₂ film, such as ZnO [12-15], In₂O₃ [16], Nb₂O₅ [17], and SnO₂ [18]. DSC with TiO₂ as the anode has achieved the highest efficiency of all semiconductor films. However, TiO₂ films have some limitations as difficulty to growing on a substrate with controlled structure. This may prevent further development of DSCs with TiO₂ films. Ordered one dimensional structure of metal oxides, such as rods or wires, will greatly improve DSCs efficiency [19]. Therefore, extensive attention has focused on looking for and studying the suitable substitute for TiO₂. Among these candidates, ZnO has been expected to be comparable to TiO₂ because of its higher electronic mobility, similar energy level of the conduction band

[13], conductive ZnO has been studied in this context. From a synthetic aspect, control of particle size, shape and composition by wet chemical methods is more readily achieved when preparing ZnO particles, whereas there are several problems making TiO₂ [14]. In earlier sixties many interest was focus in photoconductivity in dye sensitized ZnO. One of the first works was in 1950, mentioned in review references by Meier on dye sensitization from 1965 [20]. Gerischer and Tributsch [21, 22] made monocrystalline ZnO as photovoltaic device using ruthenium dyes. In 1976, a breakthrough in conversion efficiency was reported by Tsubomura et al. using dyed high porosity multi-crystalline ZnO cell of energy conversion 1.5%. They also found that the iodide/triiodide redox system was outperforming to obtain high conversion efficiencies [23].

Table 1.1 Compilation of the overall efficiencies reached in sensitized nanostructured ZnO solar cell [24]

Size/ thickness	film	Sensitizer	Intensity(Wm-2)	efficiency(%)
150 nm		N719	100	5
11 nm		N719	1000	4.1
10-20 nm		Mercurochrome	1000	2.5
5 nm		MDMO-PPV*	710	1.6
porous crystal		Eosin Y	1000	2.3
wires 100-150 nm		CdSe	360	2.3
wires 130-200 nm		N719	1000	1.5
ZnO sheets		N719	1000	3.9

* MDMO-PVP = poly[2-methoxy-5-(3',7'-dimethyloctyloxy)-1,4phenylenevinylene]

In table 1.1 it is summarized overall efficiencies reached with the dye sensitized nanostructured ZnO solar cell. DSC based on ZnO nanowires have not yet been able to give better performance than those based on spherical particles.

Other alternatives its use ZnO as an outer shell on nanoparticulate SnO₂ electrodes giving promising results (5-6% efficiency) using N719 dye [25, 26].

Nevertheless, the performance of dye sensitized ZnO solar cells in terms of solar-to-electrical energy conversion efficiencies is so far lower than that of TiO₂. This can be attributed to the much lower research activity on the use of ZnO. The main problem with ZnO at present is related to a complex dye sensitization process. Protons from carboxyl groups causes dissolution of Zn surface atoms with formation of Zn²⁺/ dye complexes in the pores of the nanostructured films. No approaches have been reported to overcome this problem. Thus, a large potential exists to improve on the performance of dye sensitized ZnO solar cells by learning how to use new types of anchoring groups and controlling the chemistry at the oxide/dye/electrolyte interface.

In this thesis is compared transfer transport and charge carrier on TiO₂ and ZnO solar cells, and study other parameters in performance of ZnO solar cells as different dye, time dye sensitization, electrolyte composition in order of get better efficiency. The first chapters are an introduction to semiconductors and theory about photochemistry. Third and four chapters are a brief description of the techniques used in the characterization of the material, and the operation principles of the equipments and solar cells devices. In the next chapter the morphology influence of ZnO nanoparticle compared with ZnO nanorod is analyzed. Also Li⁺ and Mg²⁺ were studied as dopants in the ZnO nanostructured films.

Finally the new dye D5, polyene-diphenylaniline compound, shows promissory results for performance of DSC ZnO.

Bibliography

- [1] J. Zhao, A. Wang, M.A. Green, *Prog Photovoltaics*, (1999), 7, 471-274.
- [2] S.K. Deb, *Sol. St.Mat.Sci.*, 3 (1998) 51-59.
- [3] J.S Ward, K. Ramanathan, F.S. Hasoon, T.J. Coutts, J. Keane, M.A. Contreras, T. Moriarty, R. Noufi, *Progress in Photovoltaics: Research and Applications*,10 (2002) 41-46.
- [4] B. Dimmler, in: J. Schmid et al. (Eds.), *Proceedings of the 2nd World Conference on PV Solar Energy Conversion*, European Commission, Ispra, Italy, (1998), pp. 419-423.
- [5] V.M. Fthenakis, P.D. Moskowitz, *Progress in Photovoltaics: Research and Applications*, 3 (1995) 295-306.
- [6] T. Surek, *J.Crys. Grow.*, 275 (2005) 292-304.
- [7] A.J.McEvoy and M.Grätzel,*Sol.Ener.Mater.*, 32, (1994), 221-227
- [8] D.F. Watson, G.J. Meyer, *An. Rev. Phys.Chem.*, 56 (2005) 119-156.
- [9] H. Tsubomura, M. Matsumura, Y. Nomura, T. Amamiya, *Nature* (1976), 261, 402.
- [10] O'Regan, B.; Gratzel, M. *Nature (London, United Kingdom)* 353(1991), 737-40.
- [11] M.K. Nazeeruddin, A. Kay, I. Rodicio, R. Humphry-Baker, E. Müller, P. Liska, N. Vlachopoulos and M. Grätzel, *J.Am.Chem.Soc.*,115(1993),6382-6390,
- [12] K. Keis, E. Magnusson, H. Lindstrom, S.-E. Lindquist, A. Hagfeldt, *Sol. Energy Mat.Sol. Cells* ,73 (2002), 51-58.
- [13] C. Bauer, G. Boschloo, E. Mukhtar, A. Hagfeldt, *J.Phys.Chem. B*, 105 (2001) 5585-5588
- [14] Z.W.Wang, *Characterization of Nanophase Materials*, Wiley VCH, Wienheim, (2000)
- [15] K. Hara, T. Horiguchi, T. Kinoshita, K. Sayama, H. Sugihara, H. Arakawa, *Sol. Energy Mat. Sol. Cells*, 64(2000), 115-134.
- [16] R. Katoh, A. Furube, T. Yoshihara, K. Hara, G. Fujihashi, S. Takano, S. Murata, H. Arakawa, M. Tachiya, *J.Phys. Chem. B*, 108 (2004) 4818-4822.
- [17] K. Sayama, H. Sugihara, H. Arakawa, *Chem.Mater.*, 10(1998) 3825 -3832.
- [18] Y. Tachibana, K. Hara, S. Takano, K. Sayama, H. Arakawa, *Chem. Phys. Lett.* 364 (2002), 297-302.
- [19] J.B. Baxter, A.M. Walker, K van Ommering, E.S. Aydil, *Nanot.* 17 (2006,) S304-S312.
- [20] H.Meier, *J.Phys.Chem.*,69,3,(1965) 719-729
- [21] H.Gerischer and H.Tributsch, *Ber.Bunsenges.Phys.Chem.*,72 (1968) 437-445
- [22] H.Tributsch and H.Gerischer, *Ber.Bunsenges.Phys.Chem.*,73 (1969) 850-854
- [23] H.Tsubomura,M.Matsumura,Y.Nomura and T.Amamiya, *Nature*,261(1976)402-403
- [24] T.Soga,"Nanostructured Materials for Solar energy Conversion", Elsevier, Amsterdam, (2006)
- [25] D.Niinobe, Y.Makari, T.Kitamura, Y.Wada and S.Yanagida, *J.Phys.Chem. B*,109(2005) 17892-17900
- [26] A.Kay and M.Grätzel,*Chem .Mater*,14(2002)2930-2935

Chapter 2 Photochemistry of semiconductor

General properties of the different components in a DSC device, semiconductors, electrolyte solutions, semiconductor electrolyte interfaces and the interaction between ZnO semiconductor, a dye and electrolyte are reviewed in this chapter.

2.1. Semiconductors

Semiconductors are materials whose electrical conductivity increases with temperature and is significantly lower than metals; general properties of these materials and applications are described in several textbooks [1-3].

The interesting semiconductors are solid (generally oxides or chalcogenides) where atoms are an infinite three-dimensional network. Overlapping the atomic orbitals exceeds the first neighbors, spreading throughout the network; then it is a configuration of delocalized states in close proximity among them, forming bands of permitted electronic states. Construction of electronic configuration is shown in Figure 1. Between bands, there are intervals in the energy where electronic states are not "permitted"; each of these intervals is an "energy prohibited band" or gap. The bands that limit the gap are the valence band (VB), with lower energy and the conduction band (CB), with more energy. There are so many levels as electronic atoms in the network. For an infinite network, the difference between two electronic states is virtually non-existent and the electronic configuration it is expressed as bands from the function of density states. The role of density states (DS) representing a count of electronic levels within an interval of infinitesimal energy.

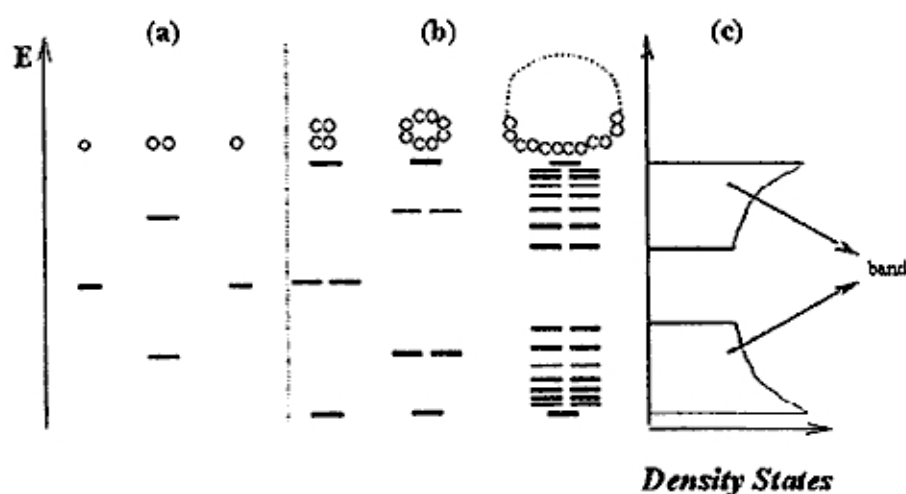


Figure 2.1 Electronic levels resulting from the bonding between identical atoms. (a) molecular orbital resulting of two atoms overlapping, with a single atomic orbital; (b) chains of 4, 6 and N atoms. (c) The energy of density of states (DS) for an infinite chain of atoms.

In the ground state and 0 K, electrons occupy these electronic states (two electrons with opposite spin for each state) to a certain amount of energy, E_F , leaving states with energy greater than E_F unoccupied, as shown in Figure 2.1. The Fermi energy, E_F , coincide at 0 K with the chemical potential of electrons.

At higher temperatures, thermal excitation promotes electron levels above E_F , and the fraction of occupied states extends to $E_F + k_B T$ (k_B is the Boltzmann constant and T temperature).

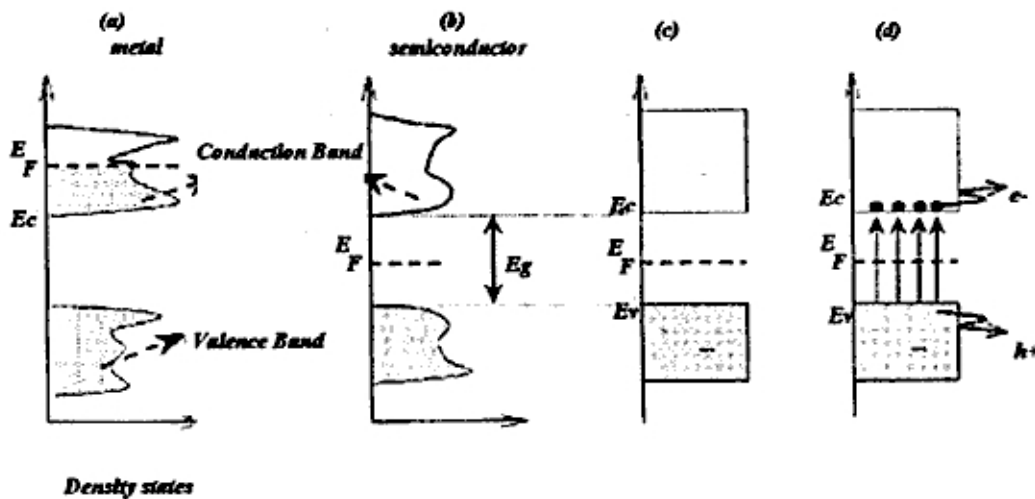


Figure 2.2 Band diagram and electronic distribution of electrons at 0°K to a metal (a) and for a intrinsic semiconductor (b). Simplified diagram of the bands structure and electronic distribution for a intrinsic semiconductor at 0 K (c) and $T > 0^\circ\text{K}$. The grey color indicates states occupied by electrons; E_F is the Fermi energy.

The position of the Fermi level respect to the valence and conduction band distinguishes metals, semiconductors and insulators. In metals, E_F falls in the conduction band while for semiconductors and insulators, falls into the band gap. The difference between a semiconductor and an insulator is given by the width of the forbidden band of energy, E_g . For semiconductors E_g is sufficiently small as it is possible to excite (heat, light or electric shock) electrons from the valence band to the conduction band.

Material conductivity is directly related with carrier charge existence. In metals, charge carriers are the electrons on the partial full band conduction, in semiconductors the carriers are the electrons in the conduction band and holes in the valence band. Electrons and holes have opposite charge; in consequence they are accelerated in opposite direction under electric field (Figure 2.2)

2.1.1. Density of electrons and holes

The density of carriers on VB and CB is zero at 0° K when the material is insulator. With increasing temperature some electrons are excited from the VB to CB occurring simultaneously increasing the electrons concentration in CB and holes in VB (Figure 2d). The electron density, n , and holes, p , in the conduction and valence band, respectively,

are given by Equations (2.1), in which N_c and N_v are densities of states in the CB and VB, respectively.

$$n = N_c \exp\left(-\frac{E_c - E_F}{k_B T}\right)$$

$$p = N_v \exp\left(-\frac{E_v - E_F}{k_B T}\right)$$
(2.1)

The charge carrier product then results in equation (2.2), where n_i is a characteristic constant for each material that depends on E_g . For an intrinsic semiconductor, without impurities or defects $n_i = n = p$

$$n \times p = N_c N_v \exp\left(\frac{E_v - E_c}{k_B T}\right) = N_c N_v \exp\left(\frac{-E_g}{k_B T}\right) = n_i^2 = cte$$
(2.2)

2.1.2. Localized States for impurities and vacancies

Substitution of some atoms with solid impurities (in the order of 1 atom per each 10^9 host atoms) introduces levels localized whose energy falls within the band gap.

Excess of electrons provided from donor atoms are located in states with energy, E_d , near the bottom of the conduction band. These atoms can be oxidized, transferring electrons to the CB. The presence of these donors impurities increasing the density of electrons in CB ($n \gg n_i \gg p$). For n-type semiconductors the majority charge carriers are electrons (Figure 3b). Similarly, acceptors impurities, deficient in electrons with respect to materials, generate empty localized levels of energy, E_a , near VB. These atoms can be reduced taking electrons from the VB and increasing the density of holes (decreases the electron concentration) VB ($p \gg p_i \gg n$). In p-type semiconductors the majority charge carriers are holes.

The relative position of the Fermi level (chemical potential of charge carriers) depending on the concentration of electrons and holes, i.e. doping of semiconductor (Figure 2.3b) is given by equation (2.3):

$$E_F = E_{F,i} + K_B T \ln\left(\frac{n}{n_i}\right)$$
(2.3)

Typical charge carrier densities for the semiconductor varies from 10^{15} to 10^{19} cm^{-3} , corresponding to levels of Fermi, E_F , located 0.04 - 0.25 eV above (semiconductor p) or below (semiconductor n) of the closer band [4]. In a n-type semiconductor with all donor impurity ionized, concentration of electron in the conduction band is approximately equal to the concentration of impurities, N_d . Since the product $n \times p$ is constant (2), the concentration of holes decreases in respect of a semiconductor intrinsic ($n \approx N_d \gg n_i = p_i \gg p$).

The defects in the material, such as vacancies, also introduce ionizable states. This is the case of various oxides and chalcogenides (ZnO , Fe_2O_3 and TiO_2 , CdS) that are

thermodynamically stable as not stoichiometric compound, without the anion. This shortcoming implies the presence of anionic vacancies around of which the deficit of negative charge is offset by a reduction of positive charge from the cations around them. In the case of TiO_2 , which should formally written TiO_{2-x} , oxygen vacancies are offset by formally adopting the state oxidation +3 by an equivalent number of atoms of titanium. In reality, these ion Ti^{3+} acted as donor electron, and the material is a semiconductor type n.

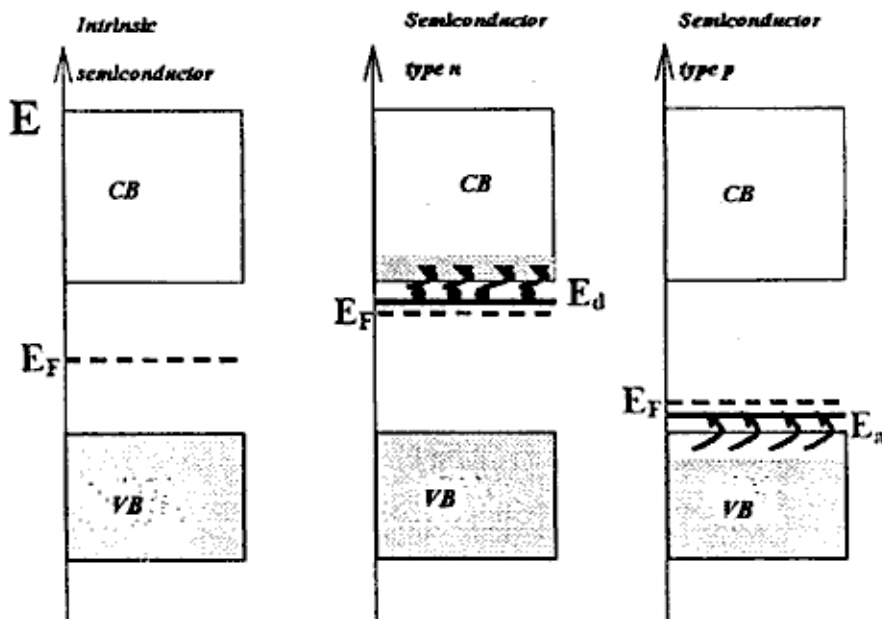


Figure 2.3. Position of the Fermi level and density of states occupied for intrinsic semiconductor type n and type p.

2.1.3. ZnO crystalline structure

ZnO is an important wide band-gap II-VI compound semiconductor. It has a wurtzite structure. The structure consists of hexagonal Zn and O planes stacked alternatively along the c-axis (see Fig. 2.4). The basic materials parameters of ZnO are shown in Table 2.1 [5].

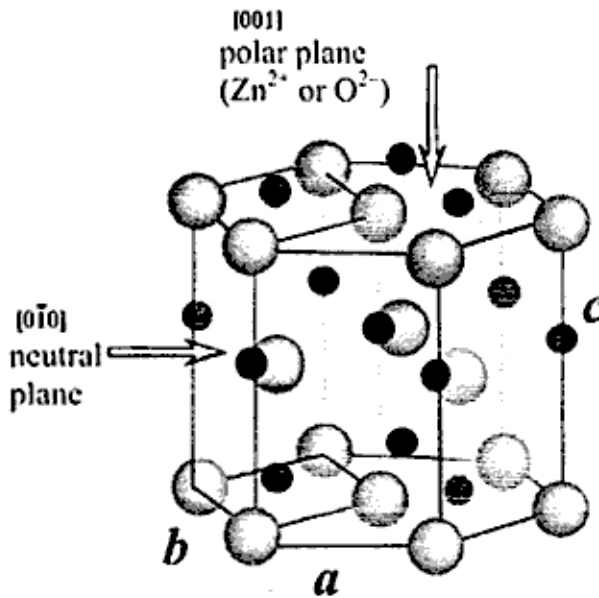


Figure 2.4. Unit cell of ZnO. Zn²⁺ are represented in black, O²⁻ anions in grey

ZnO has several advantages over other materials [6]. Firstly, ZnO is a semiconductor with a direct wide band-gap of 3.37eV, and a large exciton binding energy of 60 meV that is greater than the thermal energy at room temperature (25 meV). The lack of a center of symmetry in the wurtzite (a crystal structure of ZnO) combined with large electromechanical coupling, results in strong piezoelectric, which is a property in building electromechanical-coupled sensors and transducers, and it is bio-safe and biocompatible, and can be used for biomedical applications without coating. ZnO is also transparent to visible light and can be made highly conductive by doping metals, such as Al, Cd, and Sn.

Table 2.1. Properties of wurtzite ZnO.

Property	Value
Stable phase at 300 K	wurtzite
Lattice parameters at 300 K:	0.32495 nm
a_0	0.52079 nm
c_0	1.602 (1.633 for ideal hexagonal structure)
a_0/c_0	
Density	5.606 g/cm ³
Melting point	1975 °C
Thermal conductivity	0.6, 1-1.2
Linear expansion coefficient (1/°C)	$a_0: 6.5 \times 10^{-6}$, $c_0: 3.0 \times 10^{-6}$
Static dielectric constant	8.656
Refractive index	2.008, 2.029
Energy gap	3.4 eV (direct)
Intrinsic carrier concentration	$< 10^{6,3} / \text{cm}^3$

Exciton binding energy	60 meV
Electron effective mass	0.24
Electron Hall mobility at 300 K for low n-type conductivity	$20 \text{ cm}^2/\text{V.s}$
Hole effective mass	0.59
Hole Hall mobility at 300 K for low p-type conductivity	$5.50 \text{ cm}^2/\text{V.s}$

2.2. Electrolyte

Electrolyte has an important role in a dye sensitized solar cell because permit regeneration of sensitizer. Redox couples dissolved in an organic solvent component electrolyte.

The dissolved redox systems has empty and occupied energy levels, which are comparable to the conduction and valence bands in the solid semiconductor, respectively. According to the distribution of energy levels associated with redox couple the tendency to donate or accept electrons when the redox molecules approach the solid electrode is defined. Fluctuations in the solvation shell surrounding the redox molecules causes its energy states are distributed over a certain range. Assuming a harmonic oscillation of the solvation shell, the density of occupied states (D_{red}) and the density of empty states (D_{ox}) can be described by Gaussian functions [7] (see Figure 2.5). In consequence the energy position of the level of dissolved oxidized and reduced forms is in the maximum of the Gaussian function.

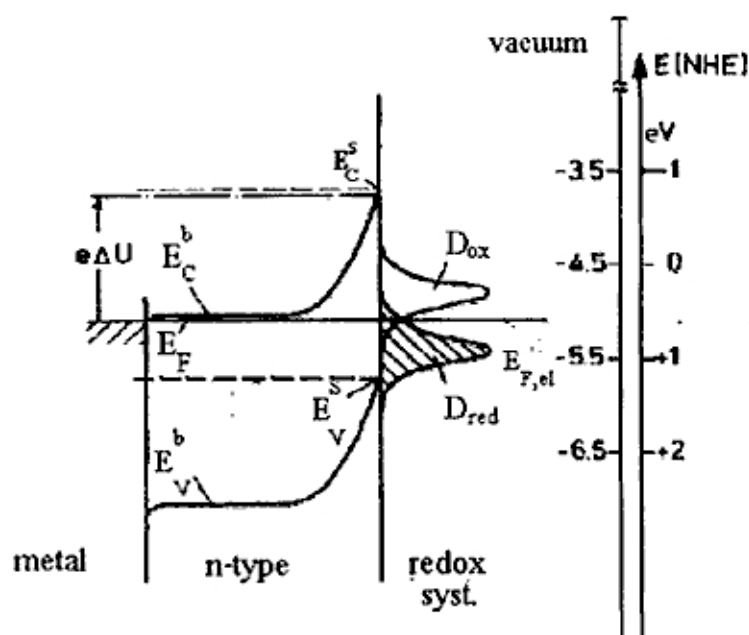


Figure 2.5 Energy states of semiconductor electrodes and redox systems [7].

The solution redox potential of the redox couple $E_{red/ox}$ is represented for the intersection point of the distribution of oxidized and reduced species and since this point the stage where the probability of a level being occupied by an electron is $1/2$, $qE_{red/ox}$ can be considered as the Fermi level in the liquid phase. $E_{red/ox}$ potential can be calculated using the Nernst equation:

$$E_{\text{red/ox}} = E^{\circ}_{\text{red/ox}} + \frac{R}{nF} T \ln \frac{\{\text{ox}\}}{\{\text{red}\}}$$

Where n is the number of electrons transferred in the redox reaction, R is the gas constant, T is temperature, F is faraday's constant and $\{\text{ox}\}$ and $\{\text{red}\}$ are the activities of the oxidized and reduced species of the redox molecule.

The redox potential of the normal hydrogen electrode is defined as zero, for a semiconductor the vacuum level is the zero in absolute scale.

In dye sensitized solar cells the redox couple used is I^-/I_3^- . The iodide (I^-) prevents the recombination of the electron by the oxidized dye and the (I_3^-) uptakes the electrons at the counter-electrode.

2.3. Dyes

The absorption of incident light in the DSCs is realized by dye molecules placed on the semiconductor electrode surface. To achieve a high light-to-energy conversion efficiency in the DSC, the properties of the dye molecule as attached to the semiconductor particle surface are essential. To minimize the energy losses and to maximize the photovoltage, the excited state of the adsorbed dye molecule should be only slightly above the conduction band edge of semiconductor but above enough to present an energetic driving force for the electron injection process.

The dye sensitization process has an important role in the preparation of DSC. For TiO_2 films dye sensitization is achieved by immersing the electrode in ethanolic dye solution. Carboxyl groups are commonly used as anchoring groups for chemisorption of dye molecules onto metal oxide surfaces [8]. The strong chemisorption of the carboxyl groups to the surface favors monolayer growth on TiO_2 .

Sensitization of ZnO may be described by the following process [9], see Figure 2.6: diffusion of the dye into ZnO film, adsorption of the dye to the ZnO surface, dissolution of Zn surface atoms from ZnO and formation of Zn^{2+} /dye complexes in the pores of ZnO [10]

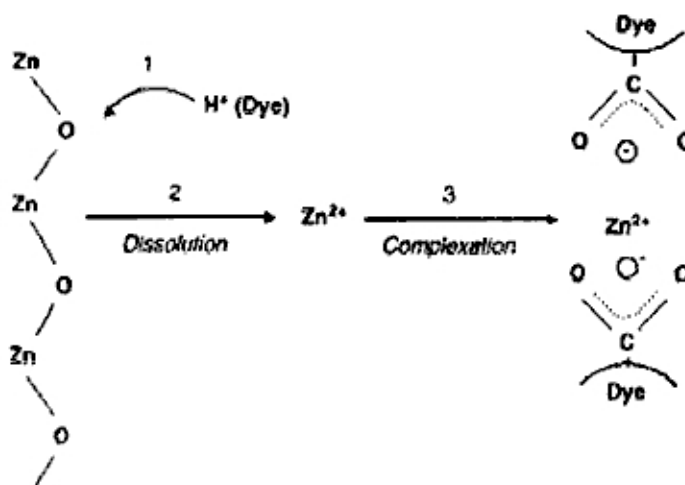


Figure 2.6 A schematic picture of the problem associated with the dye sensitization of protoned anchoring groups on ZnO surfaces

The complex formation between Zn^{2+} ions from ZnO surface and different dyes have been reported in the literature [11]. Due to this situation, it is important the control of the dye composition, concentration, pH and sensitization time, in order to avoid the Zn^{2+} /dye complex formation.

In this thesis two dyes were used *cis*-di(thiocyanato)-bis(2,2'-bipyridyl-4-carboxylate-4'-carboxylic acid)-ruthenium(II) or N719 and the polyene-diphenylaniline or D5 (see Figure 2.7). The latter was synthesized at the Center of Molecular Devices [12]. In this dye (D5) the diphenylaniline moiety acts as an electron donor and the cyanoacetic moiety acts as the electron acceptor and as anchoring groups for attachment on the TiO₂. Measuring the incident to photon current efficiency (IPCE), the highest values obtained for D5 were 85% at 400 nm and 70–65% at the plateau between 450–600 nm for an electrolyte without the additive 4-*tert*-butyl pyridine (4-TBP)

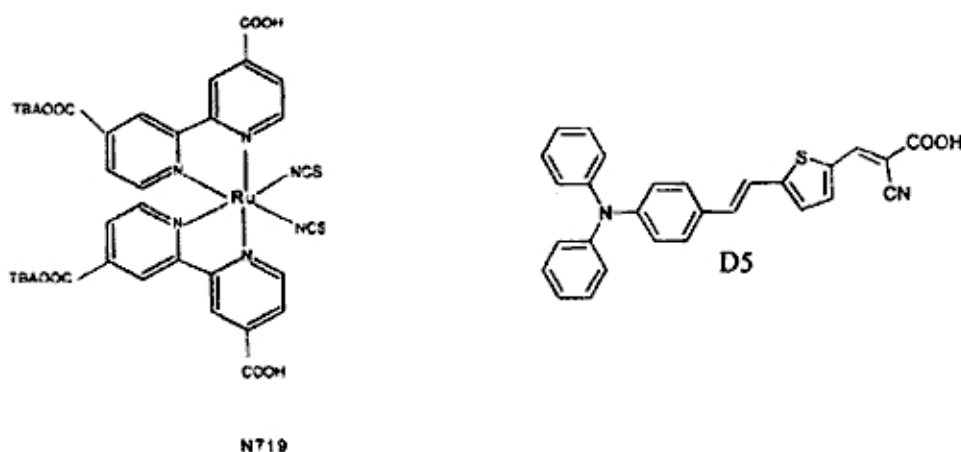


Figure 2. 7 Molecular structure of different dyes a) N719 and b) D5

2.4. Semiconductor-electrolyte interface

If two phases, with electroactive species, with different electrochemical potentials, are brought into contact, they tend to equilibrate by exchanging charges. Electrons will flow from material with the highest Fermi level until $E_f = E_{redox}$. Charged planes are formed at the interface. There are three double layers at the semiconductor/electrolyte interface controlling the electrical and chemical properties of the surface: the space charge layer in the semiconductor, formed when electrons are transferred from the semiconductor to the electrolyte. The second, the Helmholtz double layer, formed between the semiconductor and the position of closest approach of nonadsorbed solvated ions and the last, Gouy-Chapman layer associated with the field created by the mobile solvated ions near the surface.

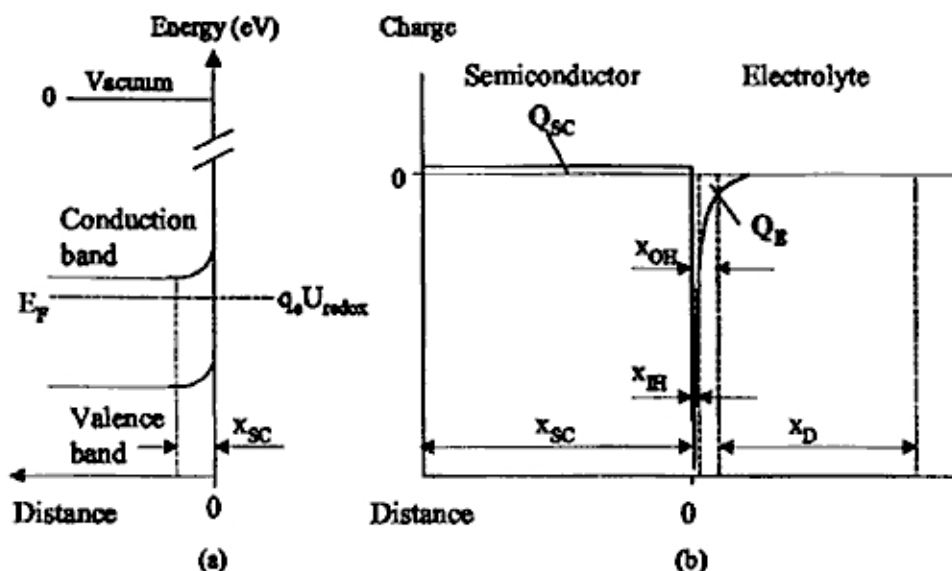


Figure 2.8. (a) energy level diagram for an n-type semiconductor in contact with electrolyte and (b) a schematic representation for charge (Q) distribution at semiconductor/electrolyte interface

A space charge is formed for charged impurities near the surface of the semiconductor or trapped carriers, also mobile electrons or holes in the conduction or valence band of the semiconductor. If the majority of carriers are extracted, the surface region is depleted of mobile carriers then the surface region is ionized. A depletion layer is formed and the space charge (Q_{sc}) is the immobile charge of ionized donors. The excess charge can be distributed over considerable distance below the interface (x_{sc}). Band bending is formed as results of electrical field by the difference of potential between the surface and the bulk of the semiconductor (Figure 2.8).

The Helmholtz double layer is considered to be formed between two planes of charge. One plane is due to charges at the surface of the solid. Charge can arise from accumulation of free charge, adsorbed ions or free charge trapped from the solid onto surface states. The other plane is due to ions in solution attracted by the charged surface. Solvated ions can only approach the solid to a distance x_{OH} and the locus of centres of these nearest solvated ions is called the outer Helmholtz plane. The layer of adsorbed solution species at the solid surface is called the inner Helmholtz plane. Q_H is the excess charge in Helmholtz layer.

The region in the solution near the electrode in which there is a space charge due to an excess of free ions of one sign is called Gouy Chapman layer. The thickness of the diffusive layer (x_D) depends on the total ionic concentration in the solution. Concentrated solution produces a extremely thin layer and melted into the outer Helmholtz plane. The excess charge in diffuse layer is Q_D , and the total excess charge on the electrolyte side of the double layer Q_E

$$Q_E = Q_H + Q_D = Q_{sc}$$

At equilibrium Fermi level of the semiconductor shift to the position of the redox potential in the electrolyte, in consequence electrolyte plays an important role in determining electrochemical equilibrium potential.

Bibliography

- [1] L. Smart y E. Moore Addison, "Química del estado Sólido: Una introducción", Wesley, Iberoamericana, Wilmington, USA, (1995).
- [2] P.A. Cox, "The Electronic Structure and Chemistry of Solids" Oxford Univ. Press, Oxford, (1987).
- [3] N.S. Lewis, M.L. Rosenbluth, "Photocatalysis, Fundamentals and Applications"; N. Serpone, E. Pelizzetti, Caps. 3 y 4, Eds.; John Wiley, New York, (1989).
- [4] A.J. Nozik, R. Memming, *J. Phys. Chem*, 100, 13061, (1996).
- [5] D.P. Norton, Y.W. Heo, M.P. Ivill, K. Ip, S.J. Pearton, M.F. Chisholm, T. Steiner, *Mater. Today* 7, 6 (2004) 34-40.
- [6] Z.L. Wang, "Nanostructures of zinc oxide", *Mater. Today*, 7, 6 (2004) 26-33.
- [7] R. Memming, *Electrochim. Acta* 25:77(1980)
- [8] M.K. Nazeeruddin, A. Kay, I. Rodicio, Humphry-Baker, R. Müller, E. Liska, P. Vlachopoulos, N. and Grätzel, M. *Chem. Rev.* 95(1995)49-68
- [9] Soga, T., *Nanostructured materials for solar energy conversion*, Elsevier, Amsterdam, (2006)
- [10] K. Keis, J. Lindgren, Linquist S-E and Hagfeldt, A. *Langmuir*, 16(2000)4688-4694
- [11] R. Baumeler, P. Rys, and H. Zollinger, *Helv. Chim. Acta*, 56(1973)2451
- [12] D. Hagberg, T. Edvinsson, T. Marinado, G. Boschloo, A. Hagfeldt and L. Sun, *Chem. Commun.*, (2006), 2245-2247

Chapter 3 Principles of dye sensitized solar cells

In this chapter the principles of the dye-sensitized solar cells is introduced starting with a short description of the operating process of the cell. After this, a more detailed look is taken to the cell operation in light of the key steps of photovoltaic conversion, as well as the other important fundamental operational aspects of the cell physics and chemistry (transport and kinetics).

3.1. Operational principles

Conventional solar cells convert light into electricity by exploiting the photovoltaic effect that exists at semiconductor junctions. Two materials with different conduction mechanism, either n and p type have a charge separation at an interface. Photovoltaic devices are based on this concept where electrons and holes are majority carriers in a single semiconductor material, heterojunctions between different semiconductors or semiconductor-metal junction (Schottky).

The dye sensitized photoelectrochemical cells work on a different principle, whereby the processes of light absorption and charge separation are differentiated. Light absorption is performed by a monolayer of dye (D) absorbed chemically at the semiconductor surface (Figure 3.1). After having been excited (D^*) by a photon of light, the dye is able to transfer an electron to the semiconductor by a process called *injection*. Electrons in the semiconductor are collected through their transport in the electrode. This transport occurs mainly by diffusion [1-3]. The original state of the dye is subsequently restored by electron donation from the electrolyte, usually an organic solvent containing redox system, such as the iodide/triiodide couple. This process called *regeneration*.

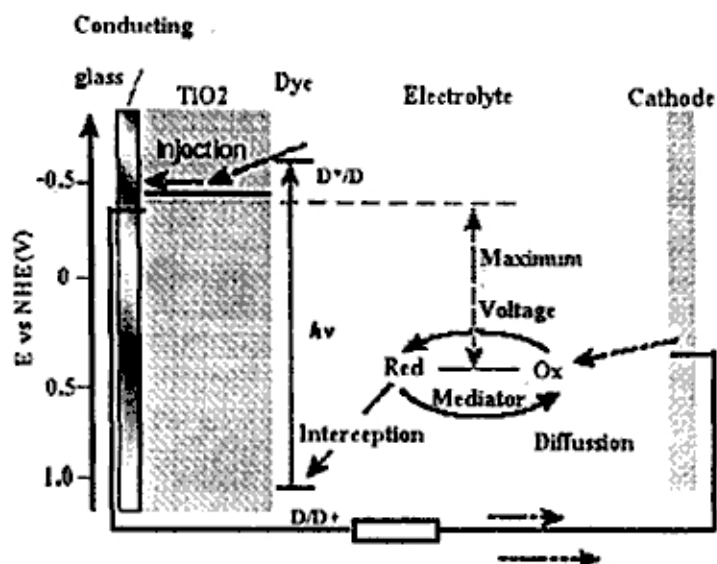


Figure 3.1. Schematic of operation of the dye-sensitized electrochemical photovoltaic cell. The photoanode, made of a mesoporous dye-sensitized semiconductor, receives electrons from the photo-excited dye which is thereby oxidized, and which in turn oxidizes the mediator, a redox species dissolved in the electrolyte. The mediator is regenerated by reduction at the cathode by the electrons circulated through the external circuit.

The regeneration of the sensitizer by iodide intercepts the recapture of the conduction band electron by the oxidized dye. The iodide is regenerated in turn by the reduction of triiodide at the counter electrode, the circuit being completed via electron migration through the external load. The theoretical maximum voltage (ΔV) that such a device could deliver corresponds to the difference between the redox (Nernst) potential of the mediator and the quasi-Fermi level of the electrons in the semiconductor.

3.2. Energetics

The electron transfer mechanism is strongly dependent on the electronic structure of the adsorbed dye molecule and the energy level matching between the excited state of the dye and the conduction band of the semiconductor.

The dye molecules have usually acid groups (COOH) as attachment units and upon binding a proton (H^+) is released to the oxide surface leaving the dye molecule negatively charged. The potential difference across the consequently formed Helmholtz's layer is estimated to be approximately 0.3 eV, and it will help to separate the charges and to reduce recombination [4].

The major mechanism for the charge separation is however the energy level positioning (Figure 3.2) between the dye molecule and the nanoparticle. The excited state of the dye (the LUMO level) is above the conduction band edge of the semiconductor and the dye's HOMO level is below the chemical potential of the redox pair iodide/triiodide in the electrolyte, both presenting an energetic driving force for the electron and hole separation.

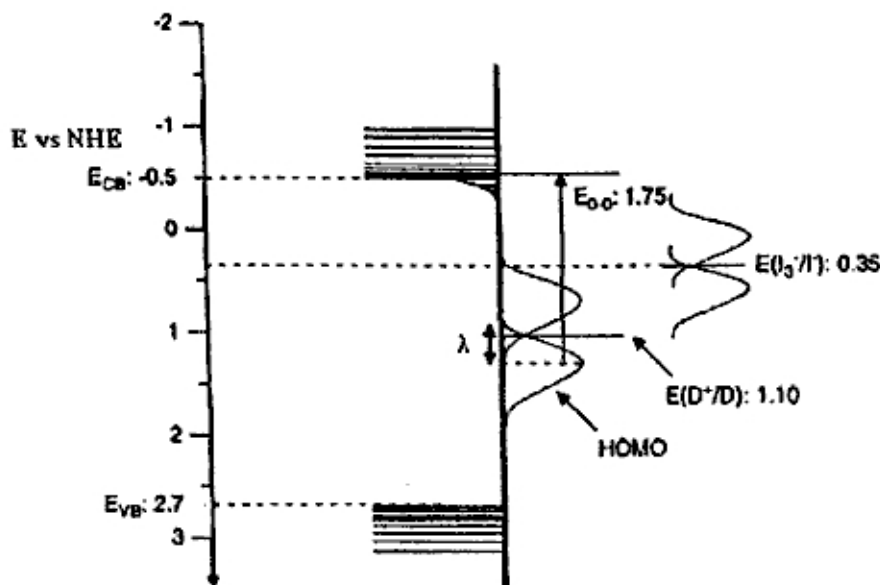


Figure 3.2 Schematic diagram of the energetics in a solar cell with ZnO, N719 and I⁻/I₃⁻ electrolyte [5]. The energy level distribution of the energy states in solution are illustrated as Gaussian distribution. The electronic excitation of the dye is most likely from the average energy level in the ground state distribution. The HOMO is estimated via the oxidation potential of the dye and the reorganization energy, λ . The zeroth-zero transition ($E_{0,0}$) is determined via the normalized intercept of the absorption and emission spectra.

In addition to the favorable energetics for the charge separation, also entropic factors arise. The large density of delocalized states in the nanoparticle compared to small number of dye molecules on the particle surface means that the electron injection to the semiconductor conduction band is associated with an entropy increase presenting a driving force of approximately 0.1 eV for the charge separation [4].

The maximum voltage that can be obtained from DSC is given by the potential difference between the conduction band edge and the redox potential. An overview of the energetics of the dye sensitized nanostructured ZnO solar cell is shown in Figure 3.2. Photoelectron spectroscopy (PES) and electrochemistry are experimental methods for determine the energetics in DSC. PES has been used to study the energy level matching for Ru(dcbpyH₂)₂(NSC)₂ adsorbed on nanostructured ZnO compared with the same complex adsorbed on TiO₂[6]. ZnO and TiO₂ have similar band gap, that indicates the energy matching between the dye and the metal oxide is similar for both semiconductors.

3.3. Light absorption

For the absorption of solar rays by a sensitizer attached as a monolayer to the surface of an oxide film there is a fundamental problem of the limited light-capture cross-section of the dye molecule.

The cross section σ is related to the molar extinction coefficient ϵ by the formula:

$$\sigma = \frac{\epsilon \cdot 1000}{N_A}$$

Typical ϵ values for dyes lie between 10^4 and $5 \times 10^5 \text{ M}^{-1} \text{ cm}^{-1}$ yielding for the light-capture cross-section values between 0.0016 and 0.08 nm²[7]. The area of the sensitizer molecule

occupies on the surface of the supporting oxide is much larger, e.g., about 1–2 nm². [7] Hence, at most a few percent of the incident light can be absorbed. A successful strategy to solve the problem of light absorption through such molecular layers is found in the application of high surface area films consisting of nanocrystalline oxide particles with a diameter of 10–20 nm. [8] The mesoporous morphology of the layer plays a crucial role in the harvesting of sunlight. Depending on film thickness, their real surface area can easily be made 100–1000 times larger than the apparent one.

When light penetrates the dye-covered oxide “sponge”, it crosses hundreds of adsorbed dye monolayers. Thereby, photons whose energy is close to the absorption maximum of the dye are completely absorbed. [9] The mesoporous structure thus mimics the light absorption by green leaves. As the chlorophyll-containing thylakoids are stacked, visible light is absorbed completely by traversing many superimposed vesicles containing the dye.

While the high efficiency of the dye sensitized solar cell arises from a collective effect of numerous well-tuned physical-chemical nanoscale properties as will become apparent later, the key issue is the principle of dye-sensitization of large band-gap semiconductor electrodes.

3.3.1. Light absorption via MLCT excitation

The absorption of a photon by the dye molecule happens via an excitation between the electronic states of the molecule.

The excitation of the Ru complexes via photon absorption is of metal to ligand charge transfer (MLCT) type (Figure 3.3). This means that the highest occupied molecular orbital (HOMO) of the dye is localized near the metal atom, Ru in this case, whereas the lowest unoccupied molecular orbital (LUMO) is localized at the ligand species, in this case at the bipyridyl rings. At the excitation, an electron is lifted from the HOMO level to the LUMO level. Furthermore, the LUMO level, extending even to the COOH anchoring groups [10] is spatially close to the TiO₂ surface, which means that there is significant overlap between the electron wavefunctions of the LUMO level of the dye and the conduction band of TiO₂. This directionality of the excitation is one of the reasons for the fast electron transfer process at the dye-TiO₂ interface.

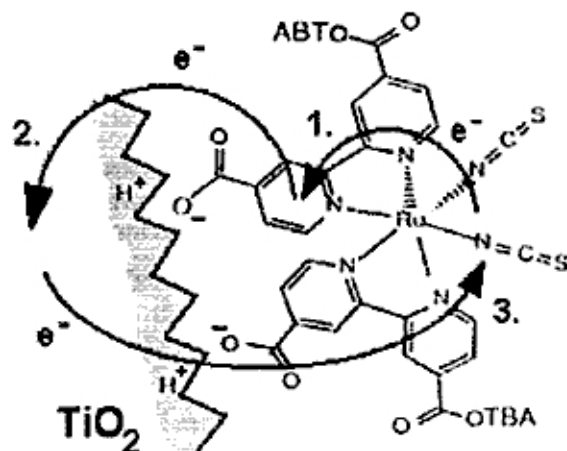


Figure 3.3 Charge transfer processes between dye and the TiO₂ lattice: 1. MLCT excitation, 2. Electron injection and 3. Charge recombination.

There are few studies about photoinjection in dye sensitized ZnO. Lian and coworkers reported multiple exponential electron injection from Ru-polypyridyl complexes into ZnO [11,12]. Faster electron injection is found with dye sensitized TiO₂, that was explained by differences in electronic coupling and density of acceptors levels. For dye sensitized ZnO, aggregation of dye is a problem. Solar cell efficiency depends strongly on both ZnO preparation and dye adsorption. Dye aggregation is expected to affect electron injection kinetics in ZnO.

3.4. Charge Transport

In the DSCs charge transport happens by electron transport in the nanostructured electrode and hole transport in the electrolyte as I₃⁻. Although the electron transport process has attracted an intensive study due to several interesting fundamental questions concerning it, both charge transport mechanisms are equally important for the operation of the solar cell.

The electrode can be viewed as a network of individual particles through which electrons percolate by hopping from one particle to the next [10]. Recombination processes being efficiently blocked at the semiconductor electrolyte interface the generation of electrons to the conduction band of the TiO₂ particles under illumination results in an electron concentration gradient in the electrode and the electrons are transferred to the transparent conductive oxide, TCO, back contact layer by diffusion.

Measurements have shown that the diffusion of electrons is characterized by a distribution of diffusion coefficients, which have been related to hopping of electrons via surface traps of different depths [10]. These electron traps are localized energy states just below the conduction band edge of the TiO₂ and they play a significant role in the electron transport. Because of the majority carrier nature of the TiO₂ electrode, trapping of electrons in the bulk states does not lead to recombination losses. Instead trapping of electrons at the TiO₂ surface may be a pathway for recombination, resulting in photocurrent losses and also photovoltage losses for kinetic reasons [13]. In addition, the trap states will lead to a lower quasi-Fermi level for the electrons under illumination and thus to a reduced photovoltage [13].

For nanostructured ZnO films, electron transport has been studied using different techniques such as photocurrent transients, Intensity Modulated Photocurrent Spectroscopy (IMPS) and conductivity measurements. Using photocurrents transients measurements, Hoyer and Weller found photocurrent response, on bare ZnO electrodes, became faster with more negative applied potentials. Solbrand et al. [14] found similar results and showed that transport time was dependent on electrolyte concentration becoming faster with higher concentrations.

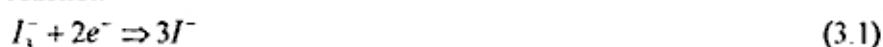
Electron transport becomes faster with increasing light intensity in dye sensitized ZnO solar cells, as is the case for nanostructured TiO₂. Recent studies suggest that the porosity of the electrodeposited films increases with films thickness [15], the films therefore consist in two parts: the porous outer part where electron transport is governed by diffusion and the inner part show field-driven electron transport.

3.4.1. Recombination

Recombination of the generated electrons with holes in the dye-sensitized nanostructured semiconductor electrode can in principle occur both after the electron injection and during its migration in the electrode on its way to the electrical back contact. Illumination

of the dye-sensitized electrode initially in equilibrium (in the dark) generates a transient electric field between the injected electrons in the semiconductor and the oxidized species in the electrolyte. This electric field could in principle oppose further charge separation and promote recombination. However, in the dye cell the mobile ions in the electrolyte can easily rearrange and effectively screen the light induced opposing fields in steady state conditions through out the electrode film, and thus enable an efficient charge separation [16].

In the absence of holes in the semiconductor particles, the recombination occurs mostly by loss of electron to an oxidized dye molecule or to a hole in the electrolyte, i.e. the oxidized triiodide. The former process is negligible, as assumed in most electrical models of the cell, but may be important in near open circuit conditions, i.e. in the case of the accumulation of electrons into the TiO₂ particles [17]. The latter recombination pathway on the other hand, is made inefficient by reaction kinetic reasons. According to Huang [18] the net recombination reaction at the TiO₂ - electrolyte interface is a two electron reaction



composed for subreactions



the last of which is a slow dismutation reaction and rate limiting in the net recombination reaction. The reaction equation 3.2 also tells that the actual electron acceptor in the recombination reaction is I₂.

For ZnO system, little information is available on recombination between oxidized dye molecules and electrons. Nevertheless similar behavior is observed with TiO₂ system [19,20]. Bauer et al [19] found that recombination kinetics of both N719-ZnO and N719-TiO₂ systems under identical conditions could be fitted to a biexponential function with time constants of about 0.3 (50%) and 300μs(50%). Willis et al., using the same experimental technique, with lower laser pulse intensity, reported exponential decay kinetics for a similar system [20]. This behavior was similar to that of dye sensitized TiO₂ in their system. They also investigated the effect of applied potential on recombination kinetics. Significant difference was found between ZnO and TiO₂: recombination half times decrease with more negative applied potentials for both nanostructured semiconductors, this trend started at a 400 mV more positive potential for ZnO. The difference was attributed mainly to a higher density of traps in ZnO.

Similarly very few studies deal with the electron transfer of electrons in dye sensitized ZnO to the oxidized part of the redox couple (i.e. triiodide). This reaction is studied in complete nanostructured solar cells using intensity-modulated photovoltage spectroscopy (IMVS). The electron lifetime in ZnO associated with this process decreases with increasing light intensity, as is the case for nanostructured TiO₂ solar cells.

Duffy et al [21]found that the back reaction between electrons and triiodide was second order in electron concentration for both ZnO and TiO₂ dye sensitized solar cells.

3.5. Kinetics

The dye-sensitized solar cell is based on photoelectrochemical reactions at the semiconductor-electrolyte interface, as already discussed, and the operation of the cell is therefore an outcome of competing opposite chemical reactions having different rate constants. A desired direction of the electrochemical reactions is achieved with fast wanted reactions (high rate constants) and slow unwanted reactions (low rate constants). The kinetics of the DSC is summarized in a highly simplified manner in Figure 3.4. The desired reaction, the electron injection from the excited state of the dye to the conduction band of TiO_2 , exceeds any unwanted reaction in an order of magnitude or more. In fact, occurring in the femtosecond time scale, the electron injection process between the N3 dye and TiO_2 in the DSC is one of the fastest chemical processes known [10]. The other desirable reaction is the regeneration of the dye by I^- , this is also a very fast reaction occurring in 10 ns in the normal conditions in the DSC. This is important for obtaining high cycle life for the dye, since lack of adequate conditions for the regeneration leads to dye degradation [10]. The electron percolation through the nanostructured TiO_2 has been estimated to occur in the millisecond to second range [13]

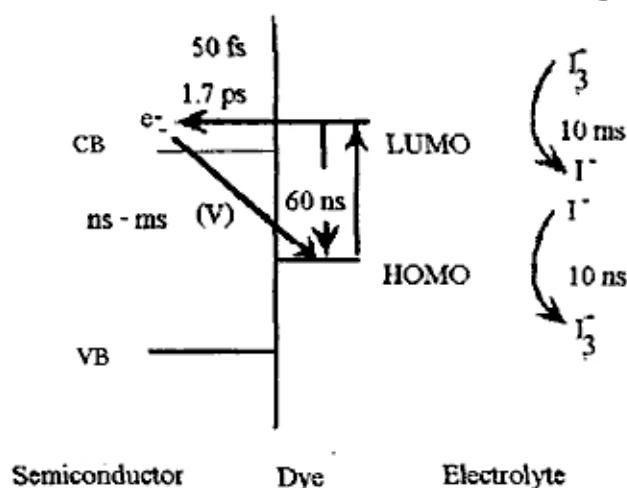
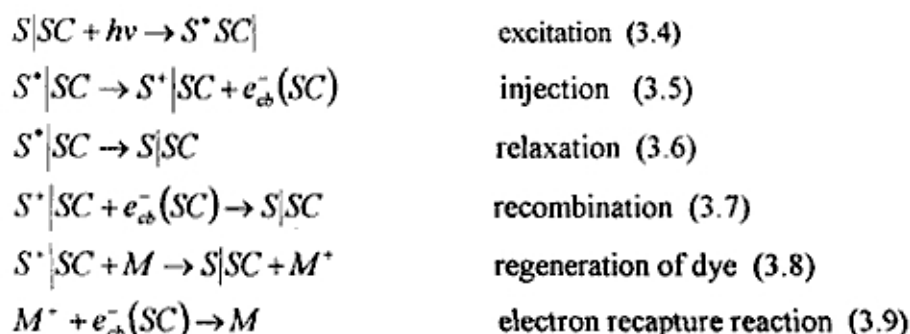


Figure 3.4. Kinetics in the DSSC, showing by arrows excitation of the dye from the HOMO to the LUMO level, relaxation of the excited state (60 ns), electron injection from the dye LUMO level to the TiO_2 conduction band (50 fs - 1.7 ps), recombination of the injected electron with the hole in the dye HOMO level (ns - ms), recombination of the electron in the TiO_2 conduction band with a hole (I_3^-) in the electrolyte (10 ms), and the regeneration of the oxidized dye by I^- (10 ns) [10]

3.5.1. Charge Transfer Dynamics

As explained before, at the base of the design of the DSSC is a photoanode constituted by a monolayer of a molecular redox dye-sensitizer (S) adsorbed onto a layer of nanocrystalline semiconductor (SC) oxide particles. Upon light absorption by adsorbed molecules (Eq. 3.4), excited states of the photosensitizer readily inject an electron into the conduction band of the solid (Eq. 3.5). Charge injection has been found for numerous efficient systems to occur in the femtosecond time frame, [22] thus successfully competing against deactivation of the dye excited state (Eq. 3.6). The electron back transfer from the conduction band to dye cations (Eq. 3.7) takes place much more slowly, typically in the microsecond-millisecond domain [23, 17]. In the presence of a redox mediator (M), this interfacial charge recombination competes kinetically with the reaction of the mediator with the oxidized sensitizer (Eq. 3.8). Charge

transport by the electrolyte in the pores of the semiconductor film to the counter electrode and that of injected electrons within the nanocrystalline film to the back-contact should be fast enough to compete efficiently with the electron recapture reaction (Eq. 3.9). These electron transfer processes are illustrated in Figure 3.5.



Orders of magnitude for the electron transfer rates in the classical DSC are summarized in Table 3.1

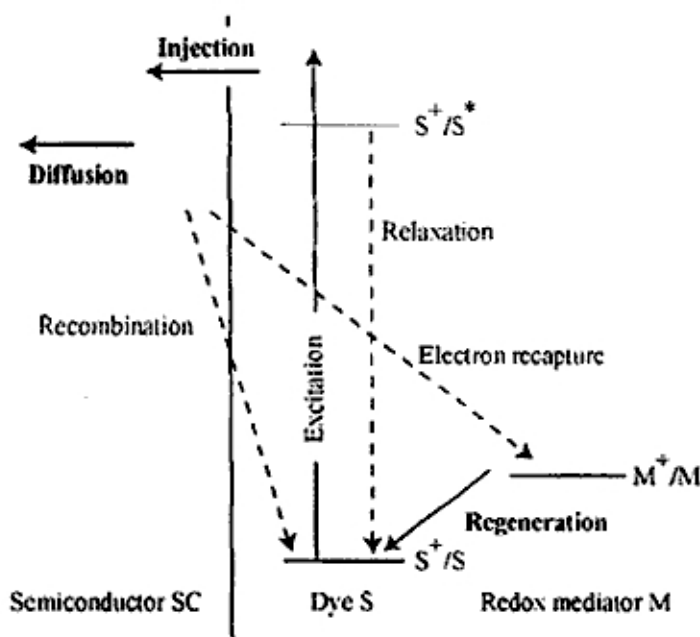


Figure 3.5. Electron transfer processes at the DSC heterojunction.

Table 3.1 Orders of magnitude for the different electron transfer processes rates taking place in a classical DSSC.

Process	Time frame
Excitation	Femtosecond
Injection	Femtosecond
Relaxation	Picosecond
Recombination	Micro-millisecond
Regeneration of dye	Nanosecond
Electron recapture reaction	Micro-millisecond

Bibliography

- [1] S. Södergren, A. Hagfeldt, J. Olsson, S.E. Lindquist, *J.Phys.Chem-Us*, 98., (1994), 5552.
- [2] F. Cao, G. Oskam, G.J. Meyer, P.C. Searson, *J. Phys. Chem. B*, 100, (1996), 17021.
- [3] K. Schwarzburg, F. Willig, *J. Phys. Chem. B*, 103, (1999), 5743.
- [4] D. Cahen, G. Hodes, M. Graetzel, J.F. Guillemoles and I. Riess *J. Phys. Chem., B*, 104, (2000), 2053-2059
- [5] Soga, T., Nanostructured materials for solar energy conversion, Elsevier, Amsterdam, (2006)
- [6] K. Westermark, H.Rensmo, H.Siegbahn, K.Keis, A.Hagfeldt, L.Ojamae and P.Persson, *J.Phys.Chem.B*,106(2002) 10102-10107
- [7] M. K. Nazeeruddin, A. Kay, I. Rodicio, R. Humphry-Baker, E. Müller, P. Liska, N.Vlachopoulos, M. Grätzel, *J. Am. Chem. Soc.*, 115, (1993), 6382.
- [8] C.J. Barbé, F. Arendse, P. Comte, M. Jirousek, F. Lenzmann, V. Shklover, M. Grätzel, *J. Am. Ceram. Soc*, 80, (1997), 3157.
- [9] B. O'Regan, M. Grätzel, *Nature*, 353, (1991), 737.
- [10] A. Hagfeldt, M. Grätzel, *Acc.Chem. Res.*,33, (2000), 269-277
- [11] J.B. Asbury, Y. Wang, and T.Q. Lian, *J.Phys.Chem.B*, 103 (1999), 6643-6647
- [12] N.A. Anderson, X. Ai. and T.Q. Lian, *J.Phys.Chem.B*,107 (2003), 14414-14421
- [13] A. Hagfeldt, M. Grätzel, *Chem. Rew.*,95 (1995) 49.
- [14] A.Solbrandt, K.Keis, S.Södergren, H.Lindström,S-E Lindquist and A.Hagfeldt, *Sol.Energy Mater.Sol.Cells*,60(2000),181-193
- [15] T.Oekermann, T.Yoshida, C.Boeckler, J.Caro and H.Minoura, *J.Phys.Chem. B*,109 (2005) 12560-12566
- [16] A. Zaban, A Meier and B. A. Gregg *J. Phys. Chem. B*. 101(1997), 7985-7990.
- [17] S.A. Haque, Y.Tachibana, D.R. Klug, J.R. Durrant, *J. Phys. Chem. B*, 102 (1998), 1745-1749.
- [18] S. Y. Huang, G. Schlichthörl, A. J. Nozik, M. Grätzel, and A. J. Frank. *Phys. Chem. B*, 101 (1997), 2576 -2582
- [19] C.Bauer, G.Boschloo, E.Mukhtar and A.Hagfeldt, *J.Phys.Chem. B*,105 (2001) 5588-5588
- [20] R.L.Willis, C.Olson, B.O'Reagan, T.Lutz, J.Nelson and J.R.Durrant, *J.Phys.Chem.B*, 106(2002),7605-7613
- [21] N.W.Duffy,L.M.Peter, R.M.G. Rajapakse and K.G.U.Wijayantha *Electrochem.Comm.*, 2 (2000) 658-662
- [22] Grätzel, M.; Moser, J. E. Solar Energy Conversion. In *Electron Transfer in Chemistry*, Balzani, V., Ed.; Wiley-VCH: Weinheim, 5(2001), 589.
- [23] Desilvestro, J.; Gratzel, M.; Kavan, L.; Moser, J.; Augustynski, J. *J Am Chem Soc*, 107, (1985), 2988.

Chapter 4 Experimental techniques and device preparation

In this Chapter an engineering point of view is taken to the preparation of the DSCs. Materials used in the literature in the different cell components are reviewed and the key material properties required for the cell components as well as some essential preparation methods are discussed.

Last part is a brief description of the different characterization methods used in this these.

4.1. Materials and synthesis

The initial part of this chapter is dedicated to the description of each component used for the preparation of the dye-sensitized solar cells studied in this work. Glass supports, sensitizers, electrolytes and counter electrodes are described, as well as their assembly to form the whole device. The second part of this chapter explains the experimental methods used to analyze the systems under investigation. These experimental methods include photoelectrochemical, analytical and electrochemical characterizations as well as Intensity modulated photocurrent spectroscopy (IMPS) and intensity modulated photovoltage spectroscopy (IMVS) measurements.

4.1.1. TCO coated glass

The electrodes of the standard DSC are prepared onto transparent conducting oxide (TCO) coated glass substrates, between where the cell is assembled. The conducting coating of the substrate works as a current collector and the substrate material itself both as a support structure to the cell and as a sealing layer between the cell and the ambient air.

Fluorine-doped tin oxide ($\text{SnO}_2:\text{F}$) and indium tin oxide ($\text{In}_2\text{O}_3:\text{Sn}$ or ITO) are the most frequently used TCOs in thin film photovoltaic cells. As the only TCO coating stable at these temperatures [1], the $\text{SnO}_2:\text{F}$ has been the material of choice for DSCs. The choice of sheet resistance of the SnO_2 -coated glass is a solution between conflicting beneficial properties of the TCO-coated glass: the higher conductance and the lower transmittance and vice versa.

The $\text{SnO}_2:\text{F}$ -coated glass can be purchased from several commercial manufactures such as Libbey Owens Ford, Asahi, Pilkington (TEC15) and Nippon Sheet Glass(NSG) to only mention a few.

An alternative to the glass substrates is TCO coated plastic foils, which has been introduced and studied especially for the commercialization of the dye solar cell in mind. Table 4.1 resumes the characteristics of two substrates.

Table 4.1 TCO substrates used for the preparation of DSC. T_{550} : transmission at 550 nm. These values are provided by the producers of the respective TCO substrates.

TCO name	Resistivity [Ω /sq]	T_{550} [%]	Diffusion [%]	IR reflectance at 10 nm [%]	Glass thickness [mm]
NSG	12	82	-	-	1
TEC15	15	83	<0.7	86	2.3

4.1.2. Nanoparticle electrodes

The nanostructured electrodes are deposited from a solution or a paste containing semiconductor nanoparticles of desired size. Control of the properties of the nanoparticle solutions and the nanoparticle films obtained from these solutions belongs to the fields of colloid and sol-gel chemistry, which have been the essential enabling technologies for the development of high efficiency DSCs.

Some important topics of preparing nanostructured electrodes for the DSSCs will be explained next.

4.1.2.1. ZnO particle synthesis

Nanoparticles: Colloidal ZnO was prepared using a simplification of previously published methods [2]. 11 g (50 mmol) zinc acetate dihydrate (Merck) was stirred in 100 ml absolute ethanol (99.5%, Kemetyl) at room temperature to give an opaque suspension. 21 ml (50 mmol) of a 25% solution of tetramethylammonium hydroxide (TMAOH) in methanol (Aldrich) was added. The suspension was heated and refluxed (80 °C) for 30 min. During heating

the solution turned completely clear, but during reflux it became slowly white again due to aggregation of the colloids. The suspension was left to cool down and settle overnight, decanted and washed with ethanol. This procedure was used to lower the concentration of TMAacetate, essential for the preparation of good quality films. Next, the ZnO colloid was concentrated until visibly viscous.

Nanorods: Nanorods and nanoparticles were synthesized in similar way. Zinc acetate in ethanolic solution reacts with tetramethylammonium hydroxide (25% in methanol) at ambient temperature. Suspension is refluxed in rotavapor for nanorods by two hours and half of hour for nanodots in flask.

ZnO doped Mg^{2+} : Two kind of films were prepared

- Thin film deposition was using the sol-gel technique, in similar way to one mentioned before. In brief, a sol of zinc acetate dihydrate $ZnCH_3COO_2 \cdot 2H_2O$ and magnesium chloride hexahydrate $MgCl_2 \cdot 6H_2O$ was prepared after mixing thoroughly the above salts in ethanol and tetramethylammonium hidroxide solution (25% in methanol) on a magnetic stirrer until it becomes transparent.

Total concentration of metal ions was 0.1M. The concentration of Mg^{2+} was so adjusted as to form $Mg_xZn_{1-x}O$ thin films with various values for x in the range of $0.0 < x < 0.20$.

- b) ZnO nanoparticle films after sintering were coated with acetate magnesium solution in ethanol by dipping following by sintering at 400° C.

ZnO doped Li+ The precursor solution was prepared by stirring 50 mmol of zinc acetate dihydrate (Merck) in absolute ethanol (99.5% Kemetyl) at room temperature, obtaining an opaque suspension. 50 mmol of a 25% tetramethylammonium hydroxide (TMA-OH) in methanol (Aldrich) and different quantities of solid $Li(NO_3) \cdot 3H_2O$ (depending on Li/ZnO wanted) is added to the suspension. The suspension is then heated and reflux at 80°C for 30 minutes and then left to cool down and settle overnight. Finally, it was decanted and washed with ethanol.

The films were obtained for doctor blading method onto substrate conductor ($SnO_2:F$) and fired at 380° C for 30 minutes. The film thickness was 3 μm .

4.1.2.2. TiO₂ particle synthesis

Transparent nanostructured TiO₂ electrodes were prepared from HNO₃-stabilized TiO₂ colloids autoclaved for 15 h at 200 °C. Electrodes were heated at 450 °C for 30 min. Film thickness (3-4 μm) was determined by profilometry. The flow diagram given in Figure 1 summarizes the reaction steps involved in the sol-gel preparation of the films. The final properties of the nanostructured TiO₂ electrode are highly dependent on the properties of the colloidal [3] solution used for the film deposition.

The influence of the processing parameters of the TiO₂ paste preparation to the obtained TiO₂ film porosity, pore-size distribution, light scattering, and electron percolation in the film and thus to the solar cell efficiency has been investigated in more detail by Barbé et al. [4].

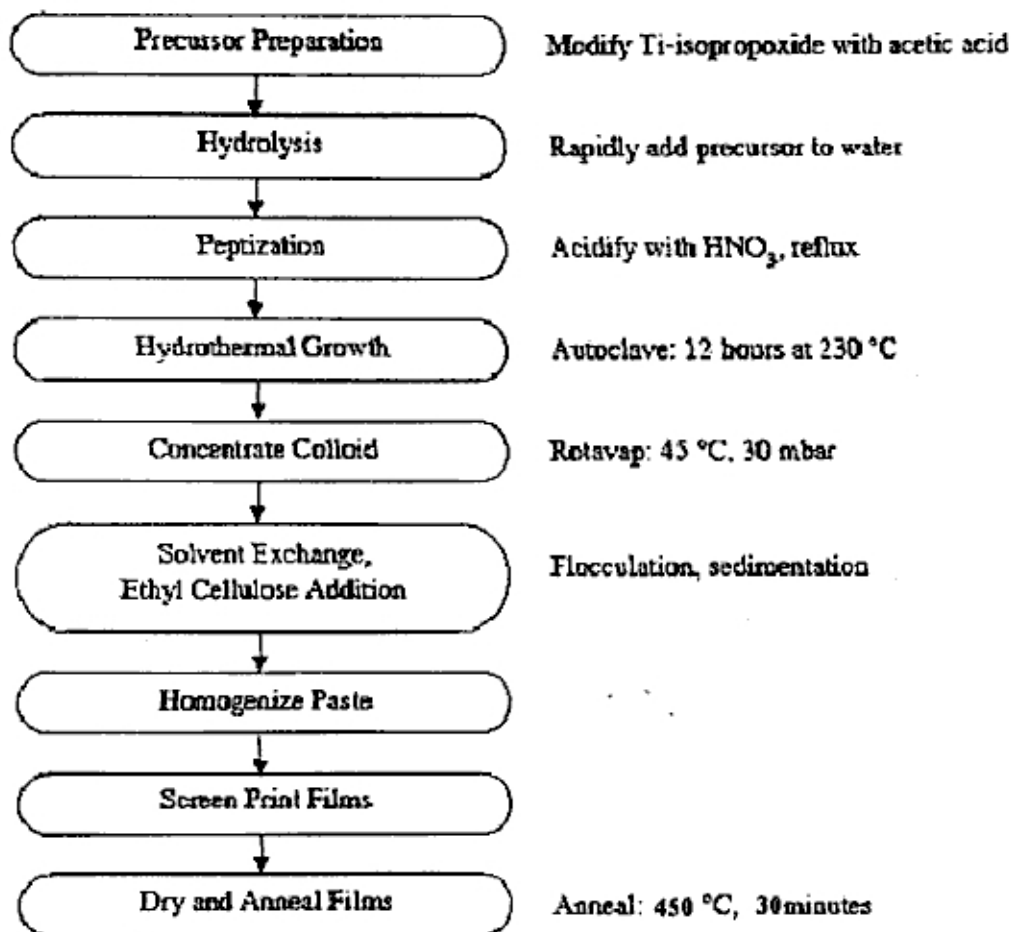


Figure 4.1. Flow diagram for the preparation of the TiO₂ colloids and mesoporous films.

4.2. Device assembly

4.2.1. Photoelectrodes

The dye molecules are adhered onto the nanostructured TiO₂ electrode by immersing the sintered electrode into a dye solution, typically $5 \cdot 10^{-4}$ M in ethanol [5], for a long enough period to fully impregnate the electrode, about 12 hours in the dark. During the impregnation process the electrode is sensitive to water [6]. To minimize water vapor content inside the pores of the electrode, the electrode should be warm upon immersion to the dye solution.

The concentration of the dye bath and the adsorption time strongly influence the efficiency of dye-sensitized ZnO solar cells[7]. In this thesis two sensitization methods were used:

Rapid method: In rapid method [8] a 8 μ L volume of a 20 mM N719 solution in dimethyl sulfoxide (DMSO) was pipetted onto the surface of ZnO or TiO₂ electrode (at 50 °C) and left for 1min (N719 corresponds to (TBA)₂ *cis*-Ru(Hdcbpy)₂(NCS)₂).

Slow method: The polyene-diphenylaniline dye D5 was used in slow method electrodes were immersed in 0.5 mM D5 ethanolic solution, overnight. Then electrodes were rinsed with ethanol, dried and assembled with a platinized conducting glass counter electrode using a 50 μ m thick thermoplastic frame (Surlyn 1702).

4.2.2. Counterelectrodes

A catalyst coating is needed for fast reaction kinetics on the triiodide reduction reaction at the TCO coated cathode.

Nanosized platinum metal clusters were deposited onto clean TCO substrate using a catalyst precursor solution composed of 5 mM solution of hexachloroplatinic(IV) acid hexahydrate in anhydrous isopropanol. The precursor solution was spread ($10 \mu\text{L} \cdot \text{cm}^{-2}$) and dried in air for 1 min. Coated electrodes were placed on a temperature controlled hot gun, where temperature was gradually increased and left to stabilize, in order to achieve the electrode surface temperature of 380°C . The electrode was allowed to cure at the temperature for 15 min. This technology produces optically transparent electrodes.[9]

4.2.3. Electrolytes

The electrolyte used in the DSCs consists of iodine (I_2) and triiodide (I_3^-) as a redox couple in a solvent with other substances added to improve the properties of the electrolyte and the performance of the operating DSC.

Since the discovery of the DSC about ten years ago [10] no redox couple preceding the performance of the I/I_3^- couple in the DSC. The I/I_3^- redox electrolyte is prepared by adding I_2 to the solvent together with iodine salt such as LiI or TBAI (tetrabutylammonium iodine).

The electrolyte composition was as follows: 0.5 M LiI ; 0.05 M I_2 in 3-methoxypropionitrile with either 0.1 M 1-methylbenzimidazole (electrolyte 1) or 0.5 M 4-*tert*-butylpyridine (electrolyte 2) as an additive.

In ZnO solar cells sensitized with D5, electrolyte composition was 0.05 M I_2 , 0.6 mM TBAI, 0.5 M 4-*tert*-butylpyridine and different concentrations of LiClO_4 .

4.2.4. Cell assembly

The two glass electrodes were sealed together by putting a cleaned thin (60 μm Surlyn plastic) rectangular piece of plastic in between and heated it for 2 minutes. The plastic has a hole for the film and enough surrounding area to insulate the two electrodes from each other. The two glass pieces were put on a hot plate (120°) and heated under pressure for two minutes.

To finish the preparation the cell was filled with electrolyte and sealed. The electrolyte is easily injected with a pipette into one of the holes and it distributes itself over the film by capillary forces.

After filling, the surface of the top glass is dried with a piece of tissue. A cover glass is placed on top of the two holes, with a piece of surlyn plastic, and heated with pressure at 250°C for 5-10 sec.

To enhance the conductivity silver paint was put on the electrode contacts.

4.3. Photoelectrochemical characterization

The standard characterization techniques of DSC include the determination of the current-voltage characteristics under light irradiance of different intensities and the determination of the photocurrent under low intensity monochromatic light.

Current-voltage characteristics of a solar cell may be approximated by the following mathematical expression:

$$I = I_{ph} - I_s \left(e^{V_a/V_t} - 1 \right) - \frac{V_a}{R_{sh}} \quad (4.1)$$

where I is the current, I_s the saturation current of the diode, and I_{ph} the photocurrent, which is assumed to be independent of the applied voltage V_a . This applied voltage includes the series resistance R_s :

$$V_a = V + R_s I \quad (4.2)$$

V_t is the thermal voltage and is equal to

$$V_t = \frac{n k T}{e}, \quad (4.3)$$

with n as the ideality factor and e the elementary charge. Eq. 4.1 models the dark current in a one-diode system and therefore is only a simplified representation of the DSC. Its equivalent circuit is shown in Figure 4.2. The real structure of the device is more complicated and corresponds to a multi-diode model that takes into account the different charge transport processes within the cell.

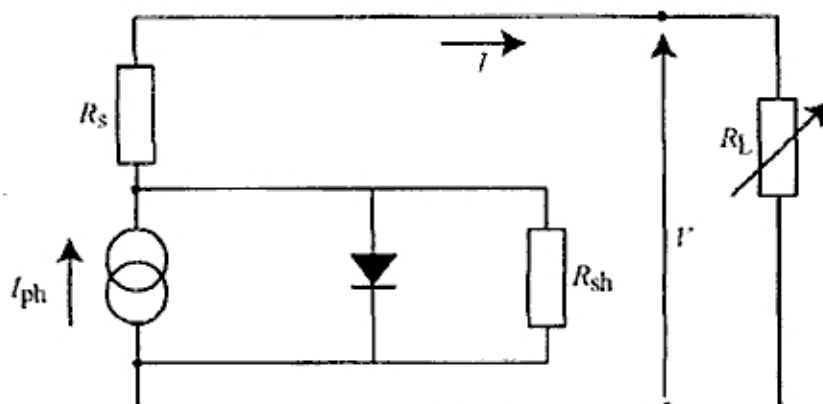


Figure 4.2 The DSC under light irradiation can be represented as a mix non-perfect current generator (which has a shunt resistance R_{sh} and a parasite series resistance R_s) mounted in parallel to a non-perfect diode.

The incident light power on the DSC surface, or irradiance, is expressed in Wm^{-2} . $1000 Wm^{-2}$ is equivalent to the light power of a full sun (100% Sun) for an air-mass number of 1.5 (AM 1.5). Photoelectrochemical data were measured using a 450 W xenon light source that was focused to give $1000 Wm^{-2}$, the equivalent of one sun at AM 1.5, at the surface of the test cell. Series of I-V measurements were performed in air and at room temperature and the dye-sensitized ZnO electrodes were illuminated through the working electrode substrate. The I-V curves were monitored and recorded using a computerized Keithley Model 2400 source measure unit. The light source (Light Drive 1000, type 1400-E2/1, Fusion Lighting, Inc.) was calibrated pyranometer model CM11 Kipp & Zonen Delft/Holland.

4.3.1. Incident photon-to-current conversion efficiency (IPCE)

The incident photon-to-current conversion efficiency (*IPCE*) is defined as the number of electrons generated by light in the external circuit divided by the number of incident photons. The *IPCE*(λ) curve as defined below:

$$IPCE(\lambda) = \frac{1240 \cdot J_{sc}}{\lambda \phi} \quad (4.4)$$

where λ is the wavelength, J_{sc} is the current at short circuit (mAcm^{-2}), and ϕ is the incident radiative flux (W m^{-2}). This curve can be derived from the measured absorption spectrum of the adsorbed photosensitizer for comparison.

The *IPCE* can be expressed in terms of the light harvesting efficiency (*LHE*), the quantum yield of charge injection (Φ_i) and the efficiency of collecting the injected charge at the back contact (η_c)

$$IPCE(\lambda) = LHE(\lambda) \cdot \Phi_i \cdot \eta_c \quad (4.5)$$

The light harvesting efficiency is given by

$$LHE(\lambda) = 1 - 10^{-\Gamma \sigma(\lambda)} \quad (4.6)$$

where Γ is the number of moles of sensitizer per square centimeter of projected surface area of the film and σ the absorption cross section. The quantum yield of charge injection is given by

$$\Phi_i = k_i / (\sum k_d + k_i) \quad (4.7)$$

where k_i is the rate constant for electron injection and $\sum k_d$ is the sum of all rate constants for the relaxation processes.

The incident photon-to current efficiency (*IPCE*) was monitored by using a computerized setup composed of a Xe arc lamp (300 W Cemax, ILC Technology), a 1/8 m monochromator (CVI Digikröm CM 110), a Keithley 2400 source/meter, and a Newport 1830-C power meter with 818-UV detector head.

Open circuit potential (V_{oc})

The open circuit potential (V_{oc}) is the cell potential measured when current within the cell is equal to zero. The equation for the current-voltage characteristics (Eq. 4.1) can then be written and simplified as

$$I_{ph} = I + I_s (e^{V/V_i} - 1) \quad (4.8)$$

V_{oc} is obtained from Eq.4.1. by setting $I=0$. At this condition, $V_a=V_{oc}$

$$I_{ph} = I_s (e^{V_{oc}/V_i} - 1) \quad (4.9)$$

$$V_{oc} = V_t \cdot \ln \left(\frac{I_{ph}}{I_s} + 1 \right) \cong V_t \cdot \ln \left(\frac{I_{ph}}{I_s} \right) \quad (4.10)$$

V_{oc} is then a function of the irradiance.

Short circuit current density (J_{sc})

The short circuit current (I_{sc}) is the cell photocurrent measured at zero voltage, where the series resistance is minimal. Therefore $V_a=0$ and $I_{sc} = I_{ph}$

The short circuit current density (J_{sc}) is the short circuit current divided by the photoactive surface area of the cell. J_{sc} is also a function of the irradiance.

Fill factor (FF)

The fill factor (FF) measures the cell's quality as a power source and therefore is the ratio of the maximum power to the external short circuit current and open circuit voltage:

$$FF = \frac{I_m V_m}{I_{sc} V_{oc}}$$

This parameter indicates the deflection of the current-voltage characteristic from a square likecurve (Figure 4.3) and is therefore dependent on:

- the shunt resistance R_{sh}
- the series resistance R_s
- the ideality factor n

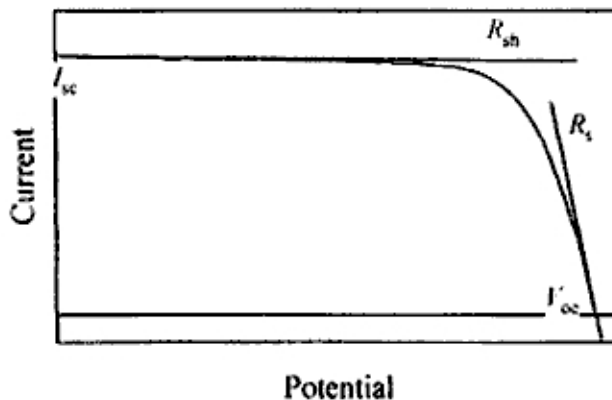


Figure 4.3 Example of I/V curve showing the open circuit potential point (V_{oc}) and the short circuit current point (I_{sc}). The series resistance R_s is given by the slope of the tangent line at V_{oc} and the shunt resistance R_{sh} is given by the slope of the tangent line at I_{sc} .

The resistance at I_{sc} is extremely high. In an equivalent circuit model of a solar cell, it represents a shunt resistance. The resistance at V_{oc} is on contrary very low. In the equivalent circuit model, it represents a series resistance. Both of these resistances are internal, and represent energy dissipation mechanisms in the cell. Ideally, one would like zero series resistance and infinite shunt resistance, to maximize the fill factor up to unity. The series resistance depends on the material resistivity, on the contact resistance of the electrodes and on the collecting grid resistance if present. The ideality factor is a number

which characterizes the slope of a current-voltage plot as measured on a semi-logarithmic scale.

Efficiency (η)

The efficiency describes the performance of the solar cell and is defined as the ratio of the maximum electric power (P_m) extracted to the incident radiation power (P_{in}) on the solar cell surface:

$$\eta = \frac{P_m}{P_{in}} = \frac{I_{sc} \cdot V_{oc} \cdot FF}{P_{in}}$$

As the efficiency is a function of I_{sc} , V_{oc} and FF , improvement of the photovoltaic yield is achieved by optimization of these three parameters.

4.3.2. Voltage Charge

The trap distribution is one of the most important features of the DSC, because the concentration of electrons occupied in traps, e_{-TRAP} , is directly connected to the concentration of conduction band electrons, e_{-CB} . Normally, most electrons in the mesoporous film are localized in traps, so the trap distribution function can be estimated by measuring the total charge accumulated in the TiO_2 [11].

Experimentally, the cell is illuminated at OC until V_{oc} is constant. Then, the cell is switched to short-circuit and the illumination is simultaneously turned off. The output current is integrated and eventually reaches Q_{oc} . An alternate method, especially efficient to obtain low voltages, is to allow the voltage to decrease due to recombination in the dark before the cell is short-circuited and the current integrated [12].

To achieve the correct relationship between V_{oc} and Q_{oc} , both methods require that the time for charge extraction is long enough to extract all electrons in the film. For the alternate method, it is also important that the electron reorganization time within the mesoporous film is short; otherwise, the displayed V_{oc} value does not resemble the quasi Fermi level, nE_F , in the mesoporous film.

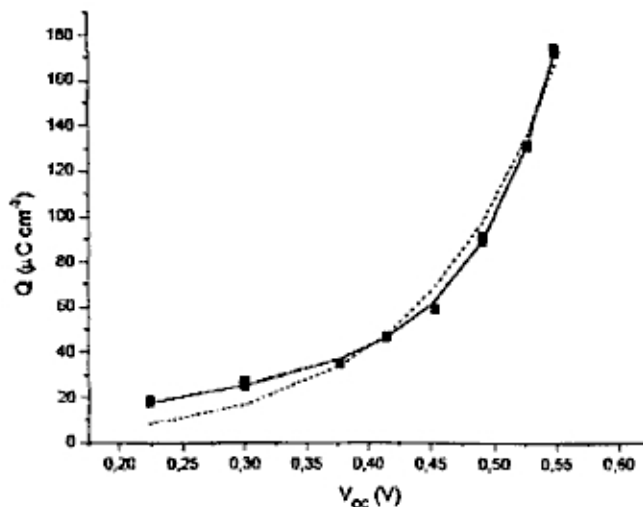


Figure 4.4 Measured Q_{oc} - V_{oc} data (squares) fitted with a single exponential function (dashed line) and an exponential function containing an additional linear term (straight line).

The trap distribution is usually described as a tail of states below the conduction band and usually, the charge accumulated in the traps is expressed by an exponential function [11]. To account for the charge accumulated at the TCO/electrolyte interface at the back contact, a linear term, $V_{oc}C_{sc}$, is also included in the overall $V_{oc}Q_{oc}$ relationship; see Eq. 4.11.

$$Q_{oc} = Q_{oc}(0) \exp(\beta q V_{oc} / k_B T) + V_{oc} C_{sc} \quad (4.11)$$

In Eq. 4.11, $Q_{oc}(0)$ is the charge at zero voltage, β is related to the width of the trap distribution, and C_{sc} is the capacitance of the space charge region associated with the TCO. Measurements made using electric impedance spectroscopy have indicated that C_{sc} is of the order of $10^{-5} \text{ F cm}^{-2}$ [13] and by comparison between fitted values of $Q_{oc}(0)$ and β , it has been concluded that most of the electrons are localized in traps, *i.e.*, originate from the exponential term in Eq. 4.11, under normal working conditions ($V > 0.5 \text{ V}$). Electron concentrations in the DSC were measured in a PC-controlled setup using a red-light-emitting-diode (Luxeon Star 1W, $\lambda_{max} = 640 \text{ nm}$). The photocurrent and photovoltage were measured using a 16-bit resolution data acquisition board (National Instruments) in combination with a current amplifier (Stanford Research Systems SR570).

4.4. Analytical characterization

4.4.1. Absorption spectroscopy

UV/vis spectrophotometer measures the intensity of light passing through a sample (I), and compares it to the intensity of light before it passes through the sample (I_0). The ratio I / I_0 is called the transmittance, and is usually expressed as a percentage (%T). The absorbance, A , is based on the transmittance:

$$A = -\log(\%T)$$

The basic parts of a spectrophotometer are a light source (often an incandescent bulb for the visible wavelengths, or a deuterium arc lamp in the ultraviolet), a holder for the sample, a diffraction grating or monochromator to separate the different wavelengths of light, and a detector. The detector is typically a photodiode or a charge coupled device (CCD). Photodiodes are used with monochromators, which filter the light so that only light of a single wavelength reaches the detector. Diffraction gratings are used with CCDs, which collect light of different wavelengths on different pixels. A spectrophotometer can be either single beam or double beam. In a single beam instrument, all of the light passes through the sample cell. I_0 must be measured by removing the sample. This was the earliest design, but is still in common use in both teaching and industrial labs.

In a double-beam instrument, the light is split into two beams before it reaches the sample. One beam is used as the reference; the other beam passes through the sample. Some double-beam instruments have two detectors (photodiodes), and the sample and reference beam are measured at the same time. In other instruments, the two beams pass

through a beam chopper, which blocks one beam at a time. The detector alternates between measuring the sample beam and the reference beam.

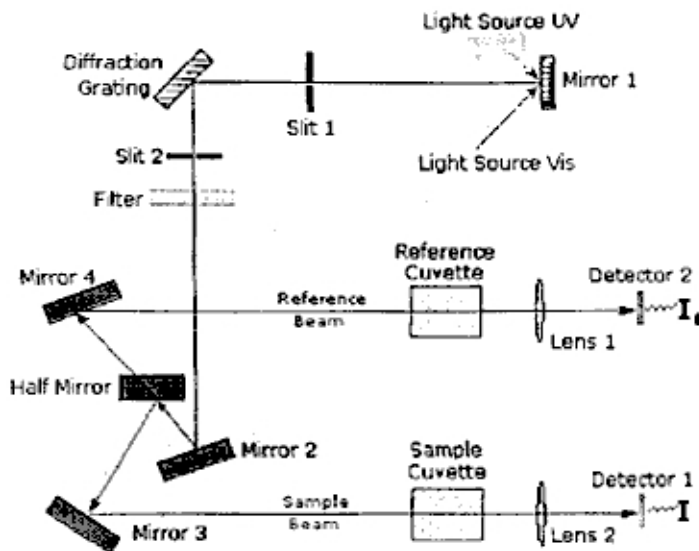


Figure 4.5 Schematic diagram of UV-Vis spectrometer

UV-vis spectra were recorded using a Hewlett-Packard 8453 diode array spectrometer in this work.

4.4.2. SEM

In scanning electron microscopy high-energy electrons are focused into a fine beam, which is scanned across the surface of the specimen. After many interactions of the beam electrons with the atoms of the specimen it is possible to obtain as a result an image of the sample surface that is straightforward to interpret.

The principle of the SEM is shown. Electrons from a thermionic or field-emission cathode are accelerated by a voltage of 1-50 kV between cathode and anode. Then the beam is condensed and collimated by pole-pieces (magnetic lens) until it dissipates its energy in the sample. The emitted electrons consist of secondary electrons (SE), backscattering electrons (BSE) and Auger electrons. The SE and BSE carry information about the sample topography.

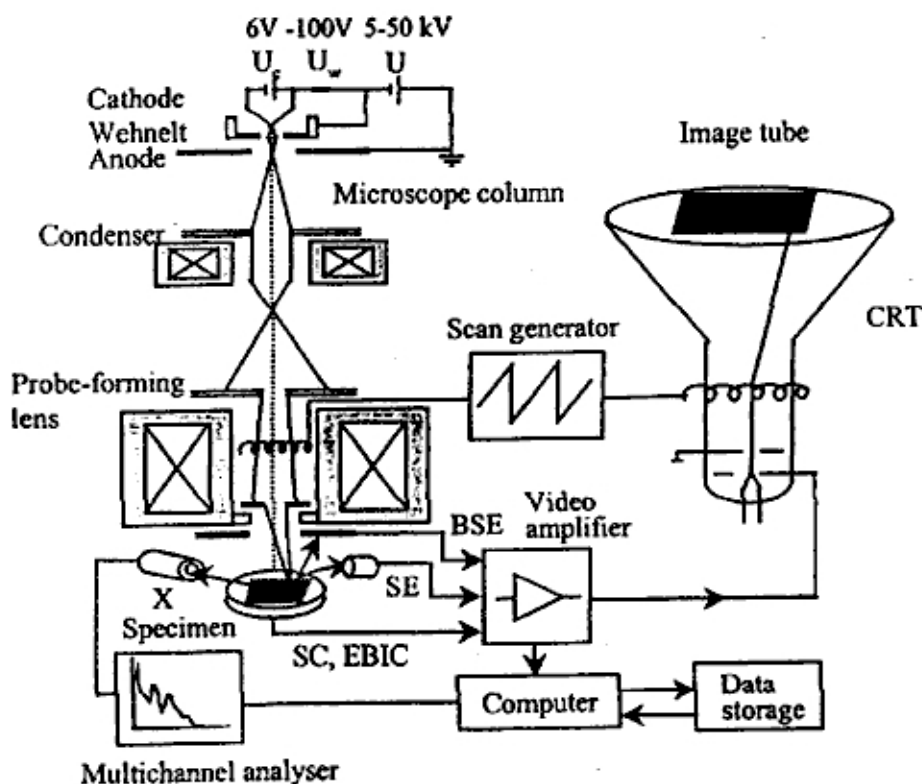


Figure 4.6. Principles of the scanning electron microscope (BSE=backscattered electrons, SE=secondary electrons, SC=specimen current, EBIC=electron-beam-induced current, X=X-ray, CRT=cathode-ray tube[14])

One important advantage of SEM is the wide variety of electron-specimen interaction that can be used to form an image and to furnish qualitative and quantitative information. Scanning electron microscopy studies in the present work were carried out using a LEO 1530 Gemini microscope.

4.4.3. TEM

Transmission electron microscopy constitutes one of the most efficient tools for structural characterization of materials due to the possibility to gain high magnification of the analyzed images. In TEM an electron beam is thermionically emitted from a gun and accelerated to 100 keV or more (1 MeV for high-resolution transmission electron microscopies), is focused onto a sample by using magnetic lenses (condenser lenses) and, finally, passes through the specimen due to the applied high voltage. The scattering processes experienced by the electrons during their passage through the sample determine the obtained information. Elastic collisions of the electrons from the beam with the potential field of the ion cores, produces a diffraction pattern. Inelastic collisions between the electron beam and matrix electrons at heterogeneities, give complex absorption and scattering effects, producing spatial variations in the intensity of the transmitted beam.

The emerged primary and diffracted electron beams are made to pass through an array of magnetic lenses that, like in optical microscopes, are denoted objective lenses for

the production of the first image which is then magnified by the projector lenses to produce the second image.

There are two basic modes of TEM operation depending on how the beam reaches the back focal plane of the objective lens [15]: diffraction and image mode.

The high magnification of the TEM instruments is a result of the effective wavelength of the electrons that can be obtained from Broglie's equation.

$$\lambda = \frac{h}{\sqrt{2mqV}}$$

Where m and q are the electron mass and charge, h is the Planck's constant, and V is the electric potential used for the acceleration of the electrons. So for 100-keV electrons, $\lambda \sim 0.004 \text{ \AA}$, which is much smaller than the diameter of an atom.

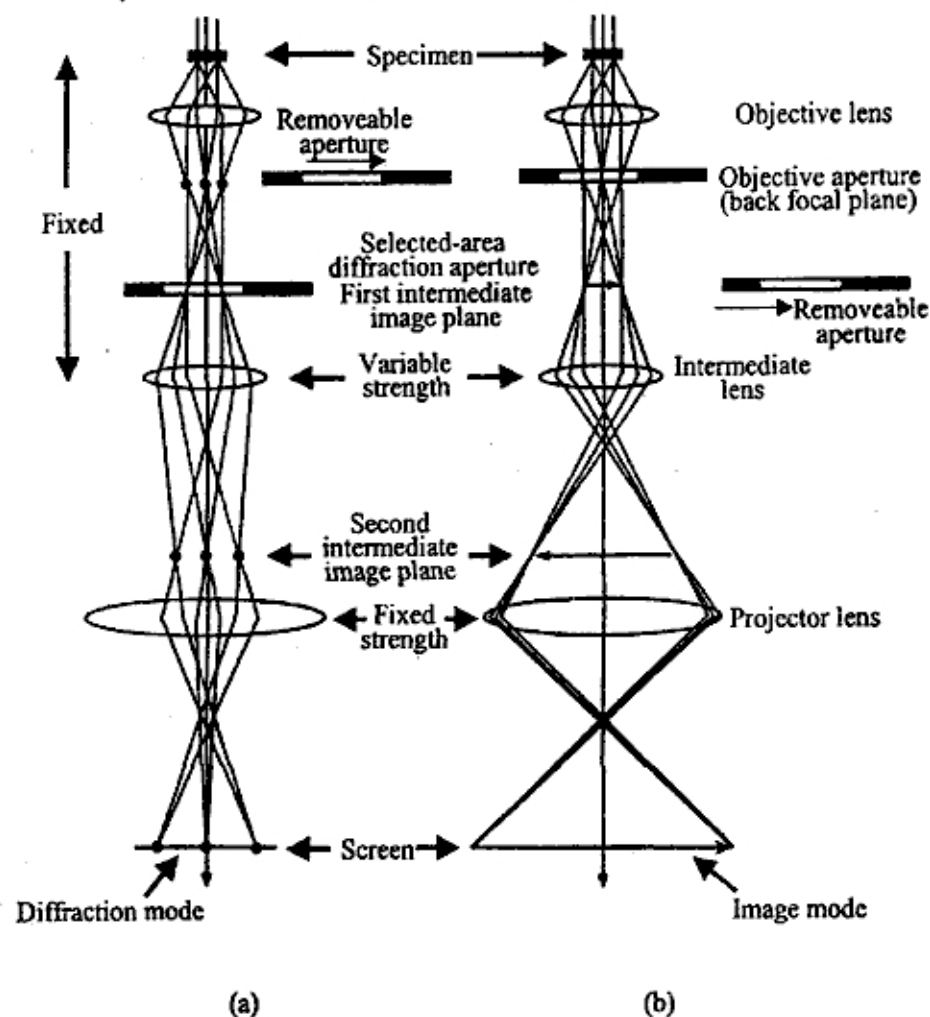


Figure 4.7 Schematic representation of the two basic operation modes in TEM: (a) projects the diffraction pattern on the viewing screen and (b) projects the image onto the screen. [16]

4.4.4. X ray diffraction

X-ray diffraction is a powerful technique that is used to analyze crystalline materials. Each atom exposed to a beam of X-ray is the source of a coherent scattered wave which will interfere in a constructive or destructive way with waves emitted from neighboring

atoms. The method implies a study of a spatial distribution of the total diffracted wave. Thus under ideal conditions, a perfect crystal and an incident beam composed of perfectly parallel and strictly monochromatic radiation will give a sharp peak in the intensity of the scattered radiation. The path difference between two rays, which interfered constructively, is just $2d\sin\theta$, where θ is the angle of incidence and d is the interplanar distance. This leads to the Bragg formulation.

$$2d\sin\theta = n\lambda,$$

Where λ is the wavelength of the X-ray and n is the order of the reflection.

Ideal conditions never actually exist, so we must determine the effect on diffraction of various kinds of departure from the ideal. We find that a very small crystal (less than about $0.1\ \mu\text{m}$) cause broadening (a small angular divergence) of the diffracted beam. A good treatment of the problem gives.

$$g = \frac{0.9\lambda}{B\cos\theta}$$

which is the Scherrer formula and it is used to estimated the particle size of a very small crystal g , by measuring the broadening of the diffraction line B , at half its maximum intensity in radians. When studying thin films, it is recommended to use grazing-incidence X-ray diffraction, which is a method that makes it possible to obtain more information about the film by using a very low incident angle to the sample surface (0.1° - 5°). Figure 4.6 displays the geometry of this system implemented with a Göbel mirror as a monochromator and a parallel plate for a collimator.

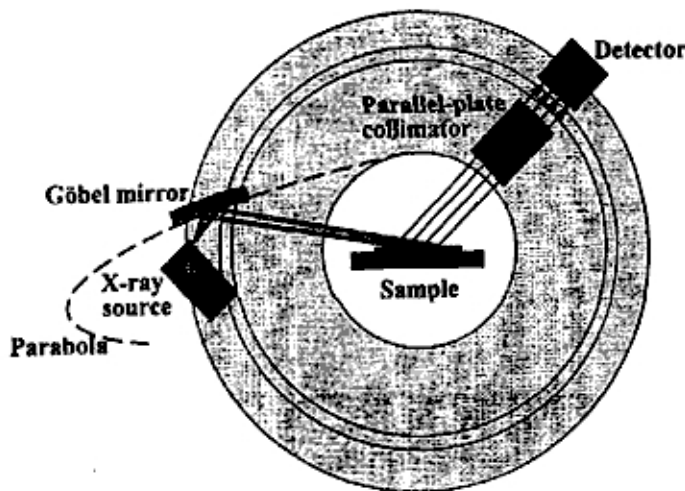


Figure 4.8. Schematic representation of the grazing-incidence X-ray diffraction geometry with a Göbel mirror and a parallel collimator.

In this work XRD was carried out by a Siemens D5000 diffractometer with a CuK α anode, using either a grazing-incidence unit suitable for thin films or a conventional $\theta - 2\theta$ set up.

4.4.5. ATR

The attenuated total reflection (ATR) method, also called multiple internal reflectance (MIR) method, is a versatile and powerful technique for infrared absorption spectrophotometry. This method is popular not only in FTIR but also in conventional dispersive IR. This is because it is not necessary to chemically treat, or machine, the samples. Measurements it made without destroying the samples.

The sample is held in contact with a prism made of highly refractive material which transmits infrared rays; infrared rays are incident on the sample at an angle larger than the critical angle (angle that induces total reflection). The light that is totally reflected by the interface between the sample and the prism is measured to obtain an infrared spectrum.

Though it is called "total reflection", the light travels through the thin surface layer of the sample, and therefore, the spectrum obtained is similar to that obtained from a very thin slice of the same sample.

Infrared light can penetrate to a depth expressed by the next equation:

$$dp = \frac{\lambda}{2\pi(\sin^2 \theta - n_{21}^2)^{\frac{1}{2}}}$$

where, θ : Incident angle

n_{21} : (Refractive index of sample) / (Refractive index of prism)

λ : Wavelength

When $\theta = 45^\circ$ and $n_{21} = 0.5$, therefore, $10\mu\text{m}$ (1000 cm^{-1}) dp corresponds to $3.18\mu\text{m}$ and $5\mu\text{m}$ dp (2000 cm^{-1}) to $1.6\mu\text{m}$,

4.5. Intensity-modulated photocurrent and photovoltage spectroscopy (IMPS, IMVS)

The diffusion of electrons to the substrate contact gives rise to a time delay between electron injection and collection. This delay is manifest as a phase lag in the photocurrent response to intensity-modulated light [17]. Intensity-modulated photocurrent spectroscopy (IMPS) [17,18] involves superimposition of a small sinusoidal perturbation of the light intensity on a larger steady background level. Measurement of the phase and magnitude of the photocurrent relative to the ac component of the illumination gives information about kinetics and transport. In intensity modulated photovoltage spectroscopy (IMVS)[18,19] the same illumination conditions are used, but the open circuit ac photovoltage is measured instead of the short circuit ac photocurrent. In the case of the DSC, it can be shown that IMPS provides information about electron diffusion, whereas the IMVS response is related to the electron lifetime under open circuit conditions, where photo-injected electrons are constrained to back react with I_3 .

The continuity equation describing injection, collection and back reaction of electrons in the DSC is [17,18,20]:

$$\frac{\partial n}{\partial t} = \eta \alpha I_0 e^{-\alpha(\lambda)x} + D_n \frac{\partial^2 n}{\partial x^2} - \frac{n - n_0}{\tau_n}$$

Here n is the electron density, η is the net electron injection efficiency [22], $\alpha(\lambda)$ is the absorption coefficient of the dye impregnated TiO₂, I_0 is the incident light intensity, D_n is the electron diffusion coefficient and τ_n is the electron lifetime.

It has usually been assumed that the back reaction is first order in electron density [17, 18, 20]. The possibility of a second order back reaction will be discussed elsewhere [20]. For IMPS and IMVS, the illumination intensity is time dependent:

$$I(t) = I_0 (1 + \delta e^{i\omega t})$$

where $\omega = 2\pi f$ is the modulation frequency and d is much less than unity.

The general boundary conditions are

$$D_n \left. \frac{\partial n}{\partial x} \right|_{x=0} = k_{\text{ext}} n_x = 0; \quad \left. \frac{\partial n}{\partial x} \right|_{x=d} = 0$$

Here k_{ext} is the rate constant for electron extraction at the substrate ($x=0$) and d is the film thickness. The short circuit IMPS solution is obtained by allowing k_{ext} to become large (Diffusion-limited case). For open circuit IMVS, $k_{\text{ext}}=0$.

It is important to note that IMPS and IMVS measurements are carried out under conditions where $\delta < 1$ in order to allow linearization of the system response. In effect, this means that D_n and τ_n can be treated as constant for a given value of I_0 .

The intensity dependence of D_n and τ_n can then be examined by varying I_0 , the dc light intensity, while keeping $\delta < 1$.

It can be shown that the IMVS response is a semicircle with a minimum located at $\omega_{\text{min}} = 2\pi f_{\text{min}} = 1/\tau_n$ [19,21]. The IMPS response is more complicated because it reflects both diffusion and back reaction. At low frequencies it approximates to a semicircle, whereas at higher frequencies it tends to a 45° slope characteristic of diffusion [17,18]. The high-frequency IMPS response may be distorted due to the effects of RC attenuation [17,18]. If τ_n is known, D_n can be obtained by fitting the IMPS response. If τ_n becomes large, it no longer influences the IMPS response since nearly all of the injected electrons are collected. Under these conditions, v_{min} (IMPS) is directly proportional to D_n , with the coefficient of proportionality being determined by α and d . This can be understood by noting that the delay time for collection of electrons generated at a distance x from the substrate is given by $t = x^2/D_n$.

Intensity-modulated photocurrent spectroscopy (IMPS) and transient measurements were carried out in a darkened cabinet using a diode laser (635 nm, Coherent Lablaser) as the light source. For intensity-modulated photocurrent spectroscopy (IMPS), a sinus modulation with intensity of about 1% of the total light output was added. The modulated photocurrent was measured by connecting the solar cell to a lock-in amplifier (Stanford Research Systems SR830) via a current amplifier (Stanford Research Systems SR570). Time constants were obtained using a nonlinear least-squares fitting procedure. A peltier element was used to control the temperature of the solar cell in the temperature-dependent studies. Photocurrent and voltage transients were recorded on a 16-bit resolution data acquisition board (National Instruments). Current decay transients were integrated numerically to obtain the accumulated charge in the mesoporous film.

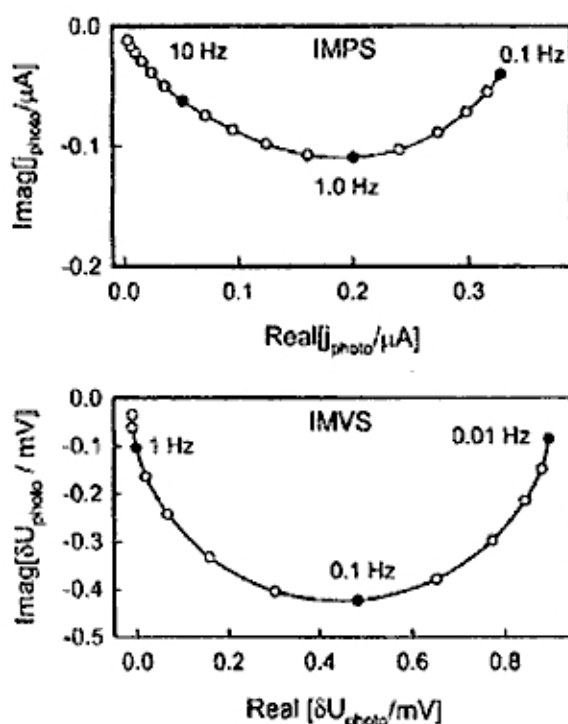


Figure 4.9. Typical IMVS and IMPS plots for DSNC at dc intensity $\sim 4 \times 10^{13} \text{ cm}^{-2} \text{ s}^{-1}$.

Figure 4.8 illustrates typical complex plane plots of the IMVS and IMPS responses for the DSC. Both plots have the shapes predicted theoretically, and they are characterized by the radial frequency of the minimum, $\omega_{\min} = 2\pi f_{\min}$. ω_{\min} was found to increase with light intensity for both the IMVS and IMPS responses.

The IMVS results show that the electron lifetime ($\omega_{\min} = 1/\tau_n$) decreases as the light intensity increases, i.e. the back reaction of electrons with tri-iodide becomes faster.

Bibliography

- [1] R. G. Gordon, *Mat. Res.Soc.*25(2000) 52-57
- [2] C. Bauer, G. Boschloo, E. Mukhtar, A. Hagfeldt, *J. Phys. Chem.B*, 105,(2001), 5585
- [3] A. Hagfeldt, M. Grätzel, *Chem.Rev.*, 95(1995), 49-68
- [4] C. J. Barbé, et al., *J.Am. Ceram. Soc.*, 80, 12(1997), 3157-71
- [5] K. Kalyanasundaram, M. Grätzel, *Coord.Chem.Rev.*, 177(1998), 347-414
- [6] A. Hagfeldt et al., *Sol.Energy Mater. Sol. Cells*, 31(1994), 481-488
- [7] K. Keis, J. Lindgren, S. E. Lindquist, A. Hagfeldt, *Langmuir*, 16(2000), 4688.
- [8] M. K. Nazeeruddin, R. Splivallo, P. Liska, P. Comte, M. Grätzel, *Chem. Commun.* (2003), 1456.
- [9] N.Papageorgiou, W.F. Maier, M. Grätzel, *J. Electrochem. Soc.*, 144(1997), 876.
- [10] B. O'Regan, M. Grätzel, *Nature*, 353(1991), 737-740
- [11] Bailes, M.; Cameron, P. J.; Lobato, K.; Peter, L. M. *J. Phys.Chem. B*, 109(2005), 15429.
- [12] Duffy, N. W.; Peter, L. M.; Rajapakse, R. M. G.; Wijayantha, K.G. U. *Electrochem. Comm.*, 2 (2000), 658.
- [13] Cameron, P. J.; Peter, L. M. *J. Phys. Chem. B*, 107(2003), 14394.

- [14] G.Binnig, H.Rohrer, C.Gerber, and E. Weibel, *Phys. Rev.Lett.*, 49,(1982), 57
- [15] L.Reimer, *Scanning Electron Microscopy: Physics of Image Formation and Mycroanalysis*, Springer-Verlag, Berlin,(1992)
- [16] D.B.Williams and C.B. Carter, *Transmission Electron Microscopy*,Plenum, New York, (1996)
- [17] L. Dlocik, O. Ileperuma, I. Lauermann, L.M. Peter, E.A. Ponomarev,G. Redmond, *J. Phys. Chem. B*, 1010 (1997), 10281.
- [18] L.M. Peter, D. Vanmaeckelbergh, in: R.C. Alkire, D.M. Kolb (Eds.),*Advances in Electrochemical Science and Engineering*, vol. 6, Wiley-Interscience, New York, (1999)
- [19] G. Schlichthörl, S.Y. Huang, J. Sprague, A.J. Frank, *J. Phys. Chem.B* ,101 (1997), 8141
- [20] S. Södergren, A. Hagfeldt, J. Olsson, S.E. Lindquist, *J. Phys. Chem.* 95 (1994) 5522
- [21] G. Franco, J. Gehring, L.M. Peter, E.A. Ponomarev, I. Uhlendorf, *J.Phys. Chem.*, 103 (1999), 692.
- [22] A.M.Fisher, L.M. Peter, E. A. Ponomarev, A.B. Walker, K. G. U. Wijayantha, *J. Phys. Chem. B.*, 104(2000), 949-958

Chapter 5 Influence of morphology and doped in ZnO photoelectrodes

Performance of solar cells has several aspects. One of the principal aspects is the semiconductor electrode preparation. Shape, size and distribution range influence directly on the efficiency of DSC.

The semiconductor morphology must also provide both high surface areas to maximize dye absorption and efficient electron transport that delivers the electron to the collection electrode without recombination. Electron transport in nanoparticle-based DSCs is proposed to occur either by a series of hopping events between trap states on neighboring particles [1] or by diffusive transport within extended states slowed down by trapping/detrapping events [2].

ZnO has probably the richest variety of different nanostructures and morphologies. Its range includes highly ordered nanowire arrays, tower-like structures, nanorods, nanobelts, nanosprings, nanocombs, and nanorings. A dense network of nanowires can provide both high surface area and direct connectivity to the electrode over distances up to the lengths of the nanorods. The ability to improve charge transport using high aspect ratio nanostructures has been observed in nanorod-polymer blend solar cells, where external quantum efficiency increases from 20% to almost 60% as the length of the nanorods are increased from 7 to 60 nm [3]

In this chapter is studied the influence of the ZnO shape in the first part, between ZnO nanorods and nanoparticles. In the second part is evaluated the use of different ions as dope in ZnO photoelectrode.

5.1. ZnO nanorods and nanoparticles in DSC

The nanorods morphology provides direct conduction paths for the electrons from the point of injection to the collection electrode while maintaining high surface area for dye adsorption. Here, it is compared a DSC based on ZnO nanorods and nanoparticles demonstrate a working cells with 25 % internal quantum efficiency and 1% energy conversion efficiency.

5.1.1. ZnO nanorods synthesis

Nanorods and nanoparticles were synthesized in similar way. Details of the synthesis are mentioned in section 4.1.2.1 .

Dye sensitization is achieved by pipetted 4 μ L of N719 in DMSO(20 mmol) onto the films and left for 1 minute (rapid method). Then it was rinsed with ethanol.

The electrolyte was HMII (1-methyl-3-hexyl-imidazoliumiodide) 0.6 M, 0.05 M I_2 and 0.5M of 4-terbutylpyridine. A platinized conducting glass was used as a counter electrode.

5.1.2. ZnO nanorods and nanoparticles characterization

In Figure 5.1, TEM picture shows ZnO nanorods(b) and nanoparticles (a) in colloidal solution. Nanorods have characteristic grains with lengthened shape with 15 nm of diameter and 70 nm long. On other hand, ZnO nanoparticles have 15-20 nm average size, with hexagonal shape.

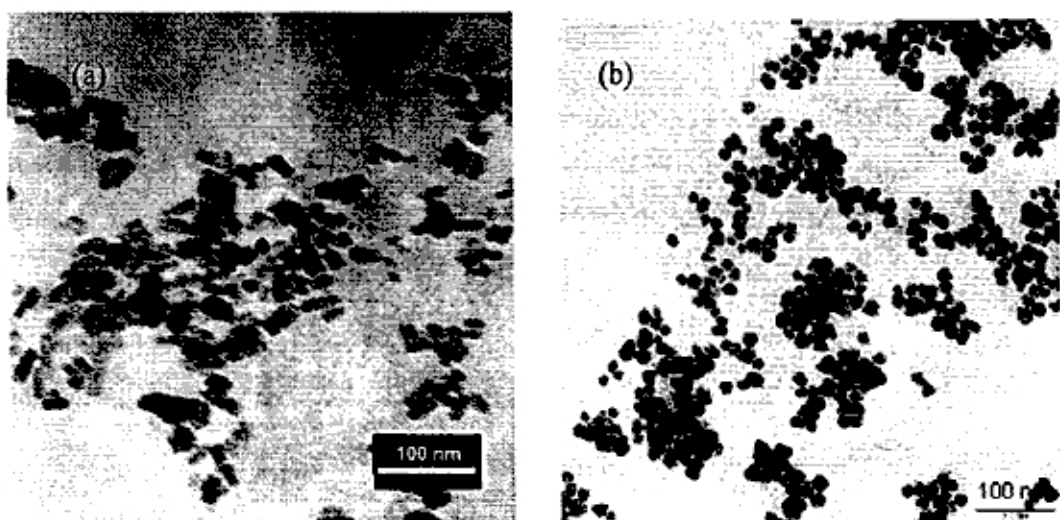


Figure 5.1 Micrography of ZnO (a) nanoparticles and (b) nanorods in colloidal solution.

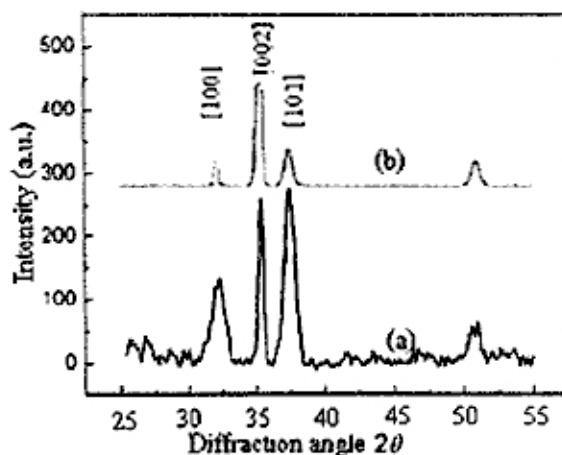


Figure 5.2 X ray diffractogram of the ZnO nanoparticle (a) and after one hour of reflux (b)

Figure 5.2 shows the XRD pattern of the as-prepared ZnO nanoparticles and nanorods. The diffraction peaks are quite similar to those of ZnO nanoparticles, which can be indexed as the hexagonal wurtzite structure ZnO ($a = 3.249 \text{ \AA}$, $c = 5.206 \text{ \AA}$). No characteristic peaks of impurities were observed. Thus, the result showed that the as-prepared products are single phase hexagonal ZnO.

5.1.3. Photoelectrochemical characterization

The photovoltaics parameters for a solar cell constructed with ZnO nanorods and nanoparticles with 100 mW/cm² and 1000 mW/cm² broadband illumination are shown in table 5.1. The short circuit photocurrent and efficiency obtained using nanorods and nanoparticles are very similar. The efficiency is slightly higher for ZnO nanoparticles

Table 5.1 Photovoltaic parameters of cells made with ZnO nanorods and nanoparticles

	1 sun				1/10 sun			
	n (%)	Voc(V)	FF	Isc(mAcm ⁻²)	n(%)	Voc(V)	FF	Isc(mAcm ⁻²)
rod	1.18	0.64	0.39	4.75	1.37	0.55	0.48	0.52
particle	1.29	0.62	0.42	5.00	1.34	0.54	0.47	0.53

IPCE reaches a maximum value of over 25% at 525 nm, near the absorbance maximum for the dye, and follows the same shape as the absorption curve for the dye adsorbed onto the ZnO nanorods and nanoparticles.

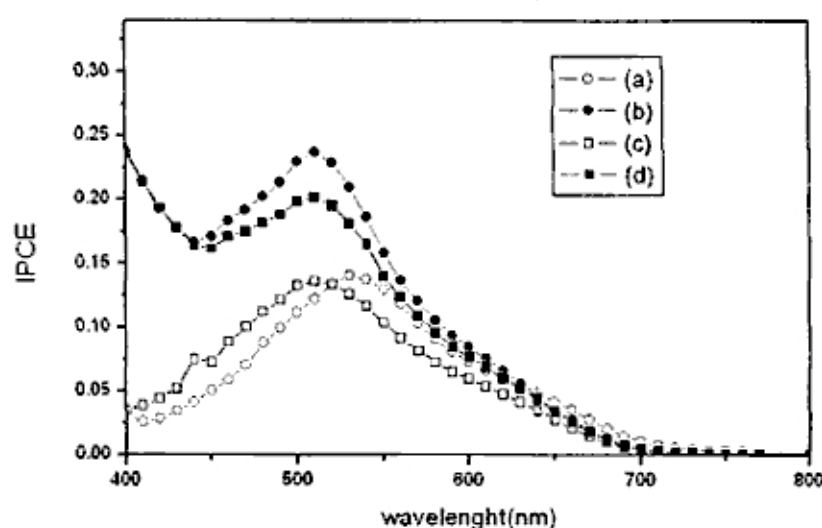


Figure 5.3. IPCE spectra for EE and SE illumination of DSC with N719 (a)EE of ZnO nanoparticles, (b) SE of ZnO nanoparticles, (c) EE of ZnO nanorods and (d) SE of ZnO nanorods.

The four curves in Figure 5.3 show the electrolyte-electrode (EE) and substrate-electrode (SE) action spectra for ZnO nanorods and nanoparticles electrodes. Higher IPCE values were obtained for electrodes prepared from ZnO nanoparticles in EE and SE illumination, consisting of highly porous, homogeneous, spherical, nanometer-sized interconnected particles.

Dividing IPCE by absorption, we find that the product of injection and charge collection efficiencies is approximately 30% (see figure 5.4). Although a small difference is observed, internal quantum efficiency confirms that the main reason for the lower current density from ZnO solar cells is the low light harvesting efficiency. This low light harvesting efficiency is probably due to lower surface area of the nanorods as compared to compacted nanoparticles.

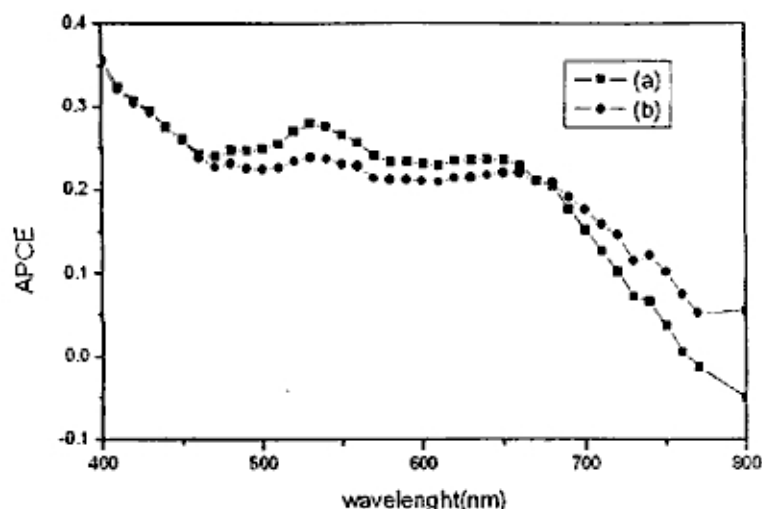


Figure 5.4 APCE spectra for ZnO nanostructured DSC with N719: (a) nanoparticle and (b) nanorod

In figure 5.5, a comparison of the current of the electrodes at a given potential reveals that the dark current J_d is much smaller than J_r , which is measured as the difference between J_{sc} and J_{ph} . This apparent inequality is ascribed to a shift of potential and can be understood from Figure 5.6 and the following analysis. In the dark, electrons flow from the SnO_2 film across the SnO_2/ZnO interface, the $\text{ZnO}/\text{solution}$ interface, and then the $\text{solution}/\text{Pt}$ interface. In the light, the direction of the electron flux is reversed.

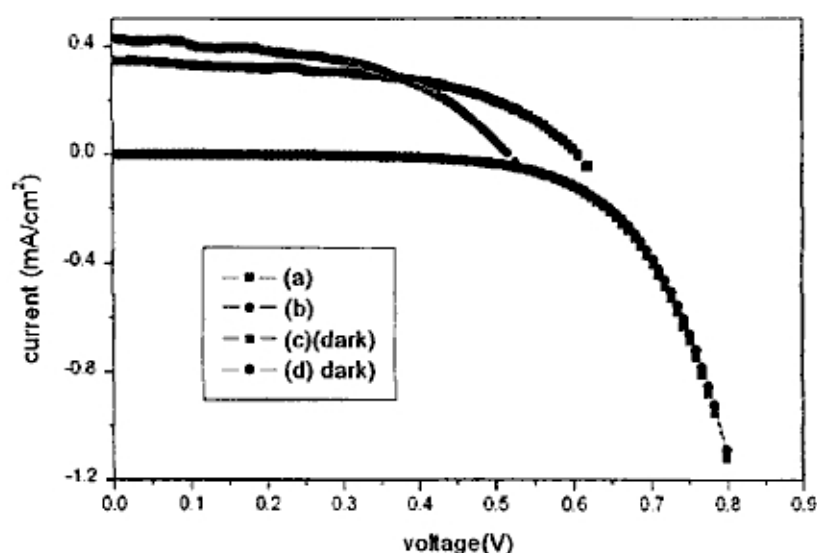


Figure 5.5 Current-voltage (I-V) behavior, under illumination and dark, of cells made with ZnO nanorod(a and c)), and with ZnO nanoparticle (b) and d)).

In figure 5.6 shows a diagram of energy levels and electron transfer pathways for a dye covered TiO_2 solar cell in the dark and under illumination. Similar to DSC TiO_2 , for electron transfer to occur, the potential of SnO_2 must be more negative located than the the ZnO potential in the dark and more positive located under illumination. Correspondingly, the potential of the Pt electrode must be positive located compared to the redox potential in the dark and negative located under illumination. Electron injection from ZnO to the charge mediator I_3^- constitutes both J_d and J_r . Under the conditions of measurements, the rate of back electron transfer from ZnO to the redox species in solution is not limited by mass transport of I_3^- ions. Thus, the redox potential of the

solution is not affected by the current and is the same in both the dark and the light. Furthermore, recombination of electrons with oxidized dye molecules is significantly slower than the reduction of the dye by I⁻ ions [4-6]. Thus, the electron concentration in ZnO governs both the magnitude of the current and the position of the Fermi level or potential of ZnO. In other words, when J_d and J_r are the same, the potential of ZnO in the dark equals that in the light. On the other hand, the applied bias between the SnO₂ film and the Pt counter electrode depends on ohmic losses within the SnO₂ and ZnO, a potential drop at the SnO₂/ZnO interface because of the presence of a barrier, and the overpotential for the redox reaction at the Pt electrode. Additional bias may be required to offset these potential losses. Thus, to generate the same J_d and J_r , the applied potential at the SnO₂ contact in the dark is shifted negatively with respect to the photopotential.

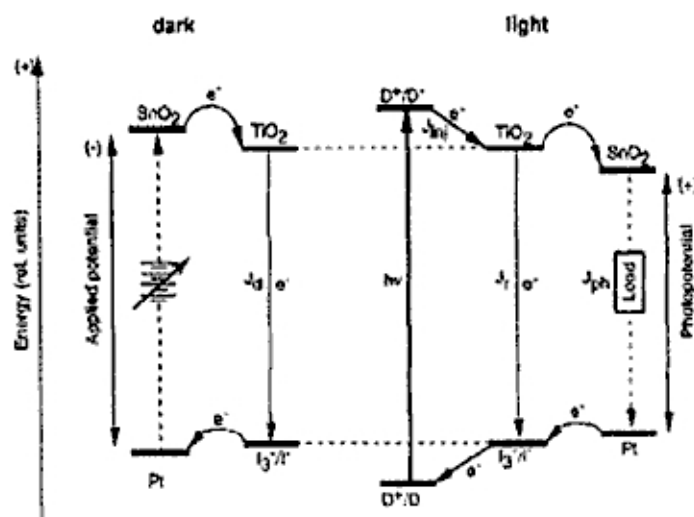


Figure 5.6 Energy levels and electron transfer pathways for a dye covered TiO₂ solar cell in the dark and under illumination[7]. Electron transfer from the Fermi level of TiO₂ to the charge mediator I₃⁻ (eq 1) constitutes both the dark current J_d and the recombination current J_r . When $J_d = J_r$, the TiO₂ potential is fixed, whether the current is a consequence of the (dark) applied bias or the light-induced charge injection J_{inj} from the dye (D⁺/D^{*}). The applied bias between the SnO₂ and Pt electrode depends on ohmic losses within the SnO₂ and TiO₂ (not shown in figure), the potential drop at the SnO₂/TiO₂ interface, and the overpotential for the redox reaction at the Pt electrode. When $J_d = J_r$, the applied potential at the SnO₂ contact is shifted negatively with respect to the photopotential.

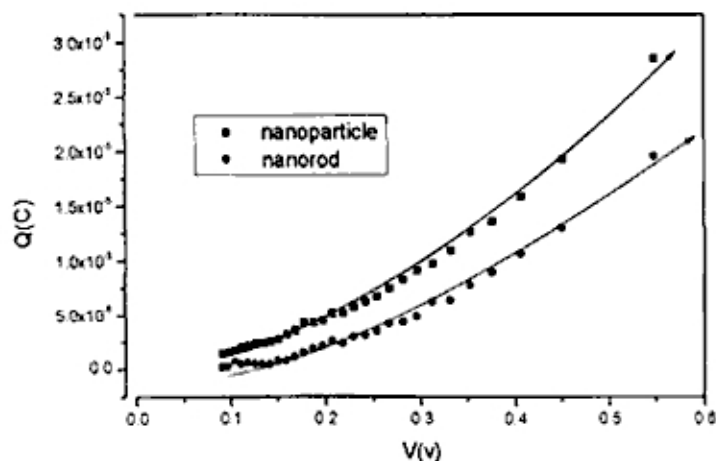


Figure 5.7 Extracted charge as function of open-circuit potential for a dye-sensitized ZnO nanorod and nanoparticle based cell. The line is an exponential fit.

The solar cell was illuminated under open-circuit conditions in order to find the relation between potential and charge, using a charge extraction technique [8]. Results are shown in Figure 5.7. The charge increases roughly exponentially with potential: $Q = Q_0 \exp(V/m)$, with $Q_0 = 2.10 \times 10^{-6} \text{ C cm}^{-2}$ and $m = 0.25 \text{ V}$ for ZnO nanorod solar cell and $Q_0 = 3.72 \times 10^{-6} \text{ C cm}^{-2}$ and $m = 0.27 \text{ V}$ for ZnO nanoparticle. It is noted that a better fit is obtained using a power-law equation. Both fitted curves are similar for ZnO nanoparticles and nanorods, also m values are closer.

5.1.4. Electron Transport Studies

The electron transport through the nanostructured metal oxides was studied using intensity-modulated photocurrent spectroscopy under short-circuit conditions[9-11] while the electron lifetime was probed using intensity-modulated photovoltage spectroscopy under open-circuit conditions[11-13] Figure 5.8 shows the IMPS and IMVS time constants as function of light intensity. The general trend for all time constants is that they decrease with increasing light intensity. The IMVS time constant, which corresponds to the electron lifetime τ_e , is similar in ZnO nanorod based solar cell with ZnO nanoparticle based solar cells.

Electron transport times in the both kinds of nanostructured ZnO were similar, and they change in the same way as a function of the incident light intensity. The films consist of porous networks of nanocrystals, having a high percentage of surface atoms and many grain boundaries. In our studies, we have a non oriented crystalline nanorods then electron transport will be limited by grain boundaries. It could be explain the similar behaviour of ZnO nanorods and nanoparticles.

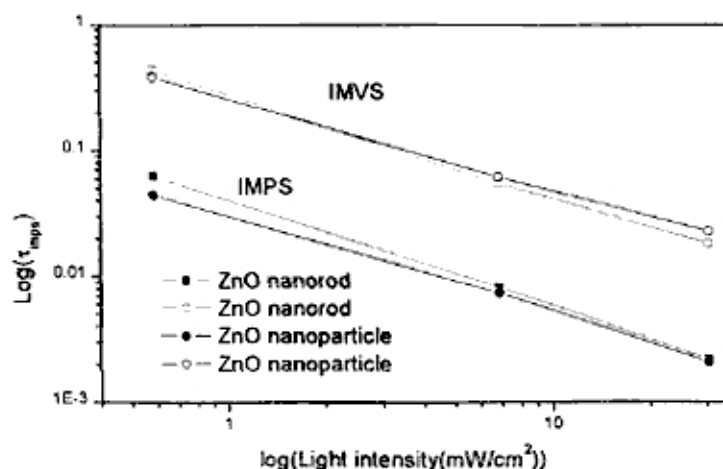


Figure 5.8 IMPS and IMVS time constants as a function of light intensity ($\lambda = 640 \text{ nm}$) for N719-sensitized ZnO and TiO₂ solar cells with electrolyte 1. Drawn lines are power-law fits.

5.2. ZnO phototelectrodes doped with Li⁺, Mg²⁺

One of the principal problems in the ZnO solar cell is the instability of ZnO in the presence of the dye, which was mentioned before. ZnO tends to react with the proton of the dye, forming Zn²⁺ on the surface of the semiconductor film. Using some thin layer of an insulating or wide-band-gap oxide, the nanostructured metal oxide to improve the performance of DSC [14-17]

Furthermore, ZnO films have a very small electrical resistivity due to the intrinsic defect existence of interstitial Li atoms [18]. The doping of Li and Mg into ZnO has been proven to be able to increase electrical resistivity [19,20]. High quality ZnO films with Li and Mg co-doping have been sought in the current film devices.

A number of different techniques have been utilized to prepare ZnO thin films. The sol-gel method is one of the attractive processes due to controllability of compositions, simple facilities, low cost, etc. In the present chapter, we investigated effects of Li and Mg doping on the microstructure and photoelectrochemical properties of ZnO solar cells. In the case of ZnO-MgO system, according to the phase diagram, the thermodynamic solubility limit of MgO in ZnO has been reported to be less than 4 mol% [21]. The large structural dissimilarity between the wurtzite ZnO and rocksalt MgO results in an unstable condition for MgZnO with high Mg content [22]. In our studies, we use low concentrations of Mg²⁺.

5.2.1. Preparation of ZnO doped Mg²⁺ photoelectrodes

The ZnO doped Mg²⁺ films were prepared as described in section 4.1.2.1.

Electrodes were immersed in D5 or N719 ethanolic solution (0.5 mM) and left for 14 hours. The temperature of contact between the dye and the film was 50°C. The films were rinsed with ethanol after the sensitization before the cell assembly.

The counter electrode was a thermally platinized conducting glass (5mM H₂PtCl₆ in dry isopropanol, heated at 380°C on a conducting glass substrate for 20 min). As a standard electrolyte we used 0.5M LiI/50 mM I₂ in 3-methoxypropionitrile.

5.2.1.1. Film characterization

Figure 5.9 shows XRD patterns of pure and doped ZnO thin films with different Mg concentrations (0.3 and 1.0 at.%) on conductor substrates (electrode a). The peaks could be indexed to a hexagonal wurtzite ZnO structure [23] for all the films with no other phase indicating these to be polycrystalline and single phase in the entire composition range studied.

It can be seen that the as synthesized powder only possesses a set of broaden peaks of ZnO, while the diffraction peaks of MgO are under the detection limit.

It is suggested that the surface energy of (002) plane is the lowest in ZnO crystal [24]. Grains with the lower surface energy become larger as the film grows. Then the growth orientation develops into one crystallographic direction of the lowest surface energy. This means that the *c* orientation maybe easily formed.

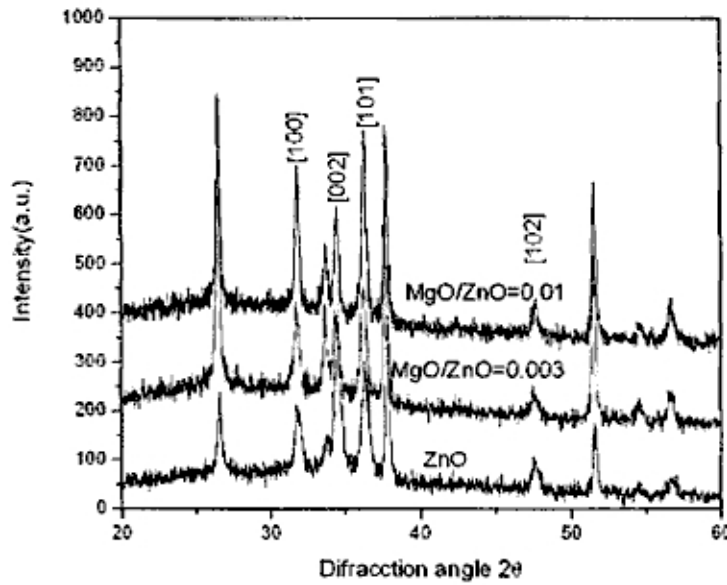


Figure 5.9 X ray diffractogram of the non doped and Mg-doped ZnO nanoparticle films on conductor glass after sintering at 400°C.

The lattice constants a and c of wurtzite structure ZnO were calculated, according to Bragg's law

$$2d \sin \theta = n\lambda$$

for Hexagonal structure of ZnO, lattice constants a and c are given by

$$\frac{1}{d_{hkl}^2} = \frac{4}{3} \left(\frac{h^2 + hk + k^2}{a^2} \right) + \frac{l^2}{c^2}$$

with the first order approximation, $n=1$:

$$\sin^2 \theta = \frac{\lambda^2}{4} \left(\frac{4}{3} \frac{h^2 + hk + k^2}{a^2} + \frac{l^2}{c^2} \right)$$

for the [100] orientation at $2\theta \sim 31.1^\circ$, the lattice constant a was calculated by

$$a = \frac{\lambda}{\sqrt{3} \sin \theta}$$

for the [002] orientation at $2\theta \sim 34.42^\circ$, the lattice constant c was calculated by

$$c = \frac{\lambda}{\sin \theta}$$

With the increase of the doping concentration, the lattice constant a decreases slightly from 3.25 to 3.245 Å, and c decreases from 5.207 to 5.18 Å. Mg lodged itself in an interstitial position, which leads to a decrease of the lattice constants.

According to Vegard's law, this is quite expected for a Mg-substituted ZnO solid solution as the ionic radius of Mg^{2+} is smaller than that of Zn^{2+} . Since the phase diagram of MgO–ZnO binary system shows a thermodynamic solid solubility of about 4% MgO in ZnO [25], a large dissimilarity in the structures between wurtzite ZnO and cubic MgO may result in nonequilibrium phase in $Mg_xZn_{1-x}O$ for higher values of x beyond the solubility limit.

5.2.1.2. Photoelectrochemical characterization

There are several factors influencing the efficiency of Mg-doped ZnO solar cells, as ratio MgO/ZnO, sintering temperature of the films, thickness of the films and nature of the dye. Here we studied the influence of the latter parameter, selecting on the conventional ruthenium based N719 and organic dye, D5. The colloid used was preliminary colloid, made with high concentration of Mg (Mg/Zn= 0.1). Then we find an optimal temperature of sintering for these electrodes. Finally Mg coated ZnO is studied at different concentrations of Mg.

Mg-doped ZnO

The solar cell dyes used in this investigation are D5, an organic dye and the ruthenium based N719, as mentioned before. Five DSCs with similar thickness of Mg-doped ZnO films (~ 4.3 μm) were prepared with the different dyes (Table 5.2).

Mg-doped ZnO films did not show better performances as photoelectrodes in solar cell. The overall efficiency is lower than the non doped ZnO, although for both dyes, fill factor values are higher for the doped ZnO electrode, probably due to the lower photocurrents observed.

When Mg-doped ZnO electrodes were sensitized in 0.5 mM N719, all the photovoltaic parameters were lower. The overall efficiency is lower. The highest I_{sc} (2.23×10^{-3} A/cm²) was obtained with D5 dye. The open-circuit voltage (V_{oc}) varied in the range of 0.31–0.57 V.

Table 5.2 Photovoltaic parameters of cells made with Mg-doped ZnO (MgO/ZnO=0.01). Films were sinterized at 450° C for 30 minutes. Thickness was 4.5 μm

dye	1000 mW/cm ²				100 mW/cm ²			
	n (%)	V _{oc} (V)	FF	I _{sc} (mA)	n (%)	V _{oc} (V)	FF	I _{sc} (mA)
D5	0.75	0.45	0.74	2.23	0.93	0.57	0.62	0.263
N719	0.05	0.31	0.69	0.22	0.10	0.40	0.62	0.041

In conclusion, the first optimization procedure was varying the temperature after synthesis. The temperature was varied from 350–600°C. It was observed that when the temperature was increased the particle size increased and became less uniform in size. As the temperature decreases the Mg-doped ZnO particles have fewer chances to aggregate and, therefore, there exists fewer bigger particles. The temperature effect on the crystallinity has not been currently investigated.

In the table 5.3, the short circuit current (I_{sc}) decreased with higher temperature. The highest I_{sc} (2.76×10^{-3} A/cm²) was obtained at 400°C and the lowest I_{sc} (0.74×10^{-4} A/cm²) was obtained at 600°C. A highest overall light-to-electric energy conversion efficiency of 1% was obtained with the electrodes sensitized with D5 at 400°C.

Table 5.3 Photovoltaic parameters of cells made with Mg-doped ZnO (MgO/ZnO=0.03). Films were sinterized at different temperatures. Dye sensitization was made in ethanolic solution of D5(5mM). The film thickness was 4.5 μm

Temp (C)	1 sun				1/10 sun			
	n (%)	Voc(V)	Isc(mA)	FF	n(%)	Voc(V)	Isc(mA) $\times 10^{-1}$	FF
600	0.26	0.52	0.74	0.68	0.22	0.51	0.76	0.56
500	0.61	0.51	1.74	0.68	0.65	0.55	2.00	0.59
450	0.82	0.52	2.16	0.72	0.99	0.59	2.63	0.62
400	0.98	0.51	2.76	0.71	1.12	0.61	2.99	0.60
350	0.72	0.51	2.01	0.69	0.90	0.59	2.30	0.61

MgO-coated ZnO electrodes

The impregnation of an already sintered colloidal ZnO electrode with magnesium acetate solution followed by firing to deposit a MgO coating around the ZnO particles did not improved the I - V characteristics. However, the photovoltage and fill factor were always inferior to those obtained by the addition of magnesium chloride to the ZnO colloid before sintering.

The I - V characteristics of thin layer electrodes prepared from such modified ZnO films are shown in Figure 5.3. An increase in the open-circuit voltage with respect to that of the unmodified ZnO electrode is observed (table 5.1), despite the very low insulator coverage, but the photocurrent diminishes, resulting in an overall loss of energy conversion efficiency. The decrease in the photocurrent probably results from poor electrical contact between the particles caused by their insulating shell reducing the charge collection efficiency.

Table 5.3 Photovoltaic parameters of cells made with Mg-doped ZnO. Films were sinterized at 400°C. Dye sensitization was made in ethanolic solution of D5(5mM). The film thickness was 4.5 μm

MgO/ZnO	1 sun				1/10 sun			
	n (%)	Voc(V)	FF	Isc(mA)	n(%)	Voc(V)	FF	Isc(mA)
1 %	0.63	0.71	0.45	1.93	0.82	0.62	0.54	0.242
0.1 %	0.71	0.71	0.43	2.34	0.98	0.63	0.55	0.285
0.01 %	1.06	0.75	0.38	3.70	1.57	0.64	0.54	0.458

None of the modified ZnO electrodes is as efficient in solar energy conversion as the pure ZnO electrode (Table 5.1).

5.2.2. Preparation of ZnO doped Li⁺ photoelectrodes

ZnO doped Li⁺ films were deposited as described in section 4.1.2.1.

Dye sensitization is achieved by pipetted 4 μL of the N719 in DMSO (20 mmol) onto the films and left for 1 minute. The temperature of contact between the dye and the film was 50°C and was followed by rinsing with ethanol.

The electrolyte was HMII (1-methyl-3-hexyl-imidazoliumiodide) 0.6 M, 0.05 M I₂ and 0.5 M of 4-terbutylpyridine. A platinized conducting glass was used as counter electrode.

5.2.2.1. Film characterization

Figure 5.11 shows the XRD patterns of the as-deposited ZnO films with different Li/ZnO molar ratios. XRD patterns of these samples are in agreement with the typical wurtzite structure ZnO diffraction pattern (hexagonal phase, space group $P6_3mc$, JCPDS No. 36-1451). Sharp diffraction peaks shown in Figure 5.11 indicate good crystallinity of ZnO films. No characteristic peak related to Li compounds or other impurity was observed.

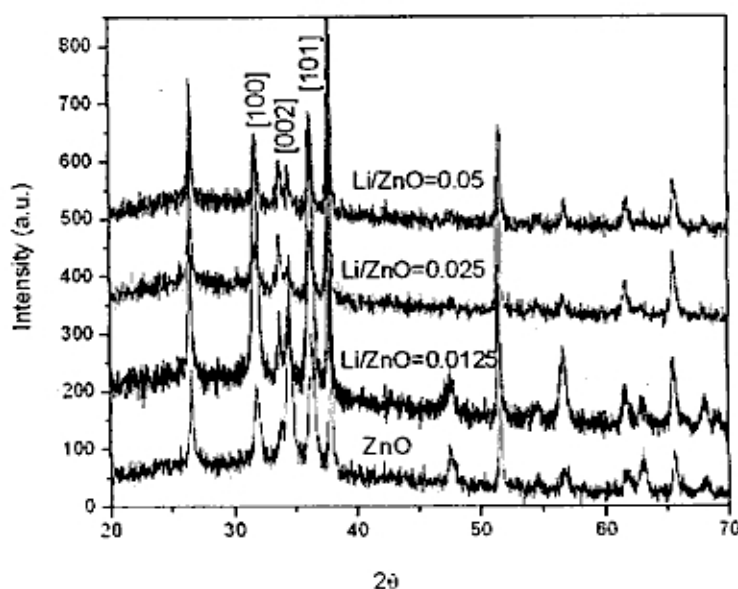


Figure 5.11 X ray diffractogram of the non doped and Li-doped ZnO nanoparticle films on conductor glass after sintering at 380 C

We can observe (Figure 5.11) as the amount of doped Li increased, the intensity and angle of (002) diffraction peaks are also decreased and increased, respectively. These results indicate that the lattice constants of ZnO crystals are gradually decreased due to substitution of smaller Li atom than Zn atom. In detail, with increasing Li contents, asymmetric (002) diffraction peak that is attributed to Li doped ZnO thin film formation is appeared and the diffraction angle is also shifted toward high degree from 34.41° to 34.58° . We index the lower angle (about 34.41°) peak (I) as pure ZnO (002) peak and the higher angle (above 34.58°) peak (II) as Li doped ZnO (002) peak, respectively. In Figure 5.11, the shapes of ZnO (002) peaks are asymmetric and they are gradually shifted toward higher angle as Li doping amounts increase. This suggests that the lattice constants in the *c*-axis of ZnO crystal (or films) decrease with a substitution of Li ion into Zn sites. It is known generally that dopants can be substituted or inserted, depending on the doping ions size. Yamamoto and co-workers [26] reported that most doping ions (larger size than Zn ion) substituted for Zn ion sites in the doping case. Moreover, it can also cause the dopants to be inserted to between zinc ion and oxygen ion because of the small size ion. Of the two cases, the former is in good agreement with our data.

5.2.2.2. Photoelectrochemical measurements

The current-voltage characteristics of Li-doped ZnO solar cells are showed in the table 5.3. The maximum efficiency and photocurrent reached in 2.5% Li/ZnO ratio are as high as 1.44% and 4.49 mAcm^{-2} , respectively.

Table 5.3 Photovoltaic parameters of cells made with Li-doped ZnO. Films were sinterized at 380°C. Dye sensitization was with N719 in DMSO (20mM). Film thickness was 4.5 μm

Li/ZnO	1 sun				1/10 sun			
	n (%)	Voc(V)	FF	Isc(mA)	n(%)	Voc(V)	FF	Isc(mA)
5%	1.23	0.64	0.47	4.07	0.86	0.69	0.56	0.41
2.5%	1.44	0.63	0.52	4.49	1.34	0.53	0.57	0.44
1.25%	1.09	0.57	0.51	3.73	1.08	0.48	0.56	0.40

The IPCE action spectrum of Li-doped ZnO/N719 solar cells is shown in figure 5.12. The maximum IPCE of ~30% (at 520 nm) was obtained by using a 0.025 Li/ZnO electrode. It is important to note the IPCE decreased with other Li/ZnO ratios. Also, the maximum around 520 nm flattened out for all the Li-doped ZnO films. Same optimum is obtained on I-V measurements, mentioned above.

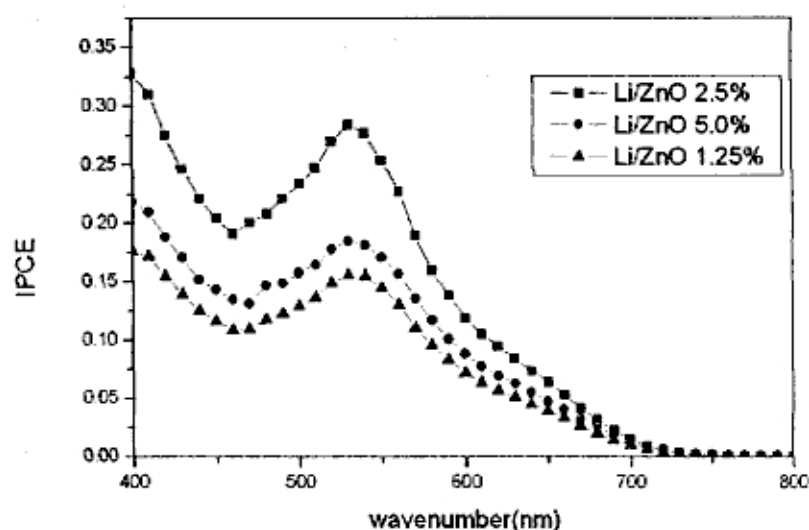


Figure 5.12 IPCE spectra of Li-doped ZnO nanostructured DSC with N719

5.2.2.3. Electron Transport studies

Results are shown in Figure 5.13. The charge increases exponentially with potential, for each Li/ZnO rate, we fitted a power law equation $Q = Q_0 \exp(V/m)$. In table 5.4 Q_0 (C cm^{-2}) and m (V) are listed.

Table 5.4 Constants Q_0 and m of power law equation from Li-doped ZnO solar cells

Li/ZnO	$Q_0(\text{C cm}^{-2}) \times 10^{-6}$	m
0	3.46	0.23
1.25%	3.21	0.23
2.5%	2.23	0.22
5%	0.47	0.15

According to potential-charge relation graph (Figure 5.13), we can calculate the total density of traps in the ZnO. The electron transport properties are explained with trapping and detrapping models (detailed later in the next section). In this case, at high

concentration of Li+ (5%) the quantity of traps are 160 that decrease with diminishing concentration of Li+.

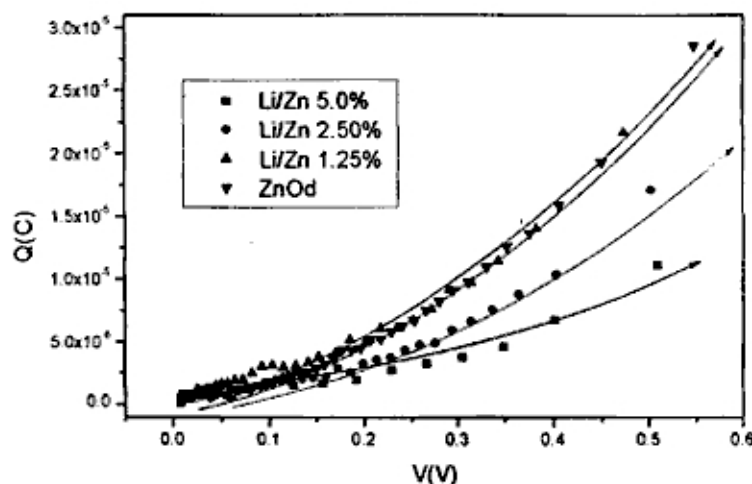


Figure 5.13 Extracted charge as function of open-circuit potential for N719 sensitized Li-doped ZnO solar cell . The drawn line is an exponential fit.

Figure 5.14 shows the IMPS and IMVS time constants as function of light intensity. The general trend for all time constants is that they decrease with increasing light intensity as previous measurements on ZnO solar cells. Electron transport times in Li-doped ZnO were similar, and they change in the same way as a function of the incident light intensity. In the next chapter we compare nanostructured ZnO with TiO₂, finding similar results for electron transport.

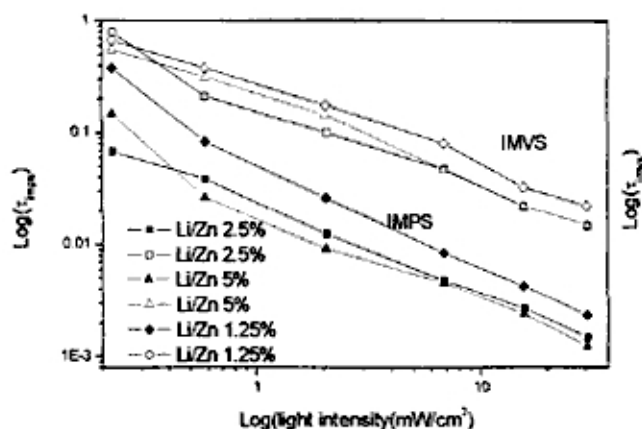


Figure 5.14 IMPS and IMVS time constants as a function of light intensity ($i = 640 \text{ nm}$) for N719-sensitized Li-doped ZnO solar cells. Drawn lines are power-law fits

Bibliography

- [1]K. D. Benkstein, N. Kopidakis, J. van de Lagemaat, and A. J. Frank, *J.Phys. Chem. B*, 107(2003), 7759.
- [2]J. Bisquert, D. Cahen, G. Hodes, S. Ruhle, and A. Zaban, *J. Phys. Chem.B*, 108(2004), 8106

- [3] W. U. Huynh, J. J. Dittmer, and A. P. Alivisatos, *Science*, 295(2002), 2425.
- [4] M. Grätzel, *Renewable Energy*, 5(1994), 118.
- [5] A. Hagfeldt; S. E. Lindquist; M. Grätzel, *Sol. Energy Mater. Sol. Cells*, 32(1994), 245
- [6] A. Hagfeldt; M. Grätzel, *Chem. Rev.*, 95(1995), 49.
- [7] S. Y. Huang, G. Schlichthorl, A. J. Nozik, M. Grätzel, and A. J. Frank, *J. Phys. Chem. B*, 101 (1997), 2576-2582
- [8] N. W. Duffy, L. M. Peter, R. M. G. Rajapakse, K. G. U. Wijayantha, *Electrochem. Commun.*, 2 (2000), 658
- [9] F. Cao, G. Oskam, P. C. J. Searson, *Phys. Chem.*, 100(1996), 17021.
- [10] L. Dloczik, O. Illeperuma, I. Lauermañ, L. M. Peter, E. A. Ponomarev, G. Redmond, N. J. Shaw, I.J. Uhlendorf, *Phys. Chem. B*, 101(1997), 10281.
- [11] A. C. Fisher, L. M. Peter, E. A. Ponomarev, A. B. Walker, K. G. U. J. Wijayantha, *Phys. Chem. B*, 104(2000), 949.
- [12] G. Schlichthörl, S. Y. Huang, J. Sprague, A. J. J Frank, *Phys. Chem. B*, 101(1997), 8139.
- [13] G. Schlichthörl, N. G. Park, A. J. J. Frank, *Phys. Chem. B*, 103(1999), 782
- [14] K. Tennakone, I. R. M. Kottegoda, L. A. A. De Silva, V. P. S. Perera, *Semicond. Sci. Technol.*, 14(1999), 975.
- [15] A. Zaban, S. G. Chen, S. Chappel, B. A. Gregg, *Chem. Commun. (Cambridge)* (2000), 2231.
- [16] A. Kay, M. Grätzel, *Chem. Mater.*, 14 (2002), 2930.
- [17] M. Ohyama, H. Kozuka, T. Yoko, and S. P. J. Sakka, *Ceram. Soc. Jpn.*, 104(1996), 296-300.
- [18] J.H. Lee, K.H. Ko, B.O. Park, *J. Cryst. Growth*, 247 (2003) 119.
- [19] A.M. Galal, M. El-Maghraby, *E.A. Abu, Physica.B*, 949 (2001), 308-310.
- [20] N. Takahiro, S. Tamaki, A. Atsushi, *J. Cryst. Growth*, 533 (2002), 237-239.
- [21] J.F. Sarver, F.L. Katnack, F.A. Hummel, *J. Electrochem. Soc.* 106 (1959) 960.
- [22] J. Chen, W.Z. Shen, N.B. Chen, *J. Phys.: Condens. Matter.*, 15 (2003) L475.
- [23] *Selected Powder Diffraction Data for Metals and Alloys* _JCPDS, Swarthmore, Vol. I, (1978)
- [24] K. L. Chopra, S. Major, and D. K. Pandaya, *Thin Solid Films*, 102(1983), 1.
- [25] E. R. Segnit and A. E. Holland, *J. Am. Ceram. Soc.*, 48(1965), 412.
- [26] T. Yamamoto, H.K. Yoshida, *J. Cryst. Growth*, 552 (2000), 214-215.

Chapter 6 Comparison between ZnO and TiO₂ dye sensitized solar cell

In this chapter we compare the electron transport, accumulation, and recombination properties of dye-sensitized solar cells based on nanostructured electrodes of ZnO and TiO₂. There is a remarkable similarity in the transport properties of the two materials, despite the significant difference in the mobility and the effective mass of electrons in the conduction band of the pure, single-crystalline materials.

6.1. Film characterization

ZnO colloids were prepared in ethanol by addition of tetramethylammonium hydroxide to a suspension of zinc acetate in ethanol, as presented in the experimental chapter. Transparent nanostructured ZnO electrodes were obtained by depositing the paste onto conducting glass substrates (TEC8, Pilkington) by doctor blading, followed by heating in a hot-air stream at 380 °C for 30 min. Transparent nanostructured TiO₂ electrodes were prepared from HNO₃-stabilized TiO₂ colloids autoclaved for 15 h at 230 °C as mentioned in the section 4.1.2.1. Film thickness (3-4 μm) was determined by profilometry.

The electrolyte composition was as follows:

Electrolyte 1: 0.5 M LiI; 50 mM I₂ in 3-methoxypropionitrile with 0.1 M 1-methylbenzimidazole

Electrolyte 2: 0.5 M LiI; 50 mM I₂ in 3-methoxypropionitrile with 0.5 M 4-*tert*-butylpyridine as an additive.

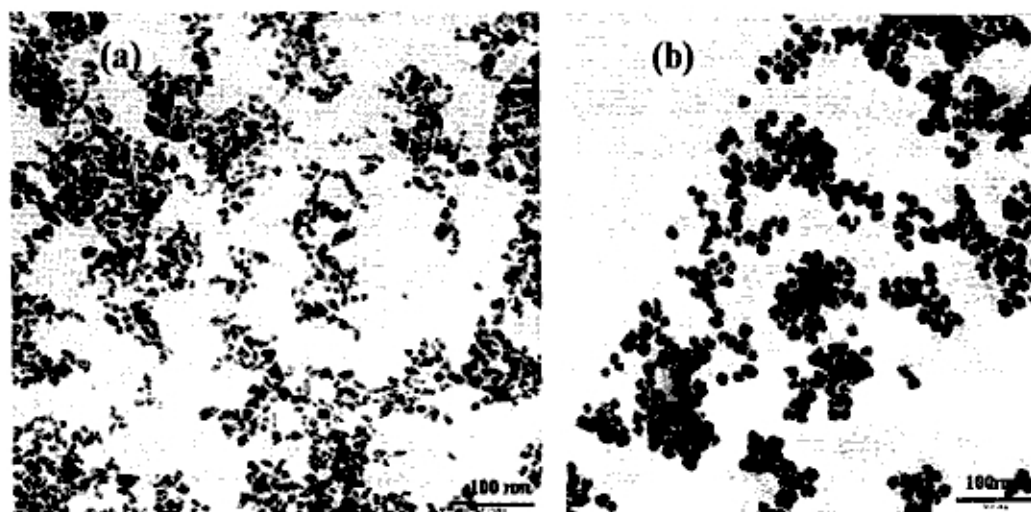


Figure 6.1 Transmission electron microscope picture of colloidal ZnO (b) and TiO₂(a)

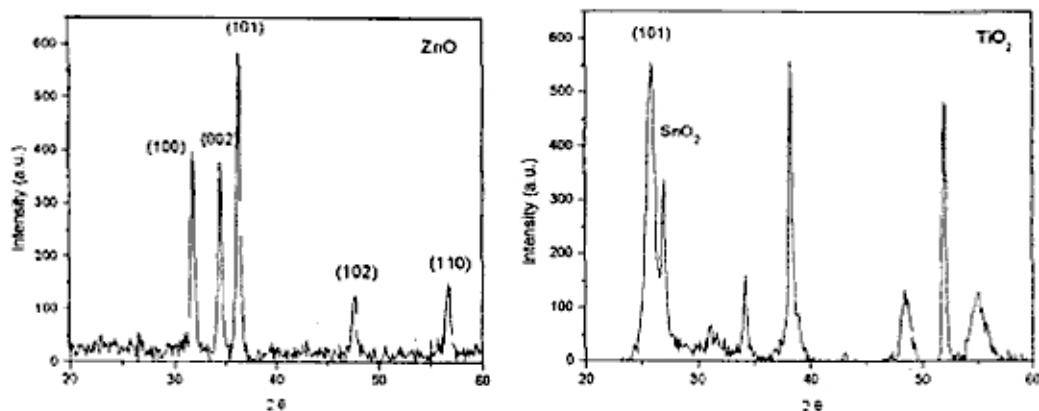


Figure 6.2 X-ray diffractograms of ZnO and TiO₂ films sintered at 380° and 450° C respectively. TiO₂ film is on conducting glass substrate

Transmission electron microscopy (TEM) revealed that colloidal ZnO solution consisted of crystalline particles with an average size of about 15 nm. The colloidal TiO₂ solution used in this study contained slightly smaller nanoparticles with an average size of 10 nm found by TEM, see Figure 6.1. The X-ray diffraction spectrum of a sintered nanostructured ZnO film is shown in Figure 6.2 and shows peaks characteristic of wurtzite. The grain size, calculated from the peak broadening using the Scherrer formula, was 16 nm. The TiO₂ films consist of 14-nm-size anatase crystals with a trace of brookite (Figure 6.2). The results suggest that significant crystal growth occurs in the TiO₂ films during heat treatment, but not in ZnO films. The resulting nanostructured ZnO and TiO₂ films were fully transparent.

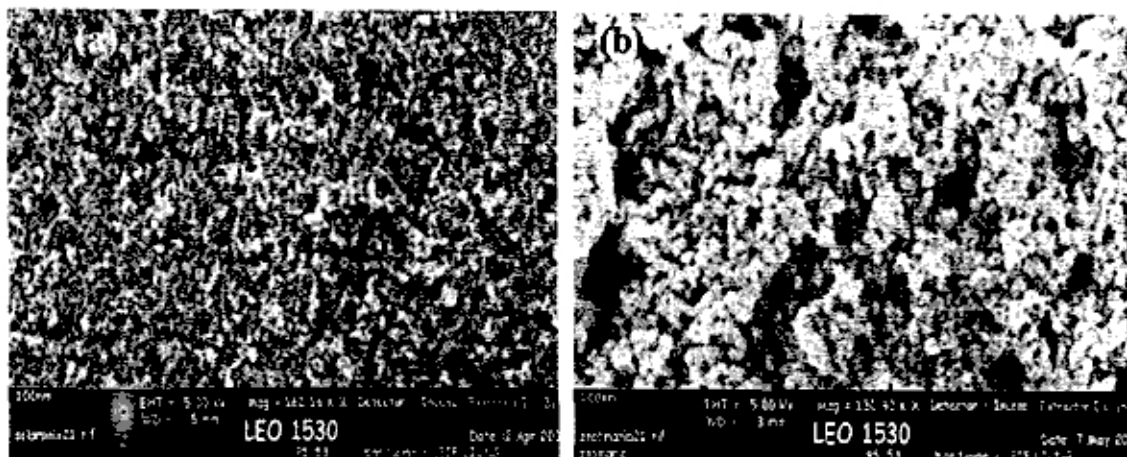


Figure 6.3 SEM picture of TiO₂ (a) and ZnO (b) film (transparent colloids)

The SEM pictures of TiO₂ and ZnO film are shown in the figure 6.3. The films of TiO₂ and ZnO, have similar morphology consisting of spherical particles with 15 nm and 25 nm, respectively. This suggest that agregation of the particles occurs in ZnO films during heating, since as ZnO colloid has not organic polymers.

A rapid method for dye adsorption was used to sensitize the films. This method was chosen to prevent sensitization problems in the case of ZnO, which can slightly dissolve in acidic environment, resulting in a precipitate of Zn²⁺ and the dye.[1] The optimum adsorption time was 1 min for ZnO solar cells. UV-vis absorption spectra of sensitized

ZnO and TiO₂ films are shown in Figure 6.4. Slightly more of the N719 dye was adsorbed by TiO₂. Importantly, the absorption maximum of the adsorbed dye on ZnO was not blueshifted. This gives evidence that there is no formation of the Zn²⁺-dye complex[1].

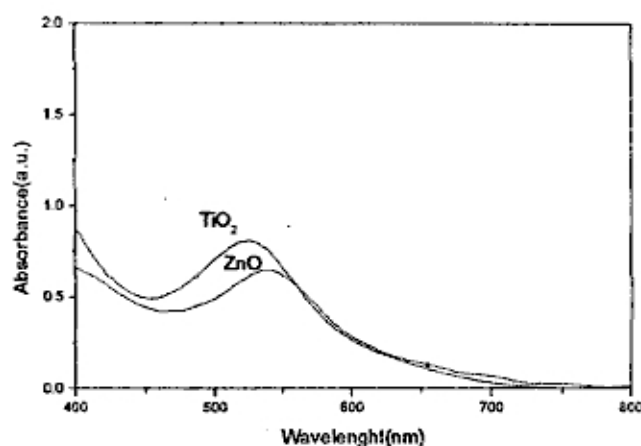


Figure 6.4 Absorption spectra of N719-dye adsorbed on ZnO and TiO₂ films (thickness 4 μm). The spectra are corrected for ZnO, TiO₂ and substrate absorption

6.2. Photoelectrochemical measurements

Current-voltage characteristics of the ZnO and TiO₂ solar cells in simulated sunlight are shown in Figure 6.5. TiO₂ solar cells give higher power conversion efficiencies than corresponding ZnO solar cells, as they give higher photocurrents, open circuit potentials, and fill factors. The overall efficiency was found to be rather low for all cells (<3%), as the nanostructured films were relatively thin. Also, the rapid dye adsorption may be a cause for low efficiency, although good results with this method have been reported by Nazeeruddin et al. for TiO₂-based solar cells [2].

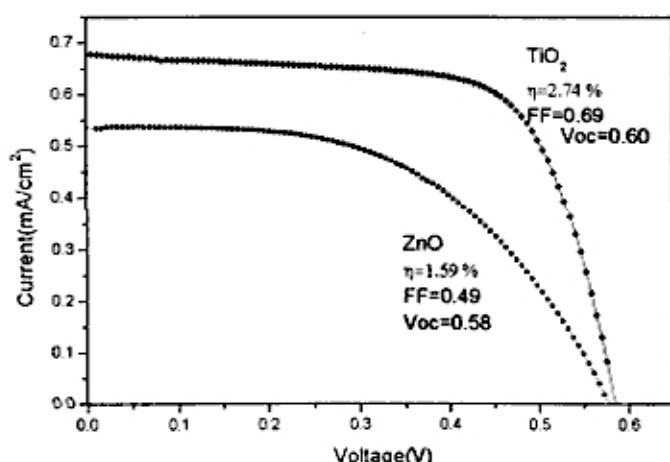


Fig.6.5 I-V characteristics for solar cells based on 4 μm thick nanostructured ZnO and TiO₂ films with rapid dye-adsorption (1 minute in 20 mM N719 in DMSO). The light intensity corresponds to 100 W/m^2 with AM 1.5G spectral distribution (1/10 sun). Electrolyte 1.

IPCE spectra of N719-sensitized ZnO and TiO₂ solar cells are shown in Figure 6.5. The photocurrent generation efficiencies are higher for TiO₂ than for ZnO, being 50% and 37% at the maximum at 520 nm for TiO₂ and ZnO, respectively. The incident photon to current conversion efficiency can be described as the product of four terms:

$$\text{IPCE} = (\text{LHE})\Phi_{\text{inj}}\Phi_{\text{reg}}\eta_c$$

where LHE is the light-harvesting efficiency, defined as $\text{LHE} = 1 - 10^{-A}$ with A is the sample absorbance, Φ_{inj} is the quantum yield for electron injection, Φ_{reg} is the quantum yield for regeneration of the oxidized dye by iodide, and η_c is the collection efficiency of injected electrons at the conducting substrate. The absorbed photon to current efficiency (APCE) is shown in Figure 6.6 b, was calculated by dividing the IPCE by the LHE. In most of the visible light range APCE values for ZnO and TiO₂ solar cells are rather constant at about 40% and 60%, respectively. As will be discussed later, losses during charge collection appear to be very low. The rather low quantum efficiencies must therefore be attributed to poor electron injection efficiency and/or dye regeneration efficiency. The rapid sensitization method is likely to give dye aggregates that are less efficient in both electron injection[3] and dye regeneration by iodide.

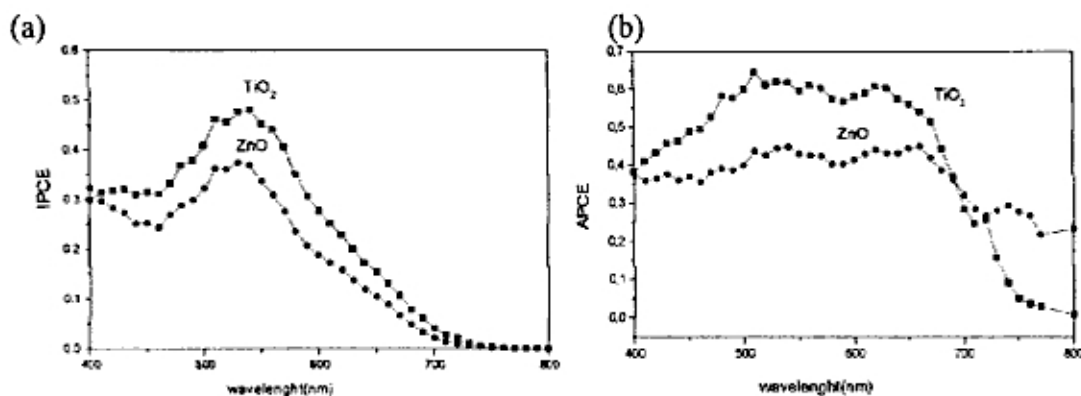


Figure 6.6 IPCE(a) and APCE spectra (b) of N719-sensitized ZnO and TiO₂ solar cells. Electrolyte 1

6.3. Electron transport studies

Several time and frequency domain measurement techniques were used to further characterize the nanostructured ZnO and TiO₂ solar cells. The electron transport through the nanostructured metal oxides was studied using intensity-modulated photocurrent spectroscopy under short-circuit conditions[4-6] while the electron lifetime was probed using intensity-modulated photovoltage spectroscopy under open-circuit conditions[6-8] Figure 6.7a shows the IMPS and IMVS time constants as function of light intensity. The general trend for all time constants is that they decrease with increasing light intensity. The IMVS time constant, which corresponds to the electron lifetime τ_e , is larger in ZnO than in TiO₂ solar cells. As τ_e is much larger than τ_{IMPS} , τ_{IMPS} can be interpreted as the electron transport time in the investigated solar cells[8] Electron transport times in nanostructured ZnO were similar to those in TiO₂, and they change in the same way as a function of the incident light intensity. It is noted that the electron mobility in single crystals is at least 1 order of magnitude larger in ZnO[9] than in TiO₂ (anatase)[10]

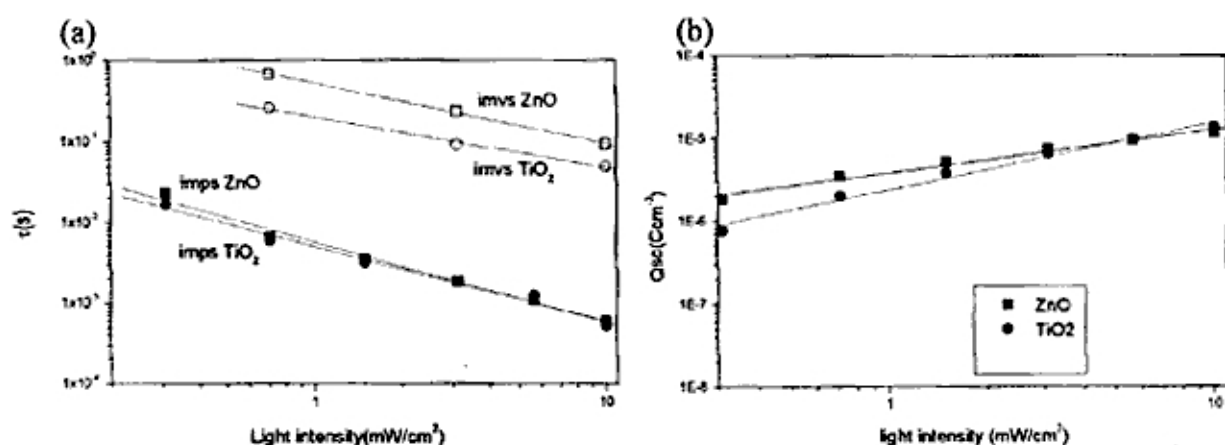


Figure 6.7 (a) IMPS and IMVS time constants as function of light intensity for N719-sensitized ZnO and TiO₂ solar cells. Drawn lines are power-law fits. Electrolyte 1. (b) Extracted short-circuit charge (Q_{sc}) as function of light intensity for the same solar cells.

The similarity of the electron transport times in the nanostructured metal oxide solar cells suggests that they are to a large part determined by the morphology of the film. The films consist of porous networks of nanocrystals, having a high percentage of surface atoms and many grain boundaries. It was demonstrated recently by Galoppini et al. that very rapid transport ($<30 \mu\text{s}$) occurred in DSCs based on ZnO nanorods [11]. In the single-crystalline nanorods electron transport will not be limited by grain boundaries.

The amount of charge present in the nanostructured metal oxide film was determined by photocurrent transients under short-circuit conditions. The current after switching off the light was measured over 1 s and integrated numerically to obtain Q_{sc} . It is noted that a fraction of the electrons can recombine before they are extracted. The fact that τ_e is much larger than τ_{IMPS} suggests, however, that most charge will be extracted. Furthermore, not all electrons may be extracted during the integration period. This can result in a systematic underestimation of the charge. The extracted charge increases with light intensity and is quite similar for the ZnO and TiO₂ solar cells at higher light intensities; see Figure 6.7 b. At lower intensities, more charge was extracted for the ZnO cell. At the highest light intensity, the charge in the ZnO electrode was about $10^{-5} \text{ C cm}^{-2}$. As the ZnO film is $4 \mu\text{m}$ thick and 50% porous, this corresponds to an electron concentration in the ZnO of $3 \times 10^{17} \text{ cm}^{-3}$, or on average about 0.6 electron per nanocrystal assuming spherical particles with a diameter of 16 nm.

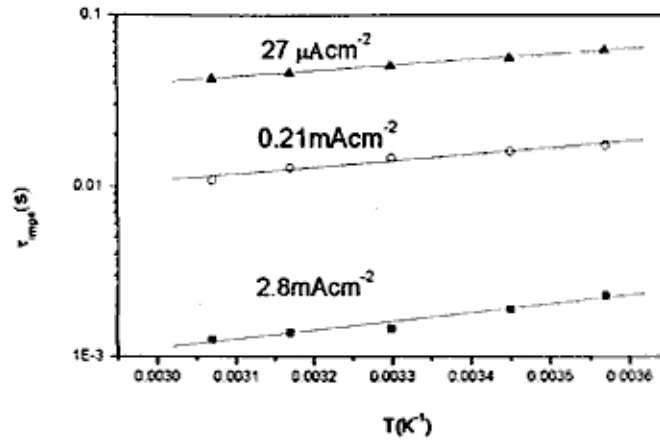


Figure 6.8 Temperature dependence of the electron transport (τ_{imp}) in a N719-sensitized ZnO solar cell. Electrolyte 2. The calculated activation energies are listed in Table 1

Results of temperature-dependent IMPS measurements on dye-sensitized nanostructured ZnO under short-circuit conditions are shown in Figure 6.8. Short-circuit current densities were practically independent of the temperature. IMPS time constants decreased with increasing temperature, indicating that the charge transport process is thermally activated. Apparent activation energies (E_a), determined using the Arrhenius equation, were rather small, 0.07-0.10 eV, and similar to those measured for dye-sensitized TiO_2 under similar conditions.[12]

Table 6.1 Activation energies for charge transport in dye-sensitized nanostructured ZnO solar cells

Light intensity (mW cm^{-2})*	J_{SC} (mA cm^{-2})	$E_a \pm 10\%$ (eV)
24.4	2.8	0.10
1.6	0.21	0.08
0.2	0.027	0.07

*Red light, $\lambda_{\text{max}} = 640 \text{ nm}$

Figure 6.9 a shows the decay of the open-circuit potential that follows after switching off the light for ZnO and TiO_2 solar cells. The decay is significantly slower in the ZnO cell, in agreement with the larger IMVS time constants found for ZnO. The electron lifetime can be calculated from the voltage transients using eq 2:[13]

$$\tau_e = -\frac{kT}{e} \left(\frac{dV_{oc}}{dt} \right)^{-1}$$

where k is the Boltzmann constant, T is the absolute temperature, and e is the positive elementary charge. The calculated electron lifetimes are shown in Figure 6.9 b as function of the open-circuit potential.[14] The lifetime increases approximately exponentially with decreasing voltage. For the TiO_2 cell there appears to be a change in recombination mechanism when the voltage decreases.

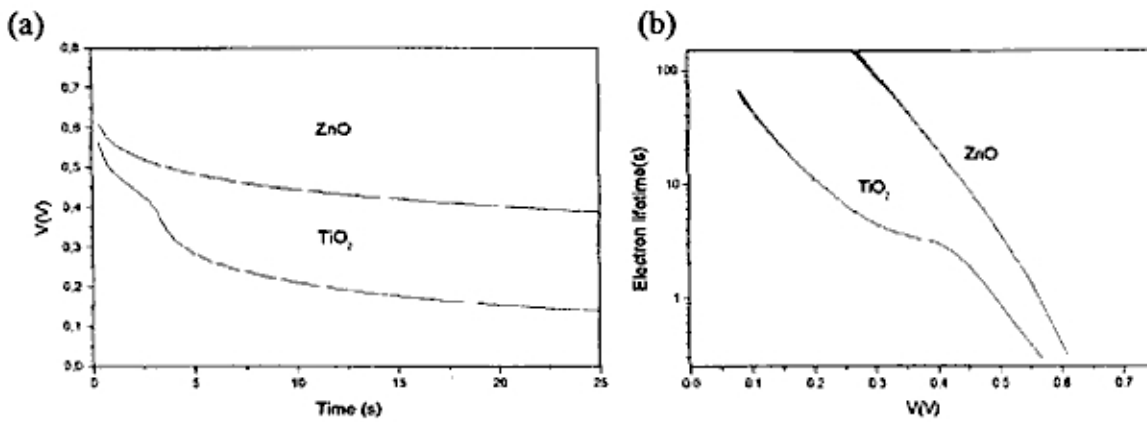


Figure 6.9 (a) Open circuit voltage decay transients of dye-sensitized nanostructured ZnO and TiO₂ solar cells. (b) Calculated electron lifetime vs open circuit potential. Electrolyte 1.

This may be related to the relative importance of recombination via the conducting glass substrate (SnO₂:F) that may be dominant over the recombination via the nanostructured TiO₂ at lower potentials.[15] In the ZnO solar cell, however, no such effect is seen. This could be a consequence of a more complete coverage of the conducting glass in case of the nanostructured ZnO electrode due to the absence of polymer in the preparation solution. Additionally, some dissolved zinc ions may have been present in the ZnO colloidal solution, which could have resulted in a dense ZnO underlayer on the conducting glass substrate.

The relation between potential and charge in the nanostructured ZnO solar cell was investigated using a charge extraction technique [16]. The solar cell was illuminated under open-circuit conditions, the potential was left to decay in the dark for a fixed time, and finally the charge was extracted by discharging over a 100 ohm resistor. Results are shown in Figure 6.10. At an open circuit potential of 0.56 V the electron concentration per ZnO nanocrystal is about 5. The charge increases roughly exponentially with potential: $Q=Q_0 \exp(V/m)$, with $Q_0=5.5 \times 10^{-6} \text{ C cm}^{-2}$ and $m = 0.19 \text{ V}$. It is noted that a better fit is obtained using a power-law equation. Part of the extracted charge is related to discharge of double-layer capacitance of the conducting glass/electrolyte interface, but its contribution is relatively small at higher potentials. The difference may be explained by differences in the electrolytes and in the ZnO batch that was used. To get insight into the electrochemical potential present in the illuminated dye-sensitized nanostructured ZnO film under short-circuit conditions, the following experiment was performed: the solar cell was illuminated for some time under short-circuit conditions, then the light was switched off and the cell switched to open circuit simultaneously[12]. The voltage that developed gives a good indication of the electrochemical potential (the quasi Fermi level) under short-circuit conditions; see Figure 6.11a.

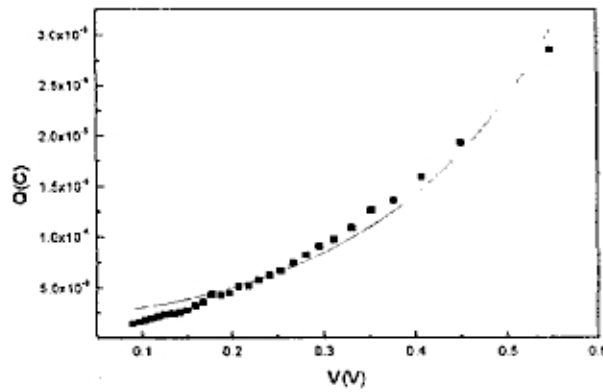


Figure 6.10 Extracted charge as function of open-circuit potential for a dye-sensitized nanostructured ZnO cell. Electrolyte 2.

We will refer to the maximum voltage that develops as the “short-circuit voltage” V_{SC} . Figure 6.11b shows V_{SC} and V_{OC} as a function of light intensity. The difference is constant, ~ 230 mV. Similar results have been obtained for dye sensitized nanostructured TiO_2 [12]. Using transient photovoltage as a tool to study recombination, O’Regan and Lenzmann concluded that the quasi Fermi level inside dye-sensitized nanostructured TiO_2 was lowered by 240 mV when changing from open-circuit to short-circuit conditions under 80 mW cm^{-2} white-light illumination[17]. The electron lifetime in ZnO cells under short-circuit conditions can be estimated using V_{SC} and the lifetime-potential relation shown in Figure 6.11b. Electron lifetimes under shortcircuit conditions appear to be very long, more than 10 s. This means that no significant recombination takes place during charge transport in the nanostructured ZnO. The low IPCE values for dye-sensitized ZnO solar cells must therefore be attributed to poor electron injection efficiency.

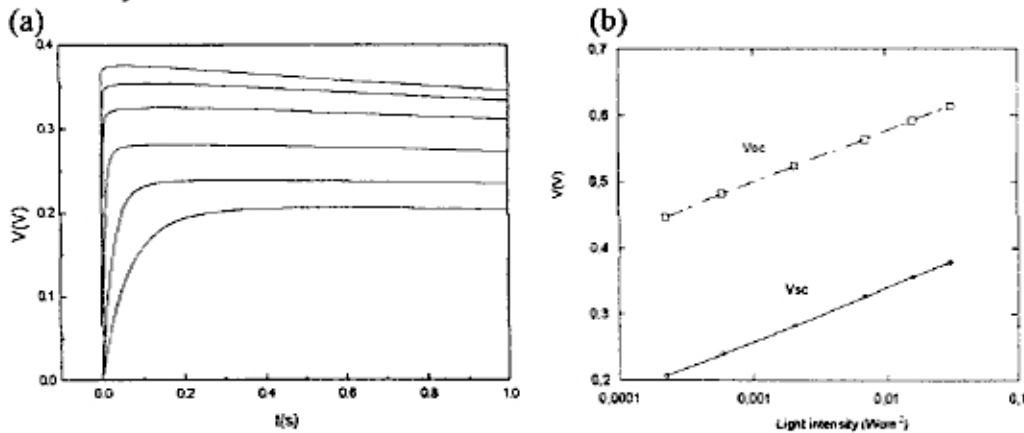


Figure 6.11 (a) Voltage transients of a dye-sensitized ZnO solar recorded in the dark at open circuit after illumination ($0.2 - 24 \text{ mWcm}^{-2}$) under short circuit conditions.

(b) Open circuit potential (V_{oc}) and internal potential under short circuit conditions (V_{sc}) in a dye-sensitized ZnO solar cell as function of light intensity. Electrolyte 2.

Bibliography

- [1] Keis, K.; Lindgren, J.; Lindquist, S.-E.; Hagfeldt, A. *Langmuir*, 16(2000), 4688.
- [2] Willis, R. L.; Olson, C.; O'Regan, B.; Lutz, T.; Nelson, J.; Durrant, J. R. *J. Phys. Chem. B*, 106 (2002), 7650.
- [3] Wenger, B.; Grätzel, M.; Moser, J.-E. *J. Am. Chem. Soc.*, 127(2005), 12150.
- [4] Cao, F.; Oskam, G.; Searson, P. C. *J. Phys. Chem.*, 100(1996), 17021.
- [5] Dloczik, L.; Illeperuma, O.; Lauermann, I.; Peter, L. M.; Ponomarev, E. A.; Redmond, G.; Shaw, N. J.; Uhlendorf, I. *J. Phys. Chem. B*, 101(1997), 10281.
- [6] Fisher, A. C.; Peter, L. M.; Ponomarev, E. A.; Walker, A. B.; Wijayantha, K. G. U. *J. Phys. Chem. B*, 104 (2000), 949.
- [7] Schlichthörl, G.; Huang, S. Y.; Sprague, J.; Frank, A. J. *J. Phys. Chem. B*, 101(1997), 8139.
- [8] G. Schlichthörl; N. G. Park; A.J. Frank. *J. Phys. Chem. B*, 103(1999), 782.
- [9] Seager, C. H.; Myers, S. M. *J. Appl. Phys.*, 94(2003), 2888.
- [10] L. Forro; O. Chauvet; D. Emin; L. Zuppiroli; H. Berger; F. Lévy. *J. Appl. Phys.*, 75(1994), 633.
- [11] E. Galoppini; J. Rochford; H. Chen; G. Saraf; Y. Lu; A. Hagfeldt; G. Boschloo, *J. Phys. Chem. B*, 110(2006), 16159.
- [12] G. Boschloo; A. Hagfeldt, *J. Phys. Chem. B*, 109(2005), 12093.
- [13] A. Zaban; M. Greenshtein; J. Bisquert, *ChemPhysChem*, 4(2003), 859.
- [14] There is some difference in the lifetimes of Figures 6b and 5a; this can probably be attributed to the fact that the data in the two figures stem from two different series of cells and measurements, separated in time by about a year.
- [15] P. J. Cameron; L. M. Peter, *J. Phys. Chem. B*, 109 (2005), 7392
- [16] N. W. Duffy; L. M. Peter; R. M. G. Rajapakse; K. G. U. Wijayantha, *Electrochem. Commun.*, 2 (2000), 658.
- [17] O'Regan, B.; Lenzmann, F. *J. Phys. Chem. B*, 108(2004), 4342.

Chapter 7 New dye D5: Charge transfer process in dye sensitized ZnO solar cells

In this chapter we make a description of one successful organic dye, called D5 [1], and compare its performance with the standard dye in DSC research, the N719. The polyene-diphenylaniline dye D5 is relatively easily synthesized and shows good solar cell performance. Power conversion efficiencies exceeding 5% have been obtained using an iodide/triiodide-based redox electrolyte [1].

Time sensitization plays an important role on ZnO DSC. In the precedent chapters, high concentration in the dye loading and short time of sensitization was used. Here with the new dye D5 was possible use low concentration of the dye and longer times of sensitization.

In consequence, there is great interest in fully organic dyes as sensitizers, as they can have very high extinction coefficients, and can potentially be produced at a lower cost.

7.1. *Dye sensitizers : D5 – N719*

The polyene-diphenylaniline dye D5, was compared with the standard sensitizer N719 ($\text{Ru}(\text{dcbpy})_2(\text{NCS})_2$) in a comparative dye-sensitized solar cell investigation. In solar cells with relatively thin layers of mesoporous TiO_2 ($< 3 \mu\text{m}$) D5 outperformed N719 because of its high extinction coefficient. Until now, best efficiency and stability data for dye-sensitized solar cells (DSCs) have been obtained with Ru-based sensitizers [2,3].

In this study we use ZnO nanoparticle films, synthesized with the same procedure as mentioned in chapter 5. A study of the performance of organic dye sensitized ZnO solar cells and the influence of the electrolyte nature is presented in last part.

7.1.1. **Photoelectrochemical measurements**

Study was made with the two dyes N719 and D5. The ZnO films used were $4 \mu\text{m}$ thick. These films were sintered at 380°C for 30 minutes. Dye sensitization of the photoelectrodes was made in 5 mM ethanolic solution overnight. The electrolyte used was 0.1 M I_2 , 0.1 M LiI , 0.6 M $[(\text{C}_4\text{H}_9)_4\text{N}]\text{I}$ in 3-methoxypropionitrile (3MPN) and 0.5M of 4-terbutylpyridine. A platinized conducting glass was used as a counter electrode.

Table 7.1 Photovoltaic parameters of D5 and N719 sensitized ZnO solar cells

Dye	1 sun				1/10 sun			
	n %	FF	Isc (mAcm ⁻²)	Voc(V)	n %	FF	Isc(mAcm ⁻²)	Voc(V)
D5	1.86	0.37	7.01	0.72	3.00	0.57	0.850	0.62
N719	0.15	0.40	0.45	0.70	0.45	0.38	0.200	0.62

In table 7.1 the efficiency results are presented, fill factor, open-circuit voltage and short-circuit current for ZnO DSC based on N719 and D5, respectively. Higher efficiency is evident for D5 based DSC mainly due to significantly higher photocurrent. This photocurrent is the highest obtained on this work and shows the crucial importance of the dye. Fill factor is low for both kinds of cells; it could be improve in subsequent studies. The open-circuit voltages present a constant value for both type of cells.

The D5 sensitized ZnO solar cell has a maximum IPCE about 64% at around 460 nm (figure 7.1). N719 sensitized ZnO solar cell has a poor performance, because a large fraction of the dye is ineffective due to multilayer or aggregate formation [2]. The effective sensitization of ZnO by D5 suggests that no multilayers or aggregated D5 is deposited on the surface. This could be related to the difference in the number of carboxylic acid binding groups of D5 and N719, and also the difference pKa of these group might have an effect.

It is important to notice that the IV results were reproducible after 1, 2 days and several weeks for D5 sensitized ZnO solar cells.

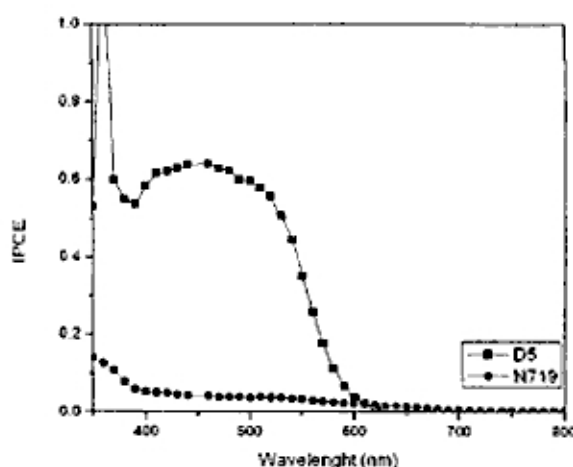


Figure 7.1 IPCE spectras of N719 and D5 sensitized ZnO solar cell

7.1.2. Electron transport studies

Electron transport and electron lifetimes were measured with time-resolved techniques (see Experimental Section). Electron transport was faster at lower light intensity in N719 sensitized ZnO solar cell than in D5 sensitized ZnO solar cell.

Even if the transport is similar for both kinds of cells, the overall efficiency collection at the back-contact also depends on the electron recombination. Electron lifetimes in N719 sensitized ZnO solar cell are longer than those of D5 sensitized ZnO solar cell, although both show a power-law dependence on light intensity (see Figure 7.2). These results can be explained by taking into account the trapping/detrapping model. When the light intensity is increased, deep traps are filled. As the detrapping process from shallow traps

is faster, the electron diffusion coefficient becomes larger while recombination is favored, diminishing electron lifetime. It seems that electron lifetime is limited by conduction band electrons, and most of the traps are not recombination centers[4].

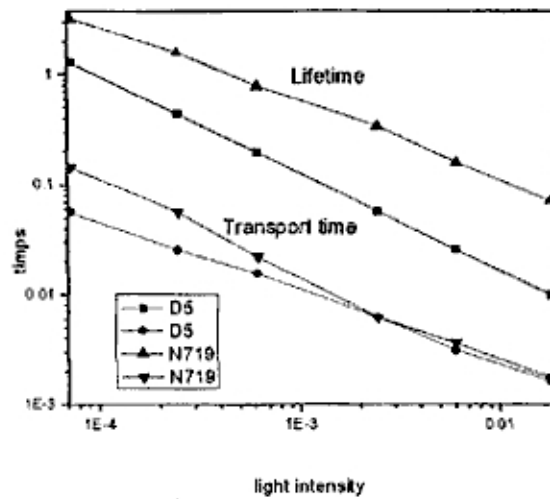


Figure 7.2 IMPS and IMVS time constants as a function of light intensity ($\lambda=640$ nm) for N719 and D5 sensitized ZnO solar cells with electrolyte 1. Drawn lines are power-law fits.

According to Yanagida [5] implies that the slow electron transport in DSC is intrinsically compensated by long electron lifetime because its origin is the same.

Figure 7.3 shows the decay of the open-circuit potential that follows after switching off the light for D5 and N719 sensitized ZnO DSCs. The decay is significantly slower in the N719 sensitized ZnO cell, in agreement with the larger IMVS time constants (fig.7.2). The electron lifetime can be calculated from the voltage transients using eq 2[6] (chapter 6)

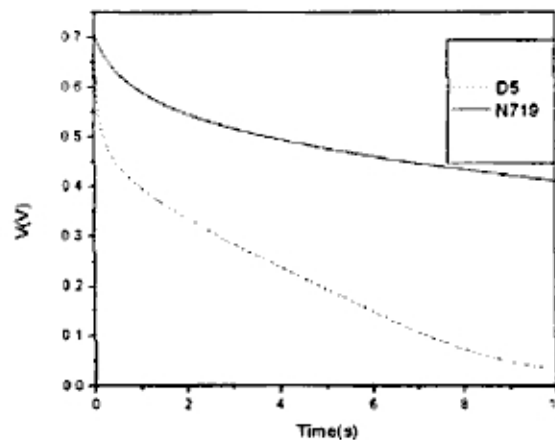


Figure 7.3 Open-circuit voltage decay transients of dye-sensitized nanostructured ZnO and TiO₂ solar cells with electrolyte 1.

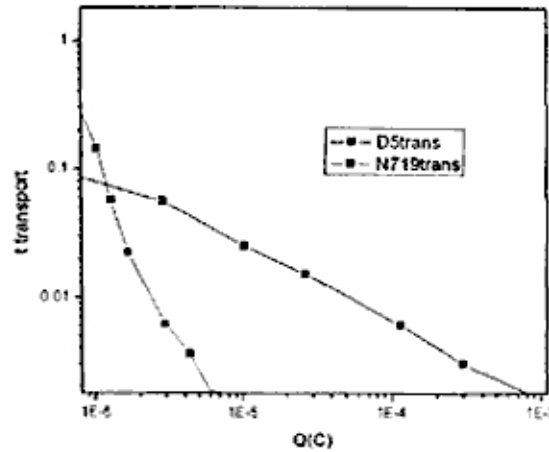


Figure 7.4 Electron transport as function of extracted charge at different light intensities. Time constants were determined using time-resolved small modulation techniques. DSC based on D5 and N719 sensitized ZnO

Figure 7.4 shows t_{IMPS} as function of the charge extracted from the D5 and N719 sensitized ZnO DSC in the photocurrent decay experiment. The curves obtained for the N719 cells are clearly shifted toward smaller charge. This implies that for a certain electron transport speed or t_{IMPS} ; much less charge is accumulated in the D5 sensitized nanostructured ZnO.

The trap distributions can be obtained by measuring the amount of accumulated charge as a function of the open-circuit voltage, if we assuming the existence of an exponential distribution below the conduction band [7,8]. From the derivative of this relation it is possible to obtain the distribution of trap states.

$$N_{trap}(qV_{oc}) = \frac{1}{q} \frac{dQ_{trap}}{dV_{oc}}$$

where Q_{trap} is the extracted charge under open-circuit conditions and $N_{trap}(qV_{oc})$ is the trap distribution as a function of the photovoltage. Figure 7.5 compares the experimentally determined charge as a function of the open-circuit potential together with the best fit for an exponential trap distribution. The measure of how rapidly the trap density varies with energy; (dQ_{trap}/dV_{oc}) is 0.19 for N719 and 0.27 for D5 DSC.

Furthermore, in Figure 7.5 a significant shift can be observed: the amount of extracted charge at a given open-circuit potential is lower in the case of D5 sensitized ZnO DSC.

The photovoltage could be defined as:

$$V_{oc} = \frac{E_{CB}}{q} + \frac{kT}{q} \ln\left(\frac{n+n_0}{N_{CB}}\right) - \frac{E_{redox}}{q}$$

n_0 being the conduction band electron concentration in the dark, n the photoinjected electrons, E_{CB} corresponds to the conduction band energy, N_{CB} is the effective density of conduction band states, and E_{redox} the electrolyte redox potential. Hence, the open circuit potential depends on the photoinjected electron concentration, on the conduction band position, and on N_{CB} . As seen in Figure 7.5, at the same total electron concentration of $7.8 \times 10^{-5} \text{ C cm}^{-2}$ in the film, a shift of 110 mV can be measured.

This shift can be partially ascribed to a higher energetic conduction band position for D5 DSC. This that could be attributed to the less number of protons present in D5 (one

carboxylic acid) compared to N719 (two carboxylic acids) originated from the number of anchoring group

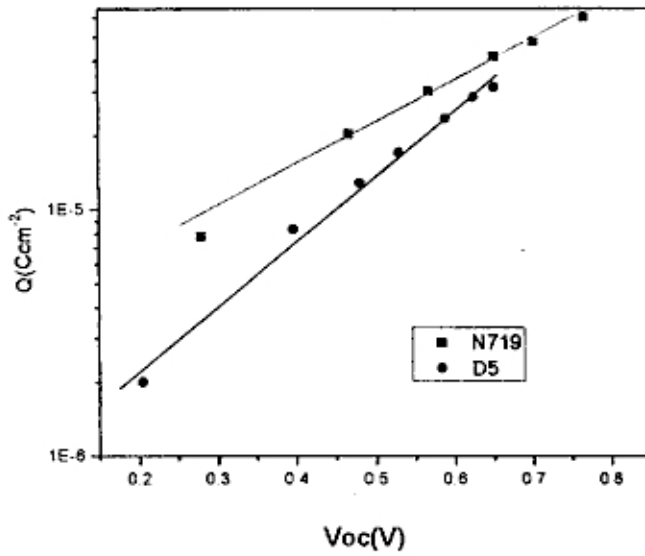


Figure 7.5 Extracted charge as function of open-circuit potential for a dye-sensitized nanostructured ZnO cell with electrolyte 2. The drawn line is an exponential fit.

7.1.3. ATR measurements

The ATR spectra of the ZnO bare film is shown in Figure 7.7. The principal bands are almost coincident with those of acetate groups observed in the spectrum of the zinc acetate used for the preparation of the ZnO sol. These bands are considered to be due to a variety of forms of acetate complexes on surfaces of ZnO particles and correspond to C-O stretching (1585 cm^{-1}) and C=O stretching ($\sim 1400\text{ cm}^{-1}$) [9]. The small absorbance band at 1344 cm^{-1} is due to the weakly bound acetic acid molecules, which, due to their protonated state [10].

Figure 7.8 shows ATR spectra of D5 powder and D5 sensitized ZnO. In the graph the vibration mode for each peak is pointed out. The difference between the two spectras is due to D5 adsorption on ZnO film.

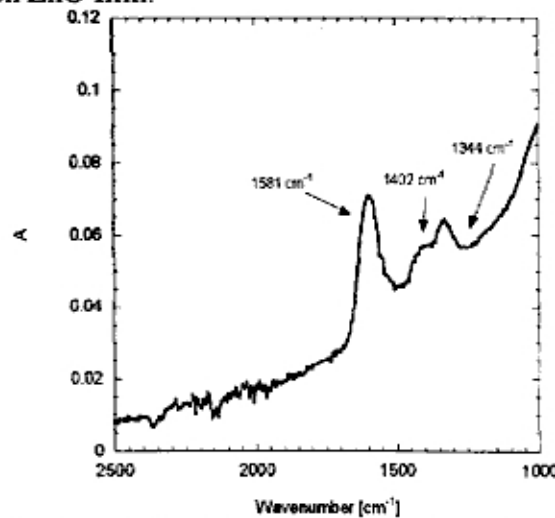


Figure 7.7 ATR spectra of ZnO bare film. The film was sintered at 380°C .

Absorptions at 1586, 1508, 1491 and at 1393 cm^{-1} correspond to a carbonyl stretching vibration from carboxylate groups and an asymmetric and symmetric C-O stretching vibration from carboxylate groups, respectively.

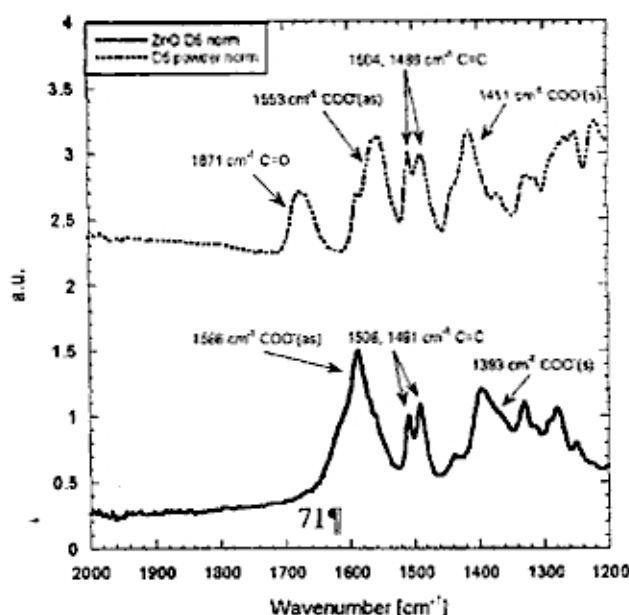


Figure 7.8 ATR spectra of D5 powder and sensitized ZnO film

7.2. Different concentration of Li^+ in the electrolyte

Optimization of ZnO DSC was one objective of this work. Using different ways the sensitization and different dyes it was improved it. Nevertheless, components in the electrolyte were not analyzed. In this part we study the strength influence of the Li^+ in the electrolyte.

7.2.1. Photoelectrochemical measurements

Solar cells were constructed as described before (section 7.1). The influence of the concentration of Li^+ on the efficiency was studied in the presence of a fixed concentration of I^- . Li^+ concentration was adjusted using LiClO_4 .

The efficiency, fill factor, the open circuit voltage, and the photocurrent for the solar cells are displayed in the table 7.2. The maximum efficiency, reached in the electrolyte 2 (low Li^+ concentration) is as high as 2.36%. Maximum photocurrent 7.12 mAcm^{-2} is obtained from the same cell at 1000 mW/cm^2

Table 7.2. Current and voltage characteristics of D5 sensitized ZnO solar cells, with different concentrations of Li^+ in the electrolyte

Electr.	1 sun				1/10 sun			
	n (%)	Voc(V)	FF	Isc(mAcm^{-2})	n(%)	Voc(V)	FF	Isc(mAcm^{-2})
1	1.82	0.75	0.54	4.52	2.16	0.64	0.63	0.54
2	2.36	0.68	0.49	7.12	2.43	0.56	0.54	0.81
3	1.86	0.65	0.43	6.70	2.43	0.56	0.54	0.81

Electrolytes:

1 0.1M LiClO₄, 0.6M TBAI, 0.5M 4-TBP, 0.1M I₂ in 3-MPN (high Li⁺)

2 0.001M LiClO₄, 0.7M TBAI, 0.5M 4-TBP, 0.1M I₂ in 3-MPN (low Li⁺)

3 0.7M TBAI, 0.5M 4-TBP, 0.1M I₂ in 3-MPN(no Li⁺)

In figure 7.9 the IPCE action spectra of D5 sensitized ZnO DSC is shown. The effect of Li⁺ concentration on efficiency has a similar trend than IV measurements. The maximum photoresponse was obtained at low concentration of Li⁺ (electrolyte 2) about 70% at 420 nm. The thickness of ZnO films used was about 3 μm.

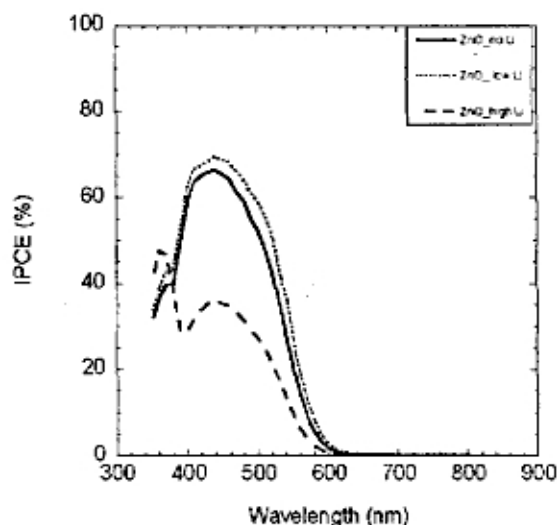


Figure 7.9 IPCE spectra for DSC based on D5 sensitized ZnO with different concentration of Li⁺ in the electrolyte.

7.2.2. Electron transport studies

Time resolved techniques were used in measure electron transport times and lifetimes. Similar results were obtained for these set of samples (it is not shown).

Figure 7.10 shows the relation between open circuit potential and charge in the nanostructured ZnO solar cells that was investigated using a charge extraction technique [7]. It was stated, earlier; the position of the quasi-Fermi level of electrons inside the semiconductor film is determined by the number of electrons accumulated under illumination and by the position of the CB position. From Figure 7.10 it can be observed that for the same value of accumulated charge the open circuit potential is different for the different electrolytes, indicating different CB positions. The position of the CB potential depends on the surface charge and therefore the nature of cation. For small adsorbing Li⁺ (positive) ions the CB shift into more positive potentials. For the present system based on D5 sensitized ZnO solar cells the opposite trend is observed. As can be seen in figure 7.10 the electrolyte with highest Li⁺ concentrations showed the most negative position of the CB, where the solar cells with 0.01 M or 0 M of Li⁺ shows about 100mV more positive position of the CB at the same charge.

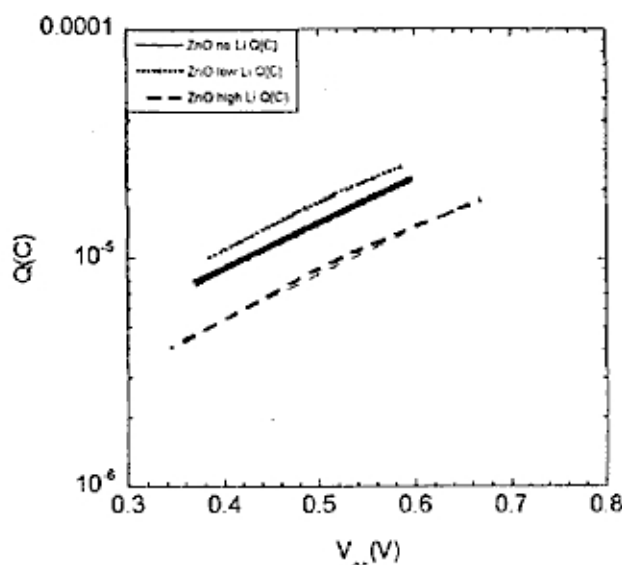


Figure 7.10 Extracted charge under short circuit conditions as a function of open circuit potential in DSC based on D5 sensitized ZnO with different electrolytes

In figure 7.11, electron lifetime as function of extracted charge different light intensities, show longer lifetimes for ZnO DSC with low concentration of Li⁺.

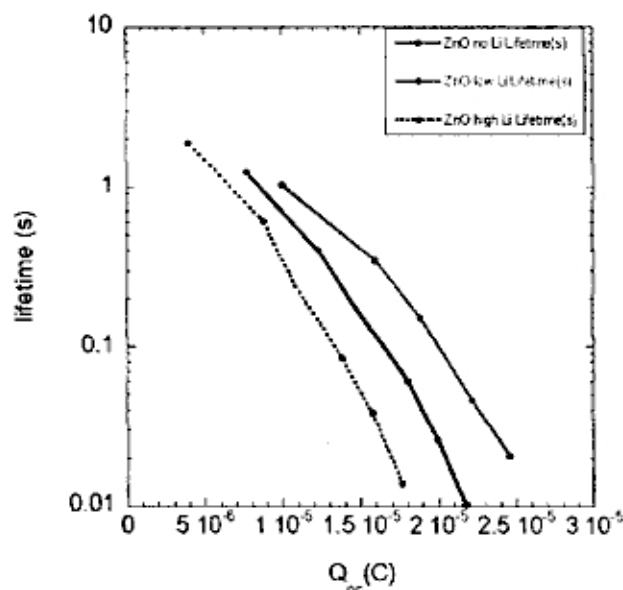


Figure 7.11 Electron lifetime as function of extracted charge at different light intensities. Time constants were determined using time-resolved small modulation techniques. DSC based on D5 sensitized ZnO with different concentration of Li⁺ in the electrolyte.

IV dark measurements, see Figure 7.12, shows at what voltage the system start to produce recombination currents. The results clearly show the equivalent trend as observed for the sensitized case leading to the conclusion that the reaction is occurring between the ZnO anode and the electrolyte.

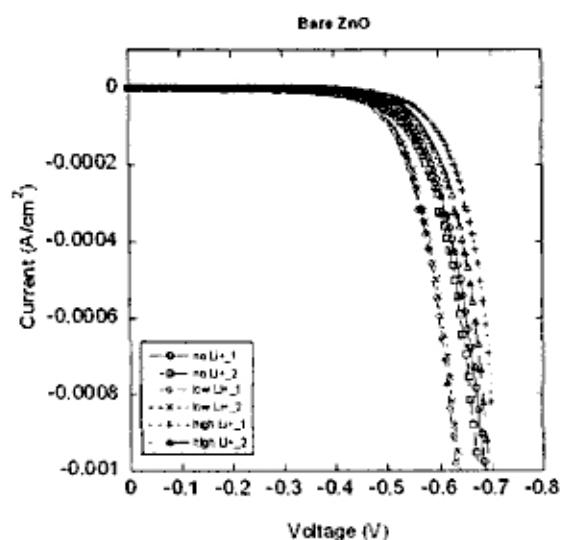


Figure 7.12 IV dark on bare ZnO electrodes with (black) electrolyte 1, (red) electrolyte 2 and (blue) electrolyte 3, in 3-MPN.

Bibliography

- [1] D. P. Hagberg, T. Edvinsson, T. Marinado, G. Boschloo, A. Hagfeldt, L. Sun, *Chem. Commun.* (2006) 2245.
- [2] M. Grätzel, *J. Photochem. Photobiol. C: Photochem.Rev.* 4 (2003) 145.
- [2] Y. Chiba, A. Islam, Y. Watanabe, R. Komiya, N. Koide, L. Han, *Jpn. J. Appl. Phys.* 45 (2006) 638.
- [4] J. Bisquert; V. S. Vikhrenko, *J. Phys. Chem. B*, 108(2004), 2313.
- [5] S. Yanagida, *C. R. Chim.*, 9 (2006), 597.
- [6] Zaban, A.; Greenshtein, M.; Bisquert, J. *ChemPhysChem*, 4(2003),859.
- [7] N. W. Duffy; L. M. Peter; R. M. Rajapakse; K. Wijayantha, *G.U. Electrochem. Commun.*, 2(2000), 658
- [8] L. M. Peter; N. W. Duffy; R.L. Wang; K. G. U. Wijayantha, *J.Electroanal. Chem.*, 127 (2002), 524-525,
- [9] G. Socrates, *Infrared Characteristic Group Frequencies, Tables and Charts* (John Wiley & Sons, Chichester, 1994).
- [10] Shuji Sakohara, D.Lane, Tickenan, Marc A. Anderson, *J. Phys. Chem.*,96(1992), 11086-11091
- [11] G.B. Deacon; R.J. Phillip, *Coord. Chem. Rev.*, 33(1980), 227.
- [12] K. Nakamoto, *Infrared and Raman Spectroscopy of Inorganic and Coordination Compounds*; John Wiley and Sons: New York, (1986)

Chapter 8 Discussion

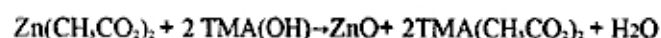
In this chapter the principal results obtained in this thesis are discussed. The results are divided into three parts:

- Effect of morphology and doping
- Comparison of ZnO DSC with TiO₂ DSC
- D5 sensitization in ZnO DSC

8.1. Effect of morphology and doping

8.1.1. ZnO nanorods and nanoparticles

ZnO nanoparticles were prepared from zinc acetate dihydrate in alcoholic solution under basic conditions [1]. The procedure is a modification of the method developed by Henglein et al.[2]. The overall reaction for the synthesis of ZnO nanoparticles from Zn(II) acetate can be written as:



We found that the shape of the ZnO particles was very sensitive to the overall concentration of precursors. At a zinc acetate dihydrate concentration of below 0.1M, quasi-spherical particles were formed, whereas mainly nanorods were formed at two times higher concentrations. Verges et al. reported similar observations for the formation of rodlike microcrystals [3].

In fact, it can be calculated from the thermodynamic data of the substances involved, that the dehydration reaction is practically thermoneutral at room temperature. That ZnO is formed in alcoholic solution must be due to a substantially lower free enthalpy of the products of hydration. Kinetically, the process is very complex. It was observed that ZnO is formed in alcoholic solutions only in the presence of small amounts of water. Rod formation occurred exclusively during the final heating step that is from already formed quasi-spherical particles.

According to XRD, zincite ZnO (wurtzite structure) is the only crystallographic phase detectable for ZnO nanoparticles and nanorods. The XRD pattern of the ZnO nanorods illustrates the texture effect of the anisotropic morphology on the relative intensity of the diffraction peak. As expected, a substantially higher intensity is obtained for the (002) diffraction peak on ZnO nanorods.

SE illumination resulted in higher IPCE values compared to EE illumination, this behavior is typically observed for nanostructured metal oxide photoelectrodes [4-6]

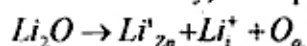
The electron losses during the transport to the back-contact in nanostructured material are related to reactions between electrons in the conduction band and electron-accepting

species in the electrolyte (O_2 , I_3^- , etc.) or by electron-hole recombination in the illuminated area of the film.

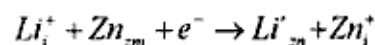
Electron transport in crystalline wires was expected to be several orders of magnitude faster than percolation through a random polycrystalline network. However, similar results were obtained for ZnO nanorods and nanoparticles, it could be ZnO nanorods films have not a ordered alignment being a similar structure with ZnO nanoparticles. In general, all results were similar between ZnO nanorods and nanoparticles.

8.1.2. Doped ZnO

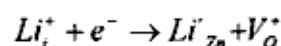
Li⁺ Case. Any of the films exhibits a strong (002) peak, indicating the c-axis orientation of ZnO grains. It is also seen that the intensity of the (002) peak increases with Li-doping up to $x=0.05$. It is believed that the interstitial zinc plays an important role in the grain growth of ZnO [7,8]. In the case of trivalent Al-doping, the concentration of the zinc interstitials is reduced, resulting in the suppressed grain growth of ZnO. This is because the diffusivity is decreased in ZnO. A similar effect can be observed in F-doped ZnO[9] On the contrary, Li-doping mainly occurs as follows [7]



where Li'_{zn} represents lithium on zinc lattice site, Li'_i lithium in interstitial position, and O_o oxygen on lattice site. Since Li^+ has a smaller ionic radius of 0.060 nm than Zn^{2+} having 0.074 nm, the diffusivity in the Li doped ZnO is expected to be higher. Nevertheless, Li-doping obviously reduces the current density of the films as shown in tables 5.1 and 5.3. Doping of 2.5 mol % Li is optimal. The reduced current density could be attributed to the replacement reaction of the Li interstitials as follows,[7,10]



or



A similar result was reported previously for the spray pyrolysed ZnO films.[11] With the fact that the grain size is smaller in these two films as read from Table 1, we can assume that too much lithium is not soluble in ZnO lattice and segregates probably in the grain boundary.

Table 1 The crystallite size and the current density of the Li- and Mg-doped ZnO thin films.

Dopant	Composition	Crystallite size (nm)	Current density ($mAcm^{-2}$)
	ZnO	15.3	5.00
Li ⁺	1.25 %	21.3	3.73
Li ⁺	2.5 %	21.3	4.49
Li ⁺	5 %	32.6	4.07
Mg ²⁺	1%	27.2	1.93
Mg ²⁺	0.3%	21.8	2.34

The relation between open circuit potential and charge in the nanostructured ZnO solar cell is showed in Figure 5.13. These results show how different the trap distributions are for Li⁺/ZnO films. The fitting is satisfactory for the cells at small photovoltage values. At a given charge, higher open circuit potentials are found for the film with high concentration of Li^+ . Assuming that the trap distribution in the nanostructured ZnO, defined with respect to the conduction band edge E_{CB} , is not affected by the changes in

the electrolyte, it is apparent the E_{CB} shifts to higher electron energy upon higher concentration of Li^+ ions. This is opposite to what is observed in TiO_2 -based solar cells [12]. The Li^+ ion effect was, however not straightforward. In presence of a low Li^+ concentration E_{CB} appeared to shift to lower electron energy compared to the situation without Li^+ ions.

Mg²⁺ Case. ZnO exhibited c-axis orientation with Mg-doping up to $y=0.05$ as confirmed by XRD. (100) and (101) peaks also appeared in the film with $y=0.10$. No peaks due to rock-salt MgO were observed in any film. The film of $y=0.10$ was often exfoliated off the substrate after the heat treatment. The Scherrer crystallite size increased by Mg-doping as shown in Table 1. Although the role of isovalent Mg^{2+} is not clear, a smaller ionic radius of 0.065 nm may be effective for diffusivity.

The current density decreases with increasing Mg^{2+} concentration. Substitution of Mg^{2+} for Zn^{2+} has no significant contribution to the cation charge in ZnO. In spite of this, the current density was reduced. The n-type conduction of ZnO is attributed to the interstitial zinc and/or oxygen vacancy.

Therefore, the above result should be explained by the decrease of the oxygen defects by Mg-doping since Mg-O bond has more ionic character than Zn-O [13].

8.2. Comparison with TiO_2 solar cell

We discuss in this part about exponential trapping model in TiO_2 and ZnO DSC.

The electron transport properties in nanostructured TiO_2 are frequently explained using trapping/detrapping models. A large part of the electrons is assumed to be trapped in localized states below the conduction band edge. Trapped electrons can be thermally excited to the conduction band and move freely before they are trapped again. The multiple trapping/detrapping process increases the transport time for the electrons strongly, and it can explain the light-intensity dependence of the transport by the energy distribution of the traps. Specifically, an exponential increase of the trap state density $N_{T(E)}$ toward the conduction band edge (eq 3) fits the experimental data well, as it results in power-law dependencies of transport time and charge with light intensity[14,15]

$$N_T(E) = N_{T0} \exp\left(\frac{E - E_{F0}}{m}\right) \quad (3)$$

In eq 3 N_{T0} is the trap state density at E_{F0} , which is the Fermi level of the TiO_2 in the dark, and m is the slope of the trap distribution. Considering the similarities in the results obtained with TiO_2 and ZnO, we now apply this model to nanostructured ZnO. From the potential-charge relation (Figure 6.10) it follows that $m=0.19$ eV and $N_{T0} = 1.7 \times 10^{17} \text{ cm}^{-3}$. Assuming the conduction band edge to be located about 0.9 eV above the redox energy of the electrolyte, a total density of traps in the ZnO of about $2 \times 10^{19} \text{ cm}^{-3}$, or 40 traps per ZnO particle, is calculated. This appears to be a reasonable result as it is well known that as-prepared ZnO can contain a significant amount of defects. Following the approach outlined by van de Lagemaat and Frank[15], the slope m can also be calculated from the light-intensity dependence of the short-circuit charge and the IMPS time constant, yielding in our case for ZnO only a reasonable value in the case of Q_{sc} , $m=0.049$ eV.

The quasi Fermi level (E_F) in the mesoporous ZnO film under illumination at short-circuit conditions was determined using the V_{sc} (voltage extraction) measurement[16] Recently, Lobato et al. measured E_F in a nanostructured TiO_2 solar cell directly by

addition of an extra electrode on top the porous TiO₂ film[17] Their results are in excellent agreement with our voltage extraction method. In our experiment with ZnO a clear increase of V_{sc} with light intensity is found, from 0.2 to 0.4 V with increasing light intensity. Considering the trap model described above and the estimated value of E_{CB} of 0.9 eV (vs E_{redox}), one might expect to find activation energies for electron transport of about 0.6 eV. The apparent activation energies that are calculated from the temperature-dependent IMPS measurements under short-circuit conditions are, however, much smaller, about 0.1 eV. This apparent discrepancy was explained recently by Peter et al. using the quasi-static multiple trapping model [18] The anomalously low apparent activation energies are a consequence of the boundary conditions imposed by the short-circuit condition and the quasi-static relationship between changes in the densities of free and trapped electrons. As the short-circuit current is almost independent of temperature, E_F is forced to move downward with increasing temperature, so that the decrease in transport time is much less than one might expect.

The presence of an exponential distribution of trap states in nanostructured ZnO may be questioned. Evidence from spectroelectrochemistry[19,20] and laser spectroscopy[21] suggests that electrons in nanostructured ZnO electrodes are located in the conduction band and/or shallow traps. Specifically, upon electron accumulation a bleach of the excitonic absorption band of ZnO as well as free-electron absorption is observed. The presence of localized electronic states in the band gap of ZnO is, however, well documented [22] Intrinsic defects, such as oxygen vacancies and interstitial Zn atoms, will affect the electronic properties of ZnO. As-prepared ZnO tends to show significant n-type conductivity, which is mainly caused by interstitial Zn atoms that act as shallow donors, with an energy level about 0.03 eV below the conduction band edge [23] Also hydrogen can act as a shallow donor in ZnO[24,25]. While being very important for the conductivity of ZnO, such shallow donors (traps) do not directly explain the observed slow and light-intensity-dependent electron transport in nanostructured ZnO.

If the donor density in nanostructured ZnO films is sufficiently high, band bending within the individual nanocrystal can occur and may determine the electronic properties of the film. If we assume that the donor density is equal to the estimated total density of traps from the charge extraction measurements ($\sim 2 \times 10^{19} \text{ cm}^{-3}$), which implies that all traps are positively charged impurities, an estimation of the maximum potential drop within a single ZnO nanocrystal (ϕ_{sc}) can be calculated using eq 4:

$$\phi_{sc} = \frac{eN_D}{6\epsilon\epsilon_0} r^2$$

where ϵ is the relative dielectric constant of ZnO ($\epsilon = 8^9$), ϵ_0 is the permittivity of vacuum, and r is the radius of the particle. For the fully depleted particle ϕ_{sc} is calculated to be ~ 0.5 V. A significant band bending may therefore be present in the ZnO particles. This is a possible cause of the very slow recombination of electrons in ZnO with triiodide in the electrolyte. In comparable TiO₂ particles band bending would be much less because of the higher dielectric constant in anatase ($\epsilon = 50$). As a result of band bending between adjacent ZnO particles, energy barriers would be formed at grain boundaries. The thermally activated crossing of these barriers by the electrons would result in slow transport in the nanostructured ZnO films. Upon electron accumulation, band bending and consequently barrier height would decrease and electron transport would become faster. Such a barrier model can, at least qualitatively, explain light-intensity-dependent electron transport in doped nanostructured films.

In a barrier model, electron transport is determined by the rate of electron hopping from ZnO particle to particle. From the transport time (0.57 ms at the highest light intensity in Figure 6.5a) an effective electron diffusion coefficient in the nanostructured ZnO of $1.2 \times 10^{-4} \text{ cm}^2 \text{ s}^{-1}$ is calculated using $D_{\text{eff}} = w^2/(2.35\tau_{\text{IMPS}})$ [26], where w is the film thickness. The time τ_j for a single electron jump across the barrier from one ZnO nanocrystal to the next can be calculated using the Einstein-Smoluchowski equation $D_{\text{eff}} = d^2/2\tau_j$, where d is jump distance, which is equal to the nanocrystal diameter. It can thus be calculated that $\tau_j = 11 \text{ ns}$, and the electron makes on average 5.3×10^4 jumps before reaching the conducting substrate. The thermionic emission model can be used to describe electron transfer in semiconductors across a barrier [27]

$$j = AT^2 \exp\left(-\frac{\Delta E}{kT}\right)$$

In this expression j is the current density, ΔE is the barrier height, and A is the Richardson constant for thermionic emission ($A = 120(m^*/m_e) A \text{ cm}^{-2}$). Using the effective electron mass in ZnO (m^*) of $0.3m_e$, and assuming that the contact area between the nanocrystals is 50 nm^2 (the area of circle with radius 4 nm), it can be calculated that a jump time of 11 ns is obtained with a barrier height of 0.3 eV, which seems to be a very reasonable value considering that the band bending in a fully depleted ZnO nanoparticle was estimated to be 0.5 eV.

Nanostructured films composed of highly doped spherical semiconductor particles will show similarly shaped voltammograms, as was demonstrated by model calculations, as well as by experiments with highly doped nanostructured $\text{SnO}_2:\text{Sb}$ electrodes, by Boschloo and Fitzmaurice[28]. We can estimate that the doping density in the ZnO needs to be about $5 \times 10^{19} \text{ cm}^{-3}$ to allow for sufficient potential drop in the ZnO particles (0.8 V), so that voltammograms similar to that shown in Figure 2 can be obtained. This doping density seems, however, rather high for unintentionally doped ZnO material. At this point, however, we cannot exclude the possibility that the electron transport and recombination properties of nanostructured ZnO electrodes are caused by a significant doping density that leads to band bending and energy barriers at grain boundaries.

8.3. Effect of new dye D5

The performance D5-sensitized ZnO is very good: the IPCE reached up to 64%. It is important to note that the same simple procedure for dye adsorption was used: the films were immersed in ethanolic solution of the dye (0.5 mM) during 16 hrs. The effective sensitization of ZnO by D5 suggests that no multilayers or aggregated D5 is deposited on the surface. This could be related to the difference in pKa value of the carboxylic acid binding groups between D5 and N719.

The results are presented in Figure 7.10, and show an opposite trend of the CB shift upon varying the lithium concentration, showing a negative CB shift for the highest lithium concentration, for the electrolyte 1. This explains the odd trend in IPCE, where electrolyte 3, with lowest lithium concentration showed the highest IPCE due to the most positive position of the CB and hence the largest driving force for effective charge injection. The electron lifetimes were further studied from transient voltage responses upon a small light intensity modulation, where the voltage response was fitted to a first order decay yielding the time constants referred to as the lifetimes, see Figure 7.11.

The lifetime trend also supports that lowest lithium concentration in the electrolyte results in longest lifetimes at a fixed amount of charge in the ZnO electrode. The lifetime

is plotted versus the charge, leading to an unfair comparison when plotted directly against the open circuit voltage.

ZnO is "reacting" in the presence of electrolyte independent on the dye, meaning that the surface or the composition of ZnO changes over time. This process involves a change in CB position and hence also in the photovoltaic performance of the solar cell. To investigate how the system is affected over time, UV-vis absorption spectra were taken of the sensitized films before and after sealing the solar cells.

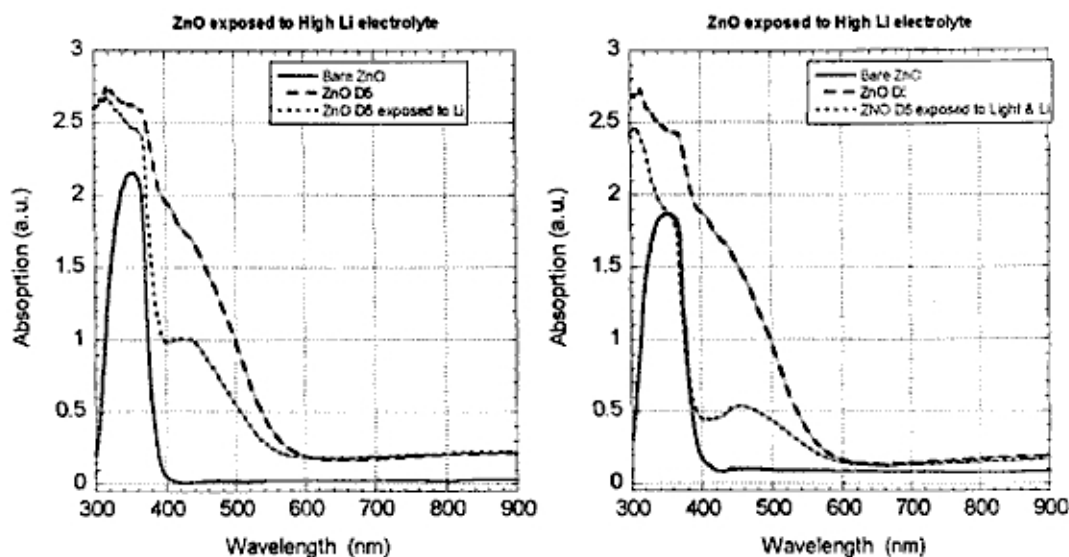


Figure 8.1 UV-vis of ZnO working electrodes; bare ZnO (—), D5 sensitized ZnO (---) and D5 sensitized ZnO exposed to redox electrolyte 1, no lithium (.....), (left) in the dark, (right) after illumination.

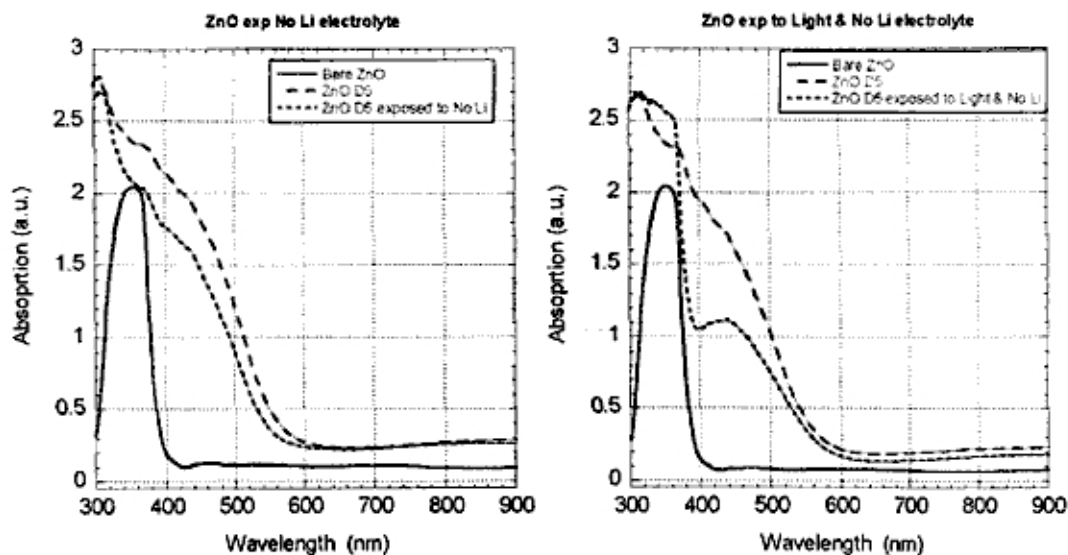


Figure 8.2 UV-vis of ZnO working electrodes; bare ZnO (—), D5 sensitized ZnO (---) and D5 sensitized ZnO exposed to redox electrolyte 3, 0.1M lithium(.....), (left) in the dark, (right) after illumination.

The stability of the D5-sensitized ZnO solar cells was not very good. A significant reduction of the D5 dye load was observed when solar cells were assembled: a sandwich was made of the D5-sensitized electrode with a counter electrode, filled with redox electrolyte and left overnight. Figure 8.2 shows that there was a significant reduction of the amount of adsorbed dye on the ZnO electrode after disassembling the cells. The degree of dye desorption was found to depend on the cations in the electrolyte and the exposure

to light. Without exposure to light, about 20% of the D5 desorbed in electrolyte 3 (only TBA⁺), while more than 40% desorbed in electrolyte 1 (with 0.1 M Li⁺). With light exposure, these values were about 40% and 70%, respectively.

The underlying reasons for the dye desorption are not fully clear. Possibly there is a slow dissolution process of the ZnO surface caused by the carboxylic acid group of the D5, but it is unclear how the Li⁺ ions play a role in this. As protons will be used in the dissolution process ($\text{ZnO} + 2 \text{H}^+ = \text{Zn}^{2+} + \text{H}_2\text{O}$), the surface pH of the ZnO will increase, leading to a more negative surface charge and a higher energy for E_{CB}. This is in accordance with the observed E_{CB} shift in the presence of 0.1 M Li⁺. The more negative surface charge may prevent re-absorption of the dye.

Dye desorption is strongly increased upon illumination. There are several possible explanations: Injected electrons in ZnO may reduce the binding strength of the D5 dye; Oxidized dye molecules will be stronger acids and cause thereby more dissolution of the ZnO surface; the UV-component in the light can cause direct excitation of the ZnO, creating holes that are known to cause dissolution of ZnO.

Although the dye-adsorption process appeared to be without problem, significant dye dissolution occurred after solar cell assembly. This may be attributed to slow dissolution of the ZnO surface, a process that appears to be accelerated by light. The overall stability of the solar cells was therefore poor. A way to improve stability of ZnO based DSC is to apply a thin surface coating to make the surface more chemically resistant.

Bibliography

- [1] H. Womelsdorf, W. Hoheisel, G. Passing, DE-A 199 077 04 A 1, (2000).
- [2] M. Haase, H. Weller, A. Henglein, *J. Phys. Chem.*, 92(1988), 482-487.
- [3] M. A. Verges, A. Mifsud, C. J. Serna, *J. Chem. Soc. Faraday Trans.*, 86(1990), 959-963
- [4] A. Hagfeldt, U. Björksten, and S.-E. Lindquist, *Sol. Energy Mater. Sol. Cells*, 27(1992),293.
- [5] G. Hodes, I. D. J. Howell, and L. M. Peter, *J. Electrochem. Soc.*, 139(1992), 3136.
- [6] A. Hagfeldt and M. Grätzel, *Chem. Rev.*, 95(1995), 49
- [7] P. Bonasewicz, W. Hirschwald, and G. Neumann, *J. Electrochem. Soc.*, 133(1986), 2270-2278.
- [8] Y. Ohya, H. Saiki, T. Tanaka, and Y. Takahashi, *J. Am. Ceram. Soc.*, 79(1996), 825-830
- [9] Fujihara, S., Kusakado, J. and Kimura, T., *J. Mater. Sci. Lett.*, 17(1998), 781-783.
- [10] J.K. Srivastava, L. Agarwal, and A.B.Bhattacharyya, *J. Electrochem.Soc.*, 136(1989), 3414-3417.
- [11] Pushparajah, P., Arof, A. K. and Radhakrishna, S., *J.Phys. D*, 27(1994), 1518-1521.
- [12] Redmond, G.; Fitzmaurice, D. *J. Phys. Chem.*, 97(1993), 1426.
- [13] Onodera, A., Tamaki, N., Jin, K. and Yamashita, H., *Jpn. J. Appl. Phys.*, 36(1997), 6008-6011.
- [14] Fisher, A. C.; Peter, L. M.; Ponomarev, E. A.; Walker, A. B.;Wijayantha, K. G. U. *J. Phys. Chem. B*, 104(2000), 949.
- [15] van de Lagemaat, J.; Frank, A. J. *J. Phys. Chem. B*, 104(2000),4292
- [16] Boschloo, G.; Hagfeldt, A. *J. Phys. Chem. B*, 109(2005), 12093.
- [17] Lobato, K.; Peter, L. M.; Wurfel, U. *J. Phys. Chem. B*, 110(2006), 16201.

- [18] Peter, L. M.; Walker, A. B.; Boschloo, G.; Hagfeldt, A. *J. Phys.Chem. B*, 110(2006), 13694.
- [19] Redmond, G.; O’Keeffe, A.; Burgess, C.; MacHale, C.; Fitzmaurice, D. *J. Phys. Chem.*, 97 (1993), 11081.
- [20] Bauer, C.; Boschloo, G.; Mukhtar, E.; Hagfeldt, A. *Chem. Phys.Lett.*, 387(2004), 176
- [21] Katoh, R.; Furube, A.; Hara, K.; Murata, S.; Sugihara, H.; Arakawa, H.; Tachiya, M. *J. Phys. Chem. B*, 106 (2002), 12957.
- [22] Ozgur, U.; Alivov, Y. I.; Liu, C.; Teke, A.; Reshchikov, M. A.; Dogan, S.; Avrutin, V.; Cho, S. J.; Morkoc, H. *J. Appl. Phys.*, 98(2005), 41301
- [23] Look, D. C.; Hemsley, J. W.; Sizelove, J. R. *Phys. Rev. Lett.*, 82(1999), 2552.
- [24] Van de Walle, C. G. *Phys. Rev. Lett.*, 85 (2000), 1012.
- [25] Jokela, S. J.; McCluskey, M. D. *Phys. Rev. B*, 72(2005), 113201.
- [26] van de Lagemaat, J.; Frank, A. J. *J. Phys. Chem. B*, 105 (2001), 11194.
- [27] Sze, S. M. *Physics of Semiconductor DeVices*; Wiley: New York, (2006).
- [28] Boschloo, G.; Fitzmaurice, D. *J. Phys. Chem. B*, 103(1999), 3093.

Chapter 9 Conclusions

We have described the preparation and characterization of ZnO nanoparticles and films. The observations can be rationalized in the following points:

- Zinc oxide, prepared to give optimal film properties, is a potential material for efficient photoelectrochemical devices.
- Pure and Mg and Li doped ZnO thin films show preferred *c* orientation. The lattice constants *a* and *c* are found to decrease with increasing dopant concentration.
- Electron transport in dye-sensitized solar cells prepared from approximately equally sized nanocrystalline ZnO and TiO₂ particles was very similar in terms of transport times and light intensity dependence, but the electron lifetime was significantly higher in ZnO than in TiO₂.
- The performance of ZnO-based solar cells was less than that for TiO₂-based cells, despite the reduced recombination rate. This was attributed to lower electron injection efficiency from excited dye molecules into the ZnO conduction band and/or lower dye regeneration efficiency. The apparent activation energy for electron transport in nanostructured ZnO under short-circuit conditions was ~0.1 eV, nearly independent of light intensity. The internal voltage in the nanostructured ZnO under short-circuit conditions was about 0.23 V lower than V_{OC} . Results may be explained using a multiple trapping model. An alternative view was presented: If there is significant doping of the ZnO, band bending in the nanocrystals will result in energy barriers for electron transport and recombination that can explain then observed properties.
- This study shows that the stability of the ZnO photoelectrode depends not only in the dye bath, more importantly in combination with the electrolyte composition.

Future Works

The dye-sensitized solar cell research is quite interdisciplinary involving different areas of expertise such as photoelectrochemistry, electrochemistry of the electrolytes and catalysts, electroanalytical chemistry, quantum chemistry, colloid science, semiconductor physics, laser spectroscopy, synthetic organic chemistry, computational modeling etc. A combination of researchers with a background in different areas is evidently needed for a successful basic research with the DSCs.

With the new dye is possible to follow the research in different concentrations of Li⁺ in the electrolyte, PIA measurements can give us more information about the process in the solar cells.

Trapping and detrapping model could be no applied for ZnO cells it would be interesting continuing the research reproducing results with commercial ZnO powder.

Oriented ZnO nanorods could be a good alternative for improve the efficiency. In this thesis we use a non oriented ZnO obtained similar results with ZnO nanoparticles.